THE OHIO STATE UNIVERSITY

College of Engineering
Department of Chemical and Biomolecular Engineering
and Department of Materials Science and Engineering

Project Final Technical Report (Draft)

Submitted to the U.S. Department of Energy
National Energy Technology Laboratory

NATIONAL
ENERGY
TECHNOLOGY
LABORATORY

FE0031635: Transformational Membranes for Pre-Combustion Carbon Capture

W.S. Winston Ho
PI: W.S. Winston Ho, Professor
E-mail: ho.192@osu.edu
Phone: 614-292-9970; Fax: 614-292-3769
The Ohio State University
151 West Woodruff Avenue
Columbus, OH 43210-1350

Co-PI: Dr. Yang Han

Project Period: October 1, 2018–March 31, 2022
Submission Date: June 11, 2022

DUNS 832127323

Contents

1 Project Overview

1.1 Major Goal of Project

The objectives of this project are to develop a cost-effective design and fabrication process of a novel transformational membrane and its membrane modules that capture CO_2 from coal derived syngas. We will synthesize transformational membranes, scale up the membrane to a prototype size of 14 inches wide by 20 feet in continuous roll-to-roll fabrication, fabricate at least 9 prototype membrane modules (each with about 2.5-inch diameter, 14-inch length, and 800 cm^2 membrane area) for testing with simulated syngas at OSU to achieve capture with at least 95% CO_2 purity. The membrane modules will be in commercial spiral-wound (SW) configuration with a minimal pressure drop (<0.103 bar/meter (1.5 psi/meter)).

This project will be performed over two budget periods:

Budget Period 1 (BP1):

In BP1, we will synthesize and characterize novel transformational membranes. We will synthesize the membranes by taking the following seven approaches: (1) Use sterically hindered amines as CO_2 carriers; (2) Incorporate ethylene oxide moieties in membrane; (3) Investigate the effects of polyethylene glycol and dimethyl ether of polyethylene glycol molecular weights, (4) Add amine-containing hydroxyethyl moieties in membrane; (5) Incorporate nanofillers; (6) Synthesize higher MW polyalcohols (>2,000 kDa); and (7) Synthesize higher MW polyamines (>2,500 kDa). In addition, we will perform a high-level techno-economic analysis (TEA).

Budget Period 2 (BP2):

In BP2, we will synthesize the optimized membrane; scale it up to the prototype size of about 14 inches wide by at least 20 feet in continuous roll-to-roll fabrication; fabricate at least 9 prototype membrane modules, each with about 2.5-inch diameter, 14-inch length, and 800 cm^2 membrane area; and test 3 modules in series each time at ~34 L/min (34 slpm or 1.2 ft^3/min) simulated syngas flow. Using the modules, 3 in series each time, the Recipient will conduct parametric testing and continuous steady-state operation for at least 200 hours using simulated syngas, all to capture CO_2 with at least 95% CO_2 purity. The TEA will be updated with membrane data obtained.

1.2 Statement of Project Objectives (SOPO)

The project tasks are described in the following paragraphs.

Task 1.0 – Project Management and Planning

The Recipient shall manage and direct the project in accordance with a Project Management Plan (PMP) to meet all technical, schedule and budget objectives and requirements. The Recipient will coordinate activities in order to effectively accomplish the work. The Recipient will ensure that project plans, results, and decisions are appropriately documented and project reporting and briefing requirements are satisfied.

The Recipient shall update the Project Management Plan 30 days after award and as necessary throughout the project to accurately reflect the current status of the project. Examples of when it may be appropriate to update the Project Management Plan include: (a) project management policy and procedural changes; (b) changes to the technical, cost, and/or schedule baseline for the project; (c) significant changes in scope, methods, or approaches; or (d) as otherwise required to ensure that the plan is the appropriate governing document for the work required to accomplish the project objectives.

Task 2.0 – Synthesis of Transformational Membranes

The Recipient will investigate the following seven approaches in the synthesis of the membranes: (1) Use sterically hindered amines as CO_2 carriers to increase CO_2 permeance; (2) Incorporate ethylene oxide moieties in the membrane to increase CO_2 permeance at high CO_2 partial pressure; (3) Investigate the effects of polyethylene glycol and dimethyl ether of polyethylene glycol molecular weights on CO_2 permeance and CO_2/H_2 selectivity, (4) Add amine-containing hydroxyethyl moieties in the membrane to increase CO_2 permeance at high CO_2 partial pressure; (5) Incorporate nanofillers in the membrane to increase free volume and hence CO_2 permeance in addition to mechanical enforcement; (6) Synthesize higher MW polyalcohol (>2,000 kDa); and (7) Synthesize higher MW polyamines (>2,500 kDa).

Task 3.0 – Membrane Characterization

The purpose of this task is to guide membrane fabrication to achieve the BP1 success criteria, and to obtain initial design parameters for the systems and cost analysis. The characterization includes:

Subtask 3.1 – Morphology of Membranes

The morphology of membranes will be characterized via scanning electron microscopy (SEM) of (cold) fracture cross-sections.

Subtask 3.2 – Transport Properties

The Recipient will measure the CO_2 and H_2S permeances and CO_2 and H_2S selectivities vs. H_2 for synthesized membranes using simulated syngas, i.e., about 4% water vapor and 6,000 ppm H_2S with balance of CO_2 (~40%) and H_2, at ~110°C with 31.7 bar syngas feed (12.5 bar CO_2) and 31.7 bar syngas retentate (1.25 bar CO_2).

Subtask 3.3 – Membrane Stability

CO_2 and H_2S permeances and CO_2/H_2 and H_2S/H_2 selectivities versus time will be obtained over 20 hours to evaluate membrane stability.

Subtask 3.4 – Chemical Composition

The chemical composition of a membrane will be characterized by FTIR (Fourier transform infrared) spectrometry and NMR (nuclear magnetic resonance) spectrometry. By FTIR, the primary and secondary amines can be identified by characteristic N–H bond stretching absorptions in the 3300–3500 cm^{-1} range of the infrared spectrum. By NMR, the H atom on the nitrogen site can be differentiated from that on an alkyl group.

Task 4.0 – Preliminary Techno-Economic Analysis

The Recipient will complete a high-level TEA, based on initial data, to study critical system and cost parameters. This study will assure the feasibility of achieving the lowest COE increase and optimize the membrane process with respect to the system parameters. This effort will also guide process and prototype membrane development. The Recipient will update the TEA with new membrane data as it becomes available and submit it at the end of BP1.

Task 5.0 – Optimized Membrane Synthesis

Based on the BP1 results, the Recipient will identify the best performing membrane based on improvements in permeance and selectivity with respect to the baseline. The Recipient will optimize the membrane synthesis to achieve the best performance in accordance with the success criteria for BP2, including the continued investigation of the synthesis approaches described in Task 2.0 and the down-selection of these synthesis approaches.

Task 6.0 – Optimized Membrane Characterization

This task is to guide membrane fabrication to the BP2 success criteria, and to obtain optimized design parameters for the TEA. The characterization methods and approach are the same as those for Task 3.0 in BP1, with membrane stability to be evaluated over at least 100 hours.

Task 7.0 – Optimized Membrane Scale-up Fabrication

The Recipient will scale up the optimized membrane to the prototype size of 14 inches wide for ~20 feet in continuous roll-to-roll fabrication using the Recipient's pilot membrane machine.

Task 8.0 – Optimized Scale-up Membrane Characterization

The scale-up membrane will be characterized using the methods and approach described in Task 3.0, with membrane stability to be evaluated over at least 100 hours.

Task 9.0 – Prototype Membrane Module Fabrication

The optimized scale-up membrane will be used to fabricate at least 9 prototype membrane modules in the commercial spiral-wound configuration each with about 2.5-inch diameter by 14-inch length, i.e., ~800 cm^2 area. The modules are targeted for a minimal pressure drop (<0.103 bar/meter (1.5 psi/meter)).

Task 10.0 – Prototype Membrane Module Testing

The Recipient will use the membrane modules fabricated in the Task 9.0 for testing using the simulated syngas and a membrane module testing unit, i.e., a larger gas permeation unit that can accommodate at least one and up to three membrane modules. This task is to obtain high membrane module performance targeting for about 350 GPU CO_2 permeance and 140 CO_2/H_2 selectivity at ~110°C with 31.7 bar syngas feed (12.5 bar CO_2).

Task 11.0 – Parametric Testing with Prototype Modules in Series

The Recipient will conduct the parametric testing of the membrane modules, 3 in series each time, using the simulated syngas described earlier at ~34 L/min (34 slpm or 1.2 ft^3/min) and the membrane module testing unit described above. Variables including operating pressures at 20–32 bar and temperatures at 100–120°C will be tested to identify conditions for the continuous steady-state operation.

Task 12.0 – Continuous Steady Operation with Modules in Series

The Recipient will conduct the test at ~34 L/min (34 slpm or 1.2 ft^3/min) steady state with the conditions identified from the parametric testing conducted in Task 11.0. The targets are to capture CO_2 with at least 95% CO_2 purity along with a minimal pressure drop (<1.5 psi/m or 0.103 bar/m) for 200 hours. FTIR and NMR will be used to identify any changes of membrane composition after the 200-hour test. In addition, XPS and energy-dispersive X-ray analysis spectroscopy (EDX) may also be used, if needed.

Task 13.0 – Final Updated Techno-Economic Analysis

The Recipient will update the TEA based on the results from Tasks 10.0–12.0 for CO_2 capture from the simulated syngas. The final TEA will provide the lowest COE increase achievable through the proposed membrane technology. The final TEA will be prepared in accordance with SOPO Appendix A.

Task 14.0 – State Point Data Table

The Recipient will prepare and submit the final State Point Data Table following the format and containing the information and data as defined in SOPO Appendix B.

Task 15.0 –Technology Maturation Plan

The Recipient will prepare and submit a Technology Maturation Plan (TMP) in accordance with SOPO Appendix C.

Task 16.0 – Environmental Health & Safety Risk Assessment

The Recipient will prepare and submit an EH&S Risk Assessment in accordance with SOPO Appendix D.

2 Summary of Project Accomplishments

2.1 Technical Progress

2.1.1 Task 1 – Project Management and Planning

Summary

- The PMP was negotiated and updated with NETL's input.
- Project kick-off meeting was held to provide a comprehensive project overview to NETL.
- All participating students and researchers were appointed, performed productive research, and were contributing to the project.
- Training in technical reporting was provided and improved.
- Project tasks were carried out and significant progress was made.
- Project updates have been communicated with the project officer on a monthly basis.
- The BP 1 Project Review Meeting was held and the Continuation Application to BP2 was approved.
- Due to the coronavirus COVID-19 pandemic, our labs were shut down from March 18 to June 21, 2020. All researchers remained to telework for the project tasks.
- Upon the lab reopening since June 22, we have resumed our experimental activities quickly owing to the good planning of the experiments during the teleworking period.
- The Final TEA Report, Final TMP Report, and EH&S Report have been submitted to DOE-NETL. These topical reports will be further revised and finalized after incorporating NETL's input and review comments.
- A no-cost time extension has been requested by NETL due to a new policy that requires the review of the final TEA report before the end of the project. This process has been initiated, and the new project end date will be determined by NETL.
- The Project Close-Out Meeting was held on December 2, 2021.

2.1.2 Task 2 – Synthesis of Transformational Membranes

Summary

- A robust polymer network was synthesized from a high MW polyalcohol and aminosilane to host the low MW CO_2 carriers.
- Carbon-based inorganic nanofiller was synthesized to enable high-pressure operation of the polymeric membrane.
- Aminoacid salts with low to moderate degrees of steric hindrance were synthesized to serve as CO_2-reactive carriers for CO_2/H_2 separation.
- Composite membranes were synthesized, and the compositions were tailored for different CO_2 partial pressure ranges.

Crosslinked Polymer Network via Aminosilane

A water-swellable polymer network that can retain high content of water is greatly preferable for the synthesis of highly CO_2-selective amine-containing facilitated transport membranes [1]. At the beginning of BP 1, such a water-swellable polymer network was synthesized by crosslinking a high MW polyalcohol with dialdehyde [2-5]. The resultant acetal linkage ($R_2C(OR')_2$) can form hydrogen bond with water, which bestows the crosslinked polymer a high water uptake [6-9]. The sorption of water also swells the polymer network and provides free volume for gas diffusion.

An improved approach to crosslink the polyalcohol is to utilize aminosilane. An aminosilane is defined as a tetravalent single bonded Si with at least one substituent containing amino group(s). As shown in Figure 2.1 (a), the aminosilane undergoes hydrolysis to afford silanol in the presence of an acid [10]. A condensation reaction between polyalcohol and silanol occurs (Figure 2.1 (b)) to make –C–O–Si– linkage, which crosslinks the polyalcohol chains as well as grafting amino groups onto the polymer network [11,12]. This approach is more versatile than the acetal synthesis in that a variety of amine structures can be introduced into the polymer network. Three amine structures were employed in this BP, which were (1) a primary amino group ($-NH_2$), (2) an ethylenediamine group ($-NH-(CH_2)_2-NH_2$), and (3) a tertiary amino group ($-N(CH_3)_2$), respectively. Hereafter, they are denoted as 1°, 2°, and 3° amines, respectively.

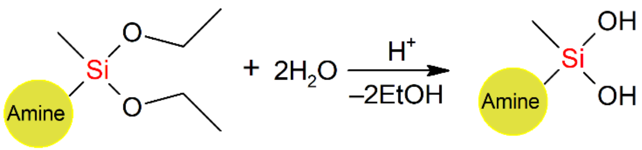

(a) Hydrolysis of aminosilane

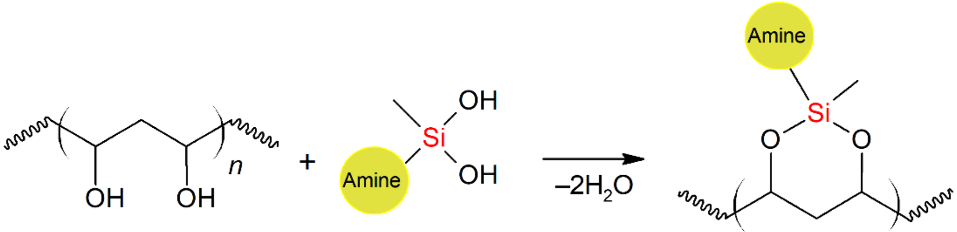

(b) Main crosslinking reaction

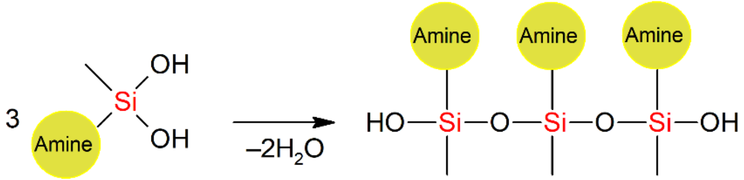

(c) Side reaction: condensation of silanol

Figure 2.1. Crosslinking reaction of polyalcohol and aminosilane: (a) hydrolysis of aminosilane, (b) crosslinking of polyalcohol by silanol, and (c) self-condensation of silanol. In the reaction scheme, 〰 represents a polymer chain.

It was later proven that the 3° amino group grafted on the polyalcohol could enhance its CO_2 permeance. In order to study the coupling reaction between the aminosilane and polyalcohol, the same 3° amino group was employed but the functionality of the silane was varied. As shown in

Figure 2.2, monodentate, bidentate, and tridentate aminosilanes containing the amino group were used. The monodentate aminosilane cannot crosslink the polymer; rather, it can only graft amine as pendent groups. The bidentate and tridentate aminosilanes are capable of crosslinking the polymer; the tridentate silane introduces a higher crosslinking degree. The three aminosilanes are denoted as AS-1, AS-2, and AS-3 hereafter.

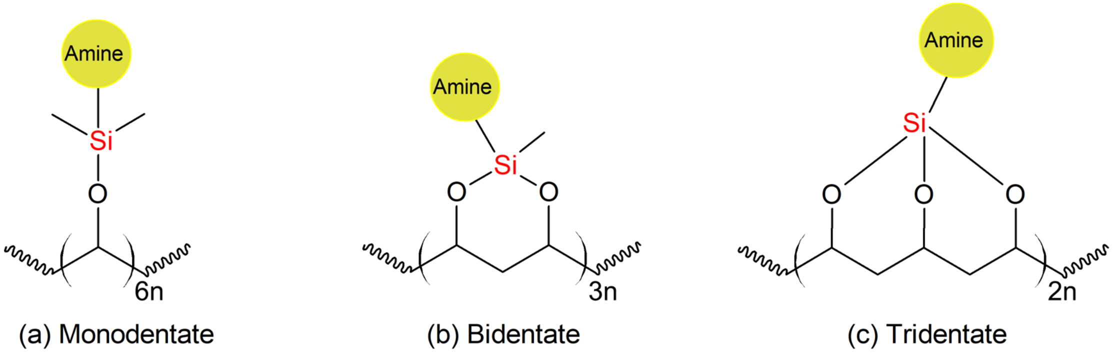

Figure 2.2. Crosslinking reaction of polyalcohol with (a) monodentate (AS-1), (b) bidentate (AS-2), and (c) tridentate aminosilanes (AS-3).

It should be noted that a self-condensation reaction can occur for the silanol (Figure 2.1 (c)), which leads to the formation of siloxane (–Si–O–Si–). This structure not only reduces the effective crosslinking of the polyalcohol, but also results in certain heterogeneity in the polymer network. In order to suppress this side reaction, the hydrolysis (Figure 2.1 (a)) and condensation (Figure 2.1 (b)) rates of 2 mol% aminosilane was studied in a mixture of ethanol-d_6 and H_2O (95/5 wt./wt.) at 25°C. The pH was adjusted in the range of 3–10 by acetic acid-d_4. The transient concentrations of alkoxy and alkanol were measured by ^{1}H nuclear magnetic resonance (NMR) to trace the reaction kinetics. As seen in Figure 2.3, the hydrolysis and condensation rates both depended strongly on the pH. In general, an acidic environment favored the hydrolysis while a basic condition favored the condensation. In comparison, AS-1 exhibited a very low rate of condensation because it could only form dimers. AS-3, however, tended to condensate, likely due to the more silanol groups. Based on this set of data, an aminosilane solution can be devised in which the rate of hydrolysis is substantially greater than that of the condensation. At a pH of 6, the rates of hydrolysis were at least two orders of magnitude higher than the rates of condensation for AS-1 and AS-2, respectively. Therefore, relatively stable silanol solutions could be formed to crosslink the polyalcohol. For AS-3, the pH had to be reduced to 5 in order to obtain a stable solution.

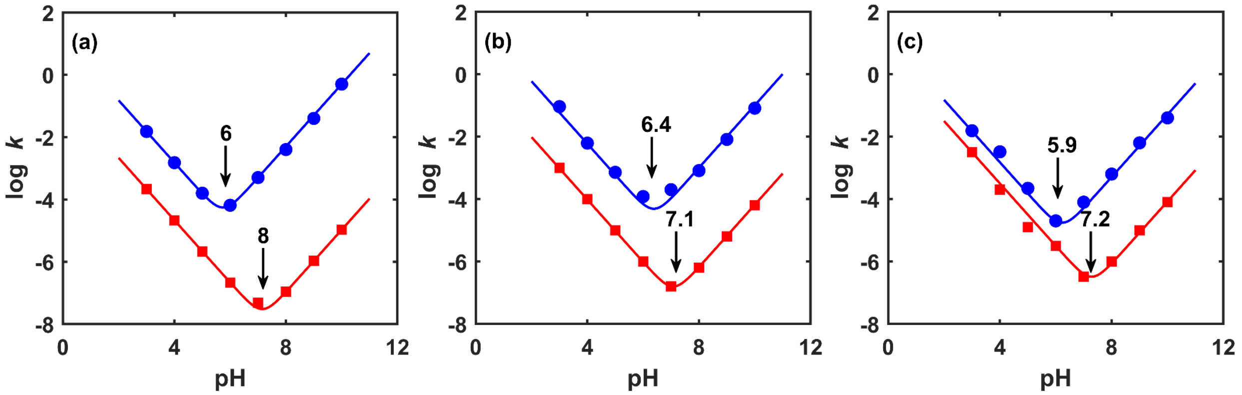

Figure 2.3. Hydrolysis (●) and condensation (▲) rates of (a) AS-1, (b) AS-2, and (c) AS-3 in ethanol/water mixture (95/5 wt./wt.) at 25°C. The pH was adjusted by acetic acid-d_4.

Experimentally, the pH of an ethanol/water mixture (95/5 wt./wt.) was adjusted to 5 or 6 via acetic acid. The aminosilane was added with stirring to yield a 2 wt.% solution. The solution was kept under stirring for 5 min to allow for the formation of silanol. Certain amount of the solution was then added in an 8 wt.% high MW polyalcohol aqueous solution at room temperature. After a homogenization for 5 min, extra acetic acid was added to yield a pH of 4. The system was then refluxed at 80°C for 2 h. In order to further tighten up the polymer network, an extra portion of the hydroxyl groups on the polyalcohol was converted to acetal linkages via a dialdehyde containing short carbon bridge. Experimentally, certain amount of the dialdehyde solution (40 wt.%) was added into the mixture under vigorous agitation. The final crosslinking was carried out at 80°C for 2 h. The pH of the gel was then adjusted to 12 by strong basic anion-exchange resin.

The degree of crosslinking was characterized by a solvent extraction method. The synthesized gel solution was poured into a borosilicate Petri dish and dried at room temperature. The resultant dried film was peeled off and cured at 120°C for 6 h. This crosslinked film was kept in reverse osmosis (RO) water at room temperature. The solvent was replaced every 24 h and its absorbance was measured by a UV–Vis spectrophotometers (UV-1700, Shimadzu, Japan) until no further change. The ratio of the remaining weight to the original dry weight was defined as the crosslinking degree. The results for four crosslinkers are shown in Figure 2.4. As seen, the dialdehyde crosslinker rendered 24.7% of the polyalcohol crosslinked. By adding additional AS-1, the crosslinking degree reduced to 22.4%. As discussed above, AS-1 could not crosslink the polymer. The reduction in the crosslinking degree was due to the leaching-out of the siloxane dimer. By using AS-2, the crosslinking degree increased to 34.9%, which was close to the calculated amount added experimentally. For AS-3, although it contained the highest site for crosslinking, the measured crosslinking degree was only 31.2%, suggesting the occurrence of self-condensation. The consequence of the different crosslinked polymer networks will be discussed in Section 2.1.3.

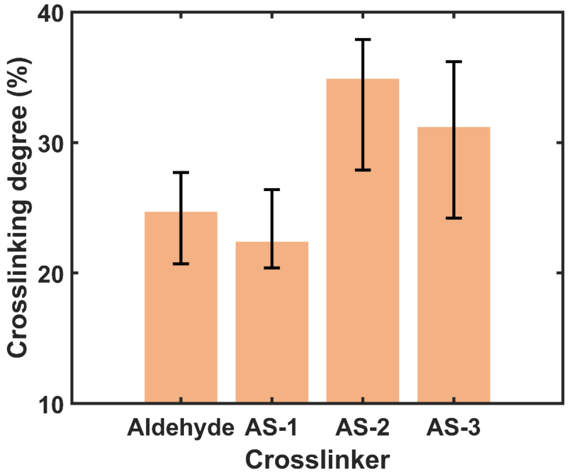

Figure 2.4. Crosslinking degrees of polyalcohol with different crosslinkers. From left to right: dialdehyde, dialdehyde+AS-1, dialdehyde+AS-2, dialdehyde+AS-3.

The basicity of the 3° amino group was also studied by a series of bidentate aminosilane. As shown in Figure 2.5, *N*,*N*-dimethyl, *N*,*N*-diethyl, and *N*,*N*-diisopropyl groups were grafted on the 3° amino site. Also included in Figure 2.5 are the pKa values of the three aminosilanes, which are 10.16, 10.98, and 11.70, respectively. A bulkier alkyl substituent increases the basicity of the amino group due to its enhanced induction effect along with its increased electron donating ability. The difference in the basicity, therefore, will affect their reaction with CO_2. The three aminosilanes will be denoted as AS-Me, AS-Et, and AS-Pr hereafter.

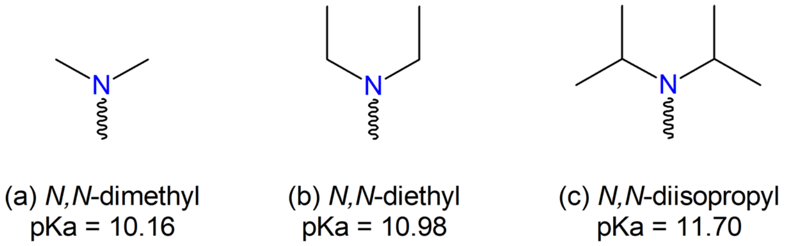

Figure 2.5. Chemical structures and pKa values of aminosilanes containing (a) *N*,*N*-dimethyl, (b) *N*,*N*-diethyl, and (c) *N*,*N*-diisopropyl groups.

Synthesis of Reinforcement Filler

Based on the crosslinking mechanism described above, the bridges created between the polymer chains are not rigid ones, but flexible sequence of –C–C– and –C–O–Si–. Although some of the polar linkages are capable of hydrogen bonding with water or amine, the polymer network is still largely rubbery [13]. A low glass transition temperature (T_g) of 45–50°C was measured by differential scanning calorimetry (DSC, PerkinElmer) in dry state. The presence of water vapor is likely to further soften the polymer chain due to the plasticizing effect [14]. In this project, the designated operating temperature for the membrane is at 107°C. At this temperature, the crosslinked polymer network is rubbery. In this case, the hydrostatic compression induced by the high syngas pressure reduces the polymer free volume, thereby a reduced gas diffusivity through the polymer [6,15]. In order to mitigate the membrane compaction, a perforated carbon nanosheet was synthesized and dispersed in the polymer network as reinforcement fillers.

In BP1, an ongoing effort was spent to synthesize reinforcement carbon nanosheet in house based on a top-down method. This method can yield quality reinforcement filler from cheaper raw materials, thus reducing the membrane cost. However, the purification of the carbon material involved repetitive centrifugation and dialysis. Typically, it took seven days for the completion of the washing process, including oxidation reaction followed by drying, to obtain 0.5 g of the carbon materials. Obviously, this method was inefficient and time consuming to deal with large-scale synthesis. Therefore, a tangential filtration method was later developed to improve the process efficiency.

Figure 2.6 (a) illustrates the bulk synthesis of the carbon nanosheet with an improved procedure. A cheap graphitic material was firstly oxidized in a mixture of strong oxidant and deintercalation agents. The oxidation reaction occurred between the intercalated carbon sheets, where oxygen-containing functional groups were introduced onto the carbon lattice. Then, carbon nanosheets were exfoliated from the oxidized carbon material via gentle sonication. The excess reagents and byproducts evolved in the process were removed by a tangential filtration device developed in house.

A partial oxidation method was then adopted to perforate the carbon-based nanosheets. This method was chosen to preserve the oxygen-containing polar functional groups, thereby an improved dispersity in the hydrophilic polymer matrix. As shown in Figure 2.6 (b), the nanosheets were firstly dispersed in RO water (ca. 1 mg/ml) by an ultrasonication probe. This step induced fragmentation of the nanosheets as well as introducing a small number of structural defects. Nitric acid was then added slowly into the dispersion with caution. The mixture was further ultrasonicated for 30 min, then refluxed at room temperature for 1 h. The resultant mixture was purified via the tangential filtration device to remove the remaining acid. The final concentration of the perforated nanofiller was measured by the UV–Vis spectrophotometer, with a typical value of ca. 1 mg/mL.

(a) Bulk synthesis of carbon nanosheet

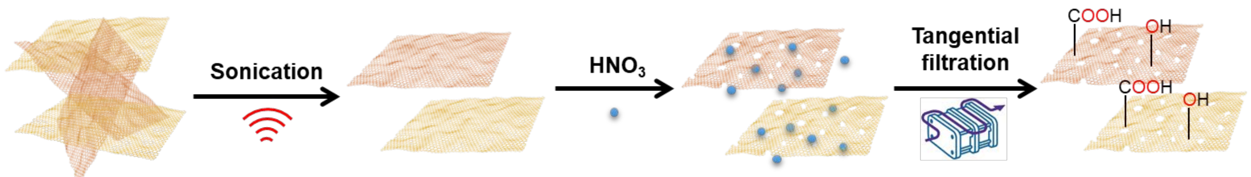

(b) Perforation of carbon nanosheet

Figure 2.6. Schematic of the synthesis of perforated carbon nanosheet: (a) bulk synthesis of carbon nanosheet and (b) perforation via partial oxidation.

The tangential filtration setup is schematically shown in Figure 2.7. The crude product was delivered to a permeation cell by a peripheral pump, where the liquid stream was treated by an ultrafiltration (UF) membrane. The water-soluble impurities permeate through the membrane while the carbon material was retained. The retentate containing the carbon material was recycled back to the feed container. RO water was added in the feed container in batches to make up for the permeation.

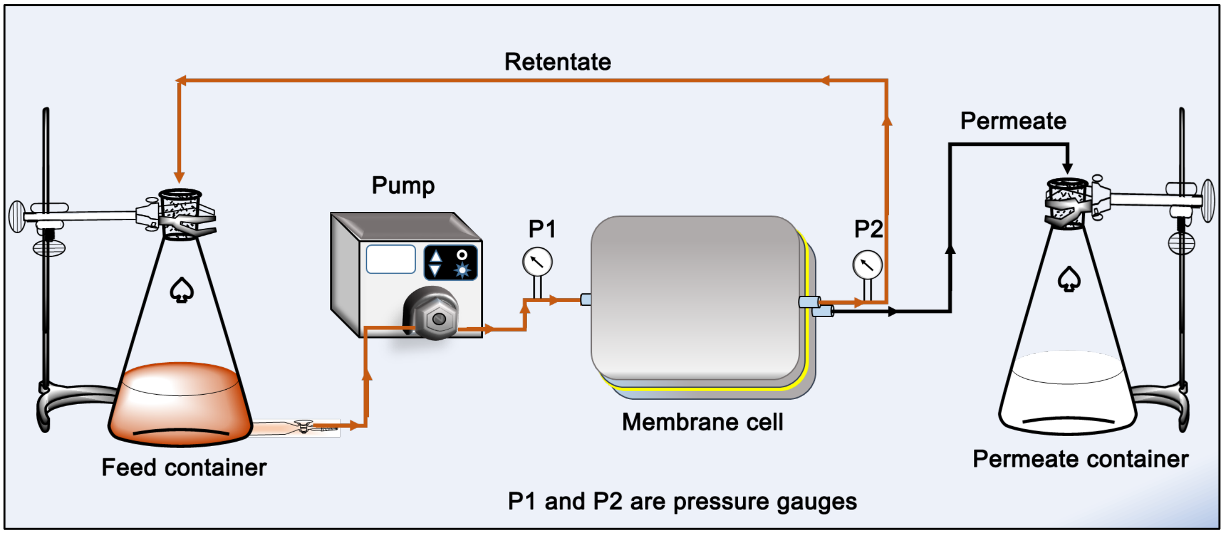

Figure 2.7. Schematic representation of the tangential filtration setup.

Two different types of UF membrane were used for the purification process, namely UF1 and UF2. These two membranes differed in the pore size and hydrophilicity. Due to the hydrophilic nature of the carbon material, the UF membranes were prone to fouling, which significantly reduced the permeate flux. The more hydrophobic UF1 showed a better resistance to fouling compared to UF2. Further, the backwashing of the UF1 was faster and easier to conduct than UF2. However, a loss of the carbon material was observed when UF1 was used. As shown in Figure 2.8, the permeate obtained from UF1 was tainted. In comparison, the permeate achieved via UF2 was completely transparent, which suggested no loss of the carbon material. Therefore, UF2 was chosen for the process optimization. Eventually, a production capacity of 2.8 g per week was achieved.

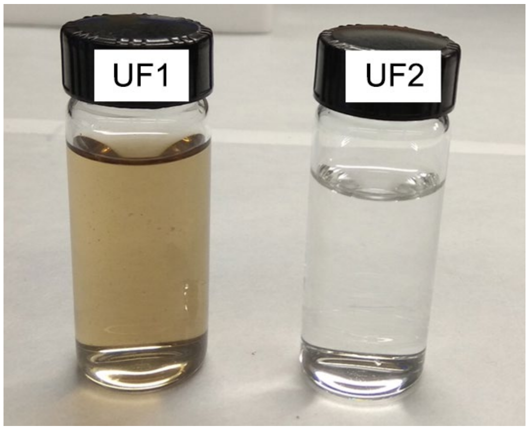

Figure 2.8. Image of the permeates of membranes UF1 and UF2.

In order to confirm the formation of single sheet of the nanofiller, atomic force microscopy (AFM) analysis was carried out. The as-prepared nanofiller was diluted by water and drop cast onto freshly cleaved mica substrate. The sample was dried in a laminar hood for 4 h before the measurement. The AFM images, along with the height profiles, of two different sheets are shown in Figure 2.9. The AFM images reveal that the sheets were of variable size and shape. Based on the height profiles, the thickness of the sheet was around 1.1–1.2 nm, which indicated that the sheets were fully exfoliated to its monolayer form. The sheet width of one of the monolayers (sheet 'a' in Figure 2.9) is ca. 450 nm while the sheet 'b' displayed a sheet width of 280 nm. This indicated the presence of different sizes of the sheets in the dispersion.

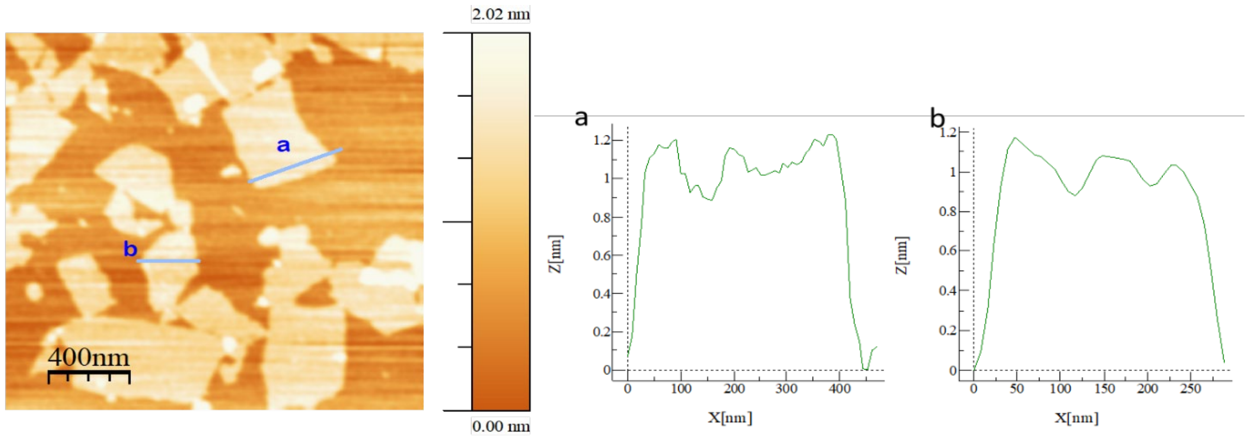

Figure 2.9. AFM image of the carbon material along with height profiles.

The textural properties of the synthesized carbon material were characterized by X-ray powder diffraction (XRD, Rigaku SmartLab), in which a Cu K_{α} X-ray with a wavelength of 1.54 Å was used. The diffractograms are shown in Figure 2.10. For the ease of comparison in this figure, the spectra of the carbon materials after exfoliation and perforation are offset from the zero count by 5×10^3 and 1×10^4 counts, respectively, so that the overlap of spectra is avoided. As seen, the diffraction pattern of the material after oxidation only contained a noteworthy (002) peak at 2-theta of 9.61°, corresponding to a d-spacing of 9.22 Å. This suggested the successful attachment of the hydrophilic group to the interplane spacing of the carbon material. After exfoliation, this feature completely disappeared, suggesting the delamination of the oxidized carbon material into monosheets. For the material after perforation, a large increase in the low-angle scattering was observed, which suggested the presence of pores (defects) in the monosheets. The broadening near the low-angle range was analyzed by the Scherrer equation, which indicated an average in-plane crystal size of ca. 10 nm [16]. This size could be interpreted as the distance between pores on the basal plane of the carbon nanosheet. The pores on the carbon nanosheets reduced the transverse diffusional resistance, thereby enhanced the gas permeance.

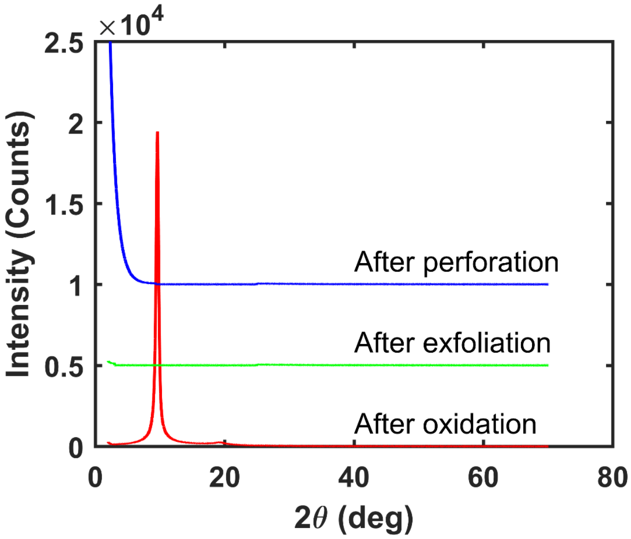

Figure 2.10. XRD diffractograms of the carbon material after oxidation, exfoliation, and perforation, respectively.

The pore geometry of the perforated carbon nanosheet was also characterized by AFM. Figure 2.11 shows the AFM image of the perforated carbon material. A clear round pattern of the porous structure was observed. Three pores, labeled as ‘a’, ‘b’ and ‘c’, were measured and the height profiles are also shown in Figure 2.11. The profiling of the pores suggested that the diameters of the pores were in the range of 8–12 nm (80–120 Å), which was at least two orders of magnitude larger than the kinetics diameters of CO_2 (3.30 Å) and H_2 (2.89 Å). The pores allow for the diffusion of light gases across the carbon nanosheet, which reduce the path length of the transverse diffusion along the basal plane of the nanosheet. It should be noted that the lateral resolution of the AFM was ca. 10 nm due to the convolution. Therefore, the AFM image does not exclude the existence of pores with a size of a few nanometers. In accordance with the X-ray diffraction results discussed in Figure 2.10, we estimated that the interpore spacing should be ca. 10 nm. The estimated pore size and interpore spacing led to a porosity of 19.6% for square arranged pores while 22.7% for hexagonally arranged pores.

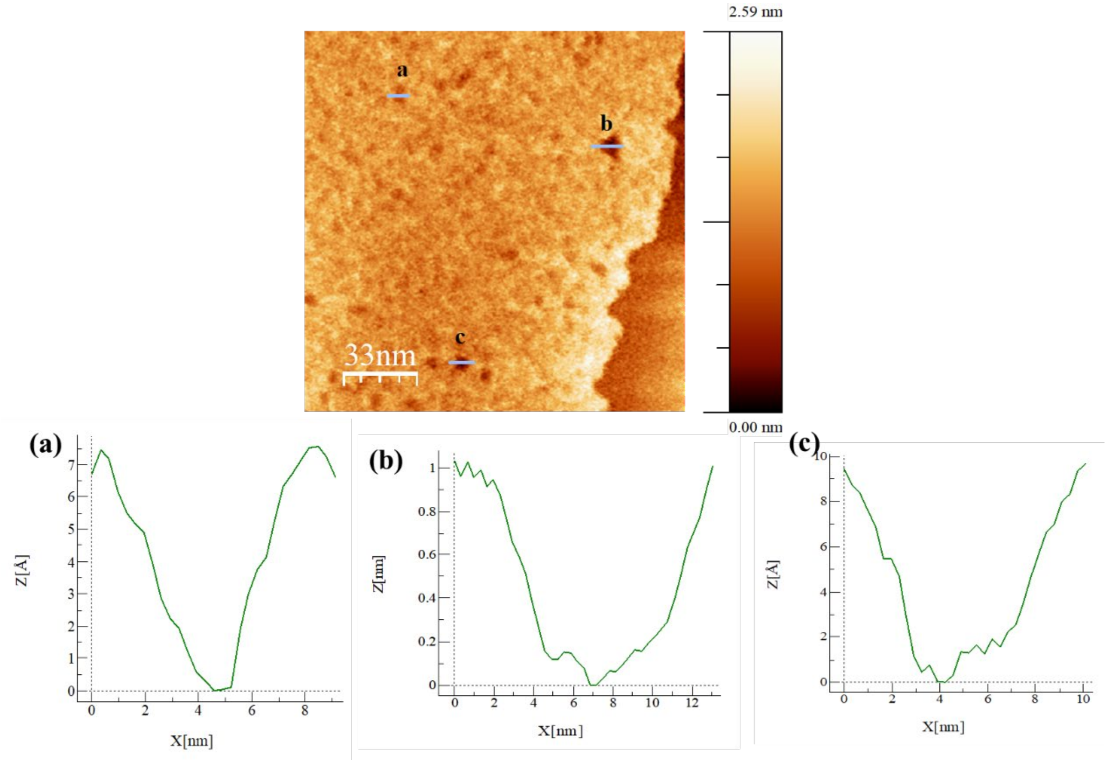

Figure 2.11. AFM image of carbon material perforated by HNO_3 and the height profiles of the porous regions.

Further, the synthesized material was characterized by dynamic light scattering (DLS) to obtain its width distribution. DLS is a technique that can elucidate particle size (average hydrodynamic diameter) distribution in a dispersion of particles. The result shown in Figure 2.12 indicated a bimodal sheet width distribution of the carbon material. The intensity profile highlighted the presence of two peaks, a small peak (which could be attributed to the presence of very small nanosheets) corresponding to an average diameter of 82–100 nm and a primary peak distributed in the range of 205–407 nm (88 %).

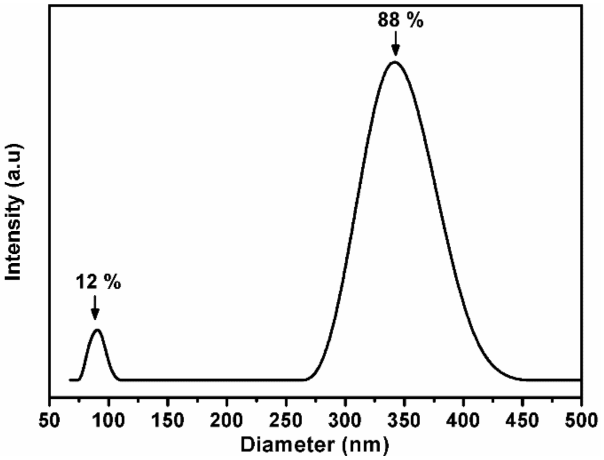

Figure 2.12. Sheet width distribution of the carbon material measured by DLS.

In order to further analyze the change of oxygen-containing groups before and after the perforation of the nanosheets, X-ray photoelectron spectroscopy (XPS, Kratos AXIS Ultra XPS) was conducted to explore the chemical environment of carbon atoms. All the spectra were calibrated with a charge reference to adventitious C 1s peak at 284.5 eV. Figure 2.13 shows the deconvoluted C 1s regions of both materials. An analysis of Figure 2.13 (a) indicated that, before perforation, 43% of the carbon was unoxidized (C–C), 48% was attributed to the epoxide linkage (C–O–C), and the C=O and O–C=O accounted for the remaining 10% carbon species. After the perforation treatment, the amount of epoxide linkage reduced slightly to 44% while the C–C linkage increased to 46%; the intensities of C=O and O–C=O linkages were nearly unchanged. Consequently, the perforation treatment conducted in this work created defects, but still retained a substantial number of polar groups (epoxide, hydroxyl, and carboxylic groups). These hydrophilic groups helped to stabilize the perforated nanosheets in its water dispersion, and an excellent dispersity in the hydrophilic polymer network was observed.

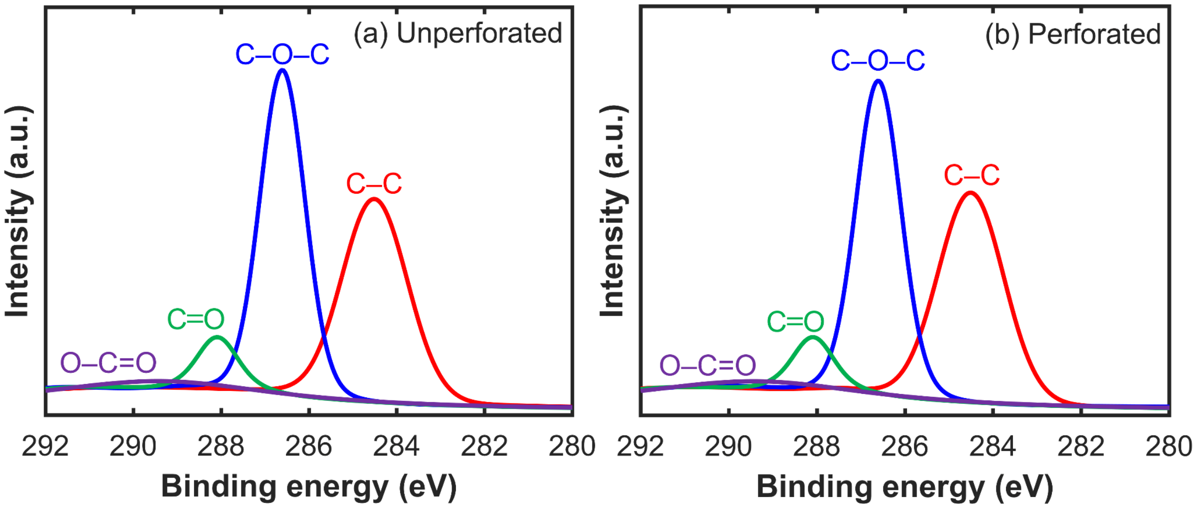

Figure 2.13. C 1s regions of XPS elemental analysis of (a) unperforated and (b) perforated nanosheets.

Enhancement of Chemi- and Physi-Sorption of CO_2

The crosslinked polymer network and reinforcement filler mainly address the membrane formation issue, where the membrane matrix intrinsically has a low H_2 solubility. This section, however, addresses our strategies to enhance the CO_2 sorption, especially at elevated temperature and pressure. Based on the mechanism of CO_2–carrier interaction, we categorize them as chemisorption carrier and physisorption enhancer.

1. CO_2 carrier based on enhanced chemisorption

The reversible amine–CO_2 reaction was used to enhance the chemisorption of CO_2. Based on the amine structure, an amine can be either sterically hindered or unhindered. A sterically hindered amine is defined as either a primary amine in which the amino group is attached to a tertiary carbon, or a secondary amine in which the amino group is attached to at least one secondary or tertiary carbon [17]. With a bulky substituent, sterically hindered amines are advantageous over conventional unhindered amines for CO_2 capture due to their high CO_2 loading capacity [5,18]. For an unhindered amine, it reacts with CO_2 to form a zwitterion, which is deprotonated by another amine to form a carbamate, which is stable:

$$CO_2 + R–NH_2 \rightleftharpoons R–NH_2^+–COO^-$$
$$R–NH_2^+–COO^- + R–NH_2 \rightleftharpoons R–NH–COO^- + R–NH_3^+$$

The sum of these two reaction is as follows:

$$CO_2 + 2\ R–NH_2 \rightleftharpoons R–NH–COO^- + R–NH_3^+$$

Overall, 2 moles of amine are needed for 1 mole of CO_2. If the amine is hindered, the carbamate is unstable and subject to hydrolysis, resulting in the formation of bicarbonate and the regeneration of the amine:

$$CO_2 + R_1–NH–R_2 \rightleftharpoons R_1R_2–NH^+–COO^-$$
$$R_1R_2–NH^+–COO^- + H_2O \rightleftharpoons R_1R_2–NH_2^+ + HCO_3^-$$

The sum of these two reaction is as follows:

$$CO_2 + R_1–NH–R_2 + H_2O \rightleftharpoons R_1R_2–NH_2^+ + HCO_3^-$$

Overall, 1 mole of amine can fixate 1 mole of CO_2. Here, R, R_1 and R_2 represent alkyl substituents. In BP1, an aminoacid containing a moderately hindered amino group was used to synthesize a mobile carrier. Naturally, the aminoacid exists as a zwitterion and is inactive to CO_2. Therefore, an aliphatic multi-amine is used to liberate the sterically hindered amino group, which resulted in an aminoacid salt that is nonvolatile. This CO_2 carrier is referred as Compound I hereafter.

2. CO_2 carrier utilizing both chemi- and physi-sorption

An alkanolamine was also used as the mobile carrier. This compound contained two hydroxyethyl groups in the structure with multi-amine moiety. The hydroxyethyl groups provide a CO_2 affinity for enhanced physisorption, while the multi-amine reacts with CO_2. Therefore, this alkanolamine has a high active-site density per molecular weight. It is referred as Compound II hereafter.

3. CO_2-philic moiety based on enhanced physisorption

Even though a CO_2 molecule is non-polar as a whole, the uneven distribution of charges inside grants the molecule a quadrupole moment [19]. It is known that the polar ethylene oxide group (–CH_2CH_2–O–) or ether linkage (–C–O–C–) possess a high affinity to CO_2 via the quadrupole-quadrupole interaction as shown in Figure 2.14 [20]. Due to the uneven distribution of charge inside the molecules, the carbon atoms carry partial positive charges while the oxygen atoms carry partial negative charges. Overall, there are more attractive electrostatic interactions between oppositely-charged atoms than the repulsive interactions between like-charged atoms. Therefore, a high CO_2 solubility can be achieved by the preferential interaction. Based on this rational, we used an ether-rich oligomer as a CO_2-philic moiety to enhance the physisorption of CO_2, especially at high CO_2 partial pressure. This oligomer is referred as Compound III hereafter. Table 2.1 summaries the CO_2 carrier and/or sorption enhancer developed in BP1.

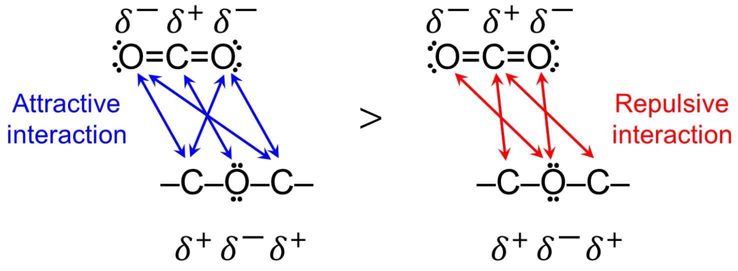

Figure 2.14. Quadrupole–quadrupole interactions between a CO_2 molecule and an ether linkage.

Table 2.1. Summary of CO_2 carriers and/or sorption enhancers in BP1.

Compound	Nature	CO_2 interaction mechanism
I	Sterically hindered aminoacid salt	Chemisorption/Reactive diffusion
II	Multifunctional alkanolamine	Chemi-and physi-sorption/Reactive diffusion
III	Ethylene oxide oligomer w/ various MWs	Physisorption

Composite Membrane Synthesis

Amine-containing facilitated transport membranes (FTMs) were synthesized by the following steps.

The nanofiller dispersion was added to the polymer solution via a 10-µL glass capillary tube under vigorous agitation, aiming for a low to medium filler loading in the final total solid of the coating solution. The mixture was transferred to a 15-mL conical centrifuge tube, in which it was homogenized by a 1/8″ microtip sonication probe with a 50% amplitude until uniformly dispersed. The sonication was carried out in an ice bath. The water introduced by the nanofiller dispersion was then evaporated by a nitrogen purge.

Certain amount of the CO_2 carrier and/or sorption enhancer solution was incorporated in the dispersion to form the coating solution. After centrifugation at 8000 × *g* for 3 min to remove any air bubbles, the coating solution was coated on a nanoporous polysulfone substrate by a GARDCO adjustable micrometer film applicator (Paul N. Gardner Company, Pompano Beach, FL) with a controlled gap setting. The membrane was dried in a fume hood at room temperature for 30 min, and then cured at 120°C for 6 h in a Thermolyne 30400 muffle furnace (Thermo Scientific, Waltham, MA) to complete the crosslinking reaction. The thickness of the synthesized membrane was measured by a Mitutoyo electronic indicator (Model 543-252B, Mitutoyo America Corp, Aurora, IL) with an accuracy of ±0.5 µm. Photos of the coating solution and the membrane after curing are shown in Figure 2.15.

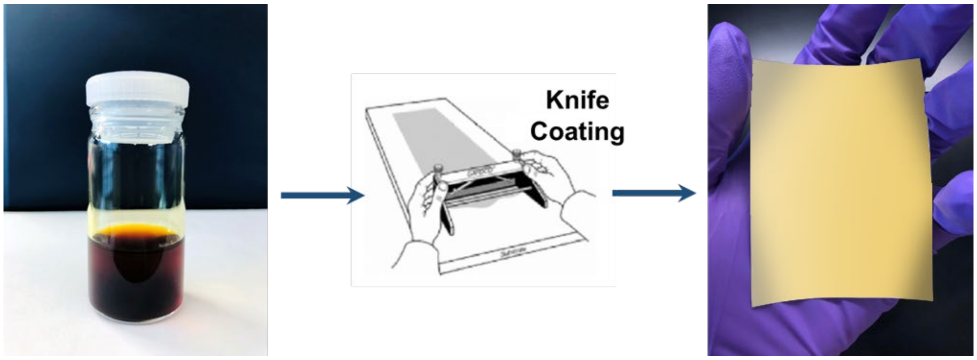

Figure 2.15. Photos of the coating solution and the cured membrane.

The schematic of the facilitated transport mechanism of CO_2 through the amine-containing is shown in Figure 2.16. The amine carriers and the various polar moieties result in a high CO_2 solubility in the membrane. On the contrary, the sorption of H_2 is weak due to the lack of a favorable interaction with the polymers. This discrepancy leads to a considerable CO_2/H_2 solubility selectivity. Moreover, CO_2 can permeate from the high to the low-pressure side either by the intermolecular diffusion of the CO_2–amine reaction product, or the intramolecular diffusion between the reaction product and another free, unreacted amines. This reactive diffusivity is also higher than the Fickian diffusivity of H_2. Therefore, the facilitated transport scheme also features a CO_2/H_2 diffusivity selectivity. The combination of these two selectivities renders a very selective separation of CO_2 from H_2.

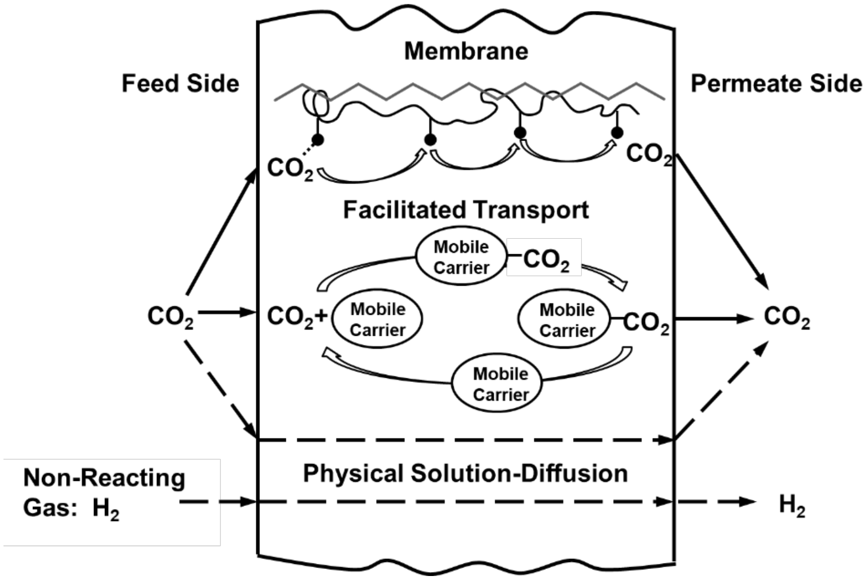

Figure 2.16. Schematic of facilitated transport of CO_2 in a polymeric membrane containing both fixed-site and mobile carriers.

The representative membranes synthesized in BP1 are listed in Table 2.2. Membranes M1–M5 were to study the effect of the reinforcement filler; Membranes M6–M8 were to investigate the different amine structures grafted on the polymer matrix; Membranes M9–M11 were to demonstrate the effect of the functionality of the aminosilane; Membranes M12–M15 were to study the basicity of the aminosilane. Membranes M16–M18 were to show the effect of the severely sterically hindered aminoacid salt on the H_2S/CO_2 separation properties. These results will be discussed in Section 2.1.3.

Table 2.2. Representative membrane compositions and thicknesses.

M#	Crosslinker	Mobile carrier	Filler	Thickness (μm)
1	Dialdehyde	Compounds I	Nanosheet None	25
2	Dialdehyde	Compounds I	Nanosheet Sparse	25
3	Dialdehyde	Compounds I	Nanosheet Low	25
4	Dialdehyde	Compounds I	Nanosheet Medium	25
5	Dialdehyde	Compounds I	Nanosheet High	25
6	1° aminosilane	Compounds II&III	Nanosheet Low	15
7	2° aminosilane	Compounds II&III	Nanosheet Low	15
8	3° aminosilane	Compounds II&III	Nanosheet Low	15
9	AS1 + dialdehyde	Compounds II	Nanosheet Low	15
10	AS2 + dialdehyde	Compounds II	Nanosheet Low	15
11	AS3 + dialdehyde	Compounds II	Nanosheet Low	15
12	AS-Me + dialdehyde	Compounds II	Nanosheet Low	15
13	AS-Et + dialdehyde	Compounds II	Nanosheet Low	15
14	AS-Pr + dialdehyde	Compounds II	Nanosheet Low	15
15	AS-Et + dialdehyde	Compounds II	Nanosheet Medium	15

2.1.3 Task 3 – Membrane Characterization

Summary

- The carbon nanosheets synthesized in house proved to be effective nanofillers to prevent membrane compaction at a feed pressure up to 35 bar.
- Sterically hindered amine carriers and CO_2-philic moieties helped mitigate the carrier saturation phenomenon at high CO_2 partial pressure.

- Bidentate aminosilane AS-Et was shown as an effective crosslinker to improve membrane performance.
- At 35-bar feed pressure, the membrane tailored for the proximity of feed inlet (a CO_2 partial pressure of ~13.8 bar) exhibited a CO_2 permeance of 311 GPU and a CO_2/H_2 selectivity of 125. The membrane tailored for the proximity of retentate outlet (a CO_2 partial pressure of ~1.1 bar) showed a CO_2 permeance of 217 GPU with a CO_2/H_2 selectivity of 268.

Mixed Gas Permeation Measurement

The transport properties of the composite membrane were measured by a Wicke-Kallenbach permeation apparatus as shown in Figure 2.17. Unless other noticed, the membranes were tested at 107°C and 31.7–35 bar feed pressure with a simulated syngas containing 4% water and 6000 ppm H_2S with balance of CO_2 and H_2. The CO_2 and H_2 concentrations were varied to achieve a feed CO_2 partial pressure ranging from 0.5 to 14 bar. These two partial pressures were intended to correspond to the feed CO_2 partial pressures after and before the bulk CO_2 removal, respectively, which will be discussed in detail in Section 2.1.4. The permeate pressure was maintained at 1 psig. After leaving the gas permeation cell, the water vapors in both the retentate and the permeate were trapped in respective water knockout vessels. The dry gas compositions of both gas streams were analyzed using a gas chromatograph (GC) that was equipped with a thermal conductivity detector (Model 6890 N, Agilent Technologies, Palo Alto, CA) and a stainless steel micropacked column (80/100 mesh Carboxen 1004, Sigma-Aldrich, St. Louis, MO). The H_2S concentration was measured by a sulfur chemiluminescence detector (Agilent 8355 SCD) in tandem with the GC. The membrane separation performance is characterized by CO_2 permeance and ideal CO_2/H_2 selectivity. The CO_2 permeance is the CO_2 flux normalized by its partial pressure differential across the membrane. It is reported in the unit, Gas Permeation Unit (GPU); 1 GPU = 10^{-6} $cm^3(STP)\ cm^{-2}\ s^{-1}\ cmHg^{-1}$ [1]. Similarly, the H_2 permeance can also be measured. The ideal CO_2/H_2 selectivity is defined as the ratio of the gas permeances.

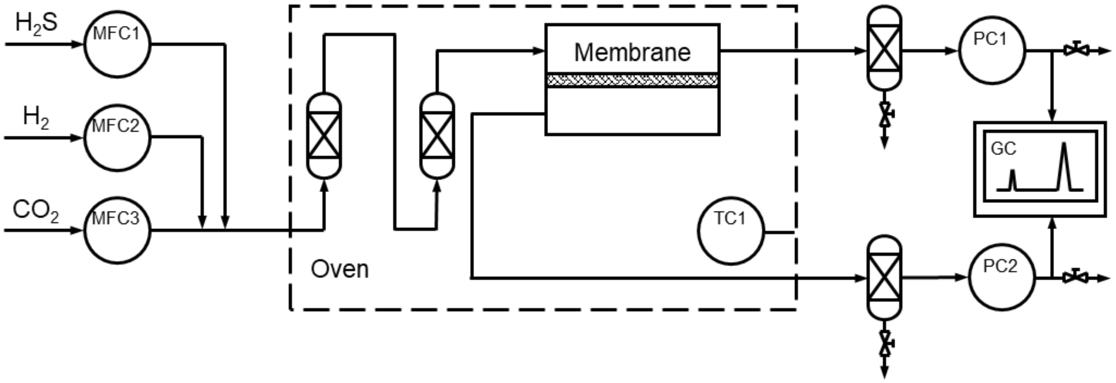

Figure 2.17. Schematic of mixed gas permeation test unit. MFC = mass flow controller; TC = temperature control; PC = pressure control; GC = gas chromatograph.

Reinforcement Effect of Nanofiller

Membranes M1–M3 and M5 in Table 2.2, which contained none, sparse, low, and high loadings of the nanofiller, were tested with a feed pressure of 31.7 bar and a CO_2 partial pressure of 1 bar. The gas transport results are shown in Figure 2.18. A low CO_2 permeance of 91 GPU was measured due to the severe membrane compaction in the absence of the nanofiller. The low permeance was attributed to the compaction of the selective layer upon high hydraulic pressure, thereby the densification of the polymer matrix.

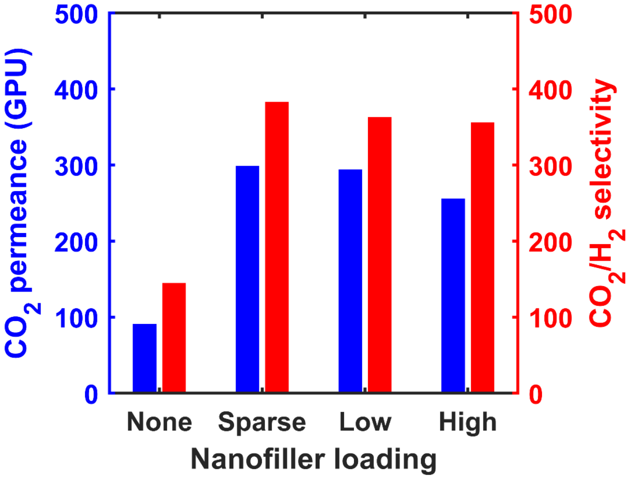

Figure 2.18. Effects of nanofiller loading on CO_2 permeance (blue) and CO_2/H_2 selectivity (red) at a feed pressure of 31.7 bar and a CO_2 partial pressure of 1 bar.

With an increasing nanofiller loading, the CO_2 permeance increased significantly. At a sparse loading, the CO_2 permeance increased to 299 GPU with a CO_2/H_2 selectivity of 383. Further increasing the nanofiller loading resulted in a similar permeance of 294 GPU and a lower selectivity of 363. However, the permeance and selectivity reduced to 256 GPU and 356, respectively, at a high nanofiller loading. The above trends indicated that the dispersion of nanosheet enhanced the rigidity of the selective layer and offset the membrane compaction, but a high loading of nanosheet actually served as a gas barrier. Due to the high aspect ratio of the nanosheet, a shear-induced alignment is very plausible during the coating of the selective layer [21]. In this case, the nanosheets likely align perpendicular to the thickness direction of a polymeric membrane. The presence of nanosheets perturbs the diffusion of the penetrants and results in certain tortuosity of the diffusion path. When the loading is low, the added mass transfer resistance is small. As the loading increases, a more torturous diffusion pathway is required for the penetrant to diffuse across the array of barriers formed by the nanosheets.

The mechanical properties of Membranes M1–M3 were measured by nanoindentation (MTS Nanoindenter® XP). The device was equipped with a Berkovich indenter, the indentation by which was modeled as a paraboloid punch. The load-displacement profiles are shown in Figure 2.19 (a). Each profile consists of three phases: 1) loading, 2) dwelling, and 3) unloading. Each sample was also reloaded, where the unloading and reloading curves were nearly identical (results not shown here). Therefore, the unloading behavior was purely elastic, and the Oliver–Pharr method was used to determine the reduced Young's moduli (E_r) [22]. The corresponding results are shown in Figure 2.19 (b). The error bars were generated by the residuals of the model fitting.

As seen, the membrane containing no nanofiller showed a low E_r of 0.094 GPa. Its low rigidity was also exemplified by the small hysteresis between the loading and unloading curves of this sample. The low modulus coincided well with the observed membrane compaction. For the untested membrane, a distinctive, dense polymeric selective layer of 25-µm thickness was supported by the porous support. After the high-pressure exposure, however, the thickness was measured again by the digital indicator and a reduced selective layer thickness of 12 µm was determined, indicating a severely densified polymer matrix.

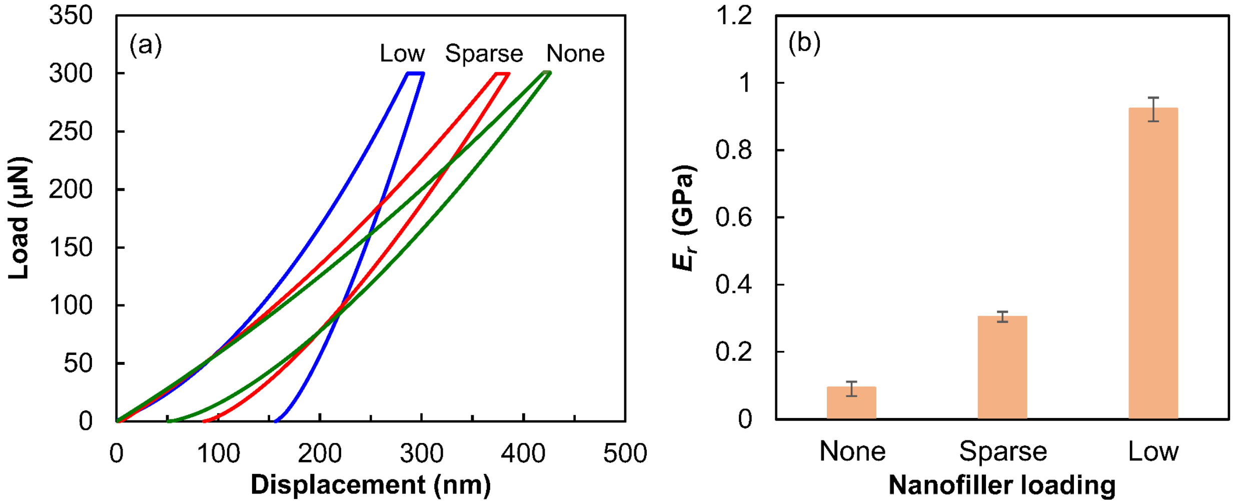

Figure 2.19. (a) Load-displacement relationships and (b) reduced Young's moduli (E_r) for Membranes M1–M3.

With an increasing nanosheet loading, the reduced Young's modulus increased significantly. At the sparse nanosheet loading, an E_r of 0.305 GPa was obtained, and a further increase in the nanosheet loading resulted in an even high E_r of 0.923 GPa. Microstructurally, the nanosheets likely formed an aligned array, where the basal planes were perpendicular to the membrane's thickness direction [21]. The aligned nanosheets restricted the motion of the polymer chains, leading to higher resistance to deformation. This set of data substantiate the reinforcement effect of the nanofiller.

Loading Optimization for 35-bar Feed Pressure

Membranes M3 and M4 in Table 2.2, which contained low to medium loadings of the reinforcement filler, were tested with feed pressure of 25, 31.7 and 35 bar and a constant CO_2 partial pressure of 1 bar. The purpose was to study if the nanofiller loading was sufficient for the feed pressure of 35 bar. The gas transport results are shown in Figure 2.20. As seen, Membrane M3 exhibited very similar results at 25 and 31.7 bar feed pressures, which were ca. 300 GPU CO_2 permeance and 350 CO_2/H_2 selectivity. Therefore, the moderate loading of the reinforcement filler was effective to suppress the membrane compaction with a feed pressure up to 31.7 bar. When the feed pressure was increased to 35 bar, however, the CO_2 permeance reduced to 261 GPU, along with a reduced CO_2/H_2 selectivity of 312. Since the CO_2 partial pressure was maintained, any effect of carrier saturation was ruled out, and the reduced performance was attributed to the membrane compaction caused by the higher hydraulic pressure.

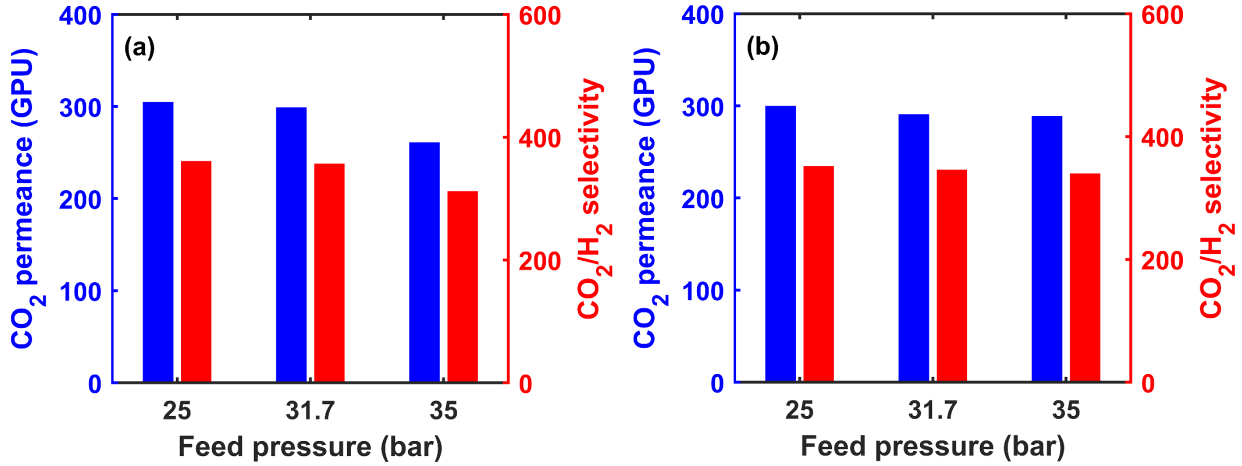

Figure 2.20. Effects of feed pressure on CO_2 permeance (blue) and CO_2/H_2 selectivity (red) for Membranes (a) M3 and (b) M4 at a CO_2 partial pressure of 1 bar (retentate outlet).

On the contrary, the higher nanofiller loading of Membrane M4 bestowed it a better mechanical stability. As seen in Figure 2.20 (b), the membrane exhibited overall a CO_2 permeance greater than 289 GPU and a CO_2/H_2 selectivity higher than 340 across the studied pressure range. Especially, the improved selectivity made this membrane more promising to be used in the membrane process for a high degree of H_2 recovery.

A similar trend was observed for Membranes M13 and M15 as seen in Figure 2.21 (a) and (b), respectively. For Membrane M13 with a low nanofiller loading, a feed pressure of 35 bar reduced the CO_2 permeance from 327 to 291 GPU, accompanied by a sharp reduction in the selectivity from 139 to 107. By increasing the nanofiller loading, Membrane M15 demonstrated a higher CO_2 permeance of 315 GPU and an improved selectivity of 130 at 35-bar feed pressure. Overall, the higher loading of nanofiller successfully improved the mechanical robustness of the membranes, resulting in a more selective performance at the 35-bar feed pressure.

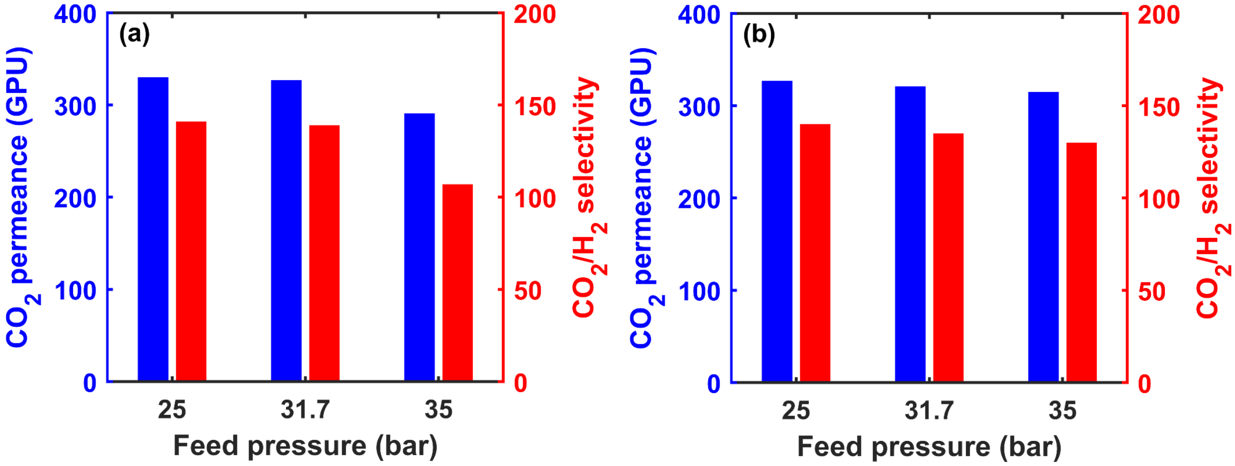

Figure 2.21. Effects of feed pressure on CO_2 permeance (blue) and CO_2/H_2 selectivity (red) for Membranes (a) M13 and (b) M15 at a CO_2 partial pressure of 12.5 bar (feed inlet).

Enhanced Chemisorption of CO_2 via Aminosilanes

The effect of aminosilane on the chemisorption of CO_2 is exemplified by Membranes M6–M8 in Table 2.2. Their CO_2/H_2 separation performances were tested at a CO_2 partial pressure of 12.5 bar, and the results are shown in Figure 2.22. As seen, the membrane crosslinked by 1° aminosilane (M6) showed a CO_2 permeance of 256 GPU but a low CO_2/H_2 selectivity of 84. By using 2° aminosilane as the crosslinker, Membrane M7 showed an improved permeance of 264 GPU as well as a higher selectivity of 87. The increased CO_2 permeance was attributed to the higher amine loading introduced by the diamine. However, the highest permeance was achieved by 3° aminosilane (M8), where the 3° monoamine led to a 269 GPU CO_2 permeance and an 89 CO_2/H_2 selectivity. In this case, the 3° amine does not react with CO_2 directly, but generates hydroxide ion to fixate CO_2 as HCO_3^- [23]. Stoichiometrically, one mole of 3° amine reacts with one mole of CO_2. Although this reaction is known to be slow, a higher CO_2 uptake is generally more important than the sorption kinetics when the feed CO_2 partial pressure is high. Therefore, the membrane crosslinked by 3° aminosilane showed the highest CO_2 permeance. Based on this set of data, the 3° aminosilane was chosen for the following membrane synthesis.

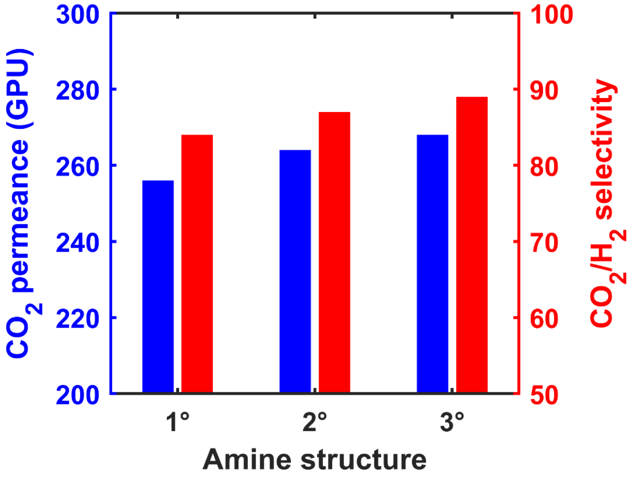

Figure 2.22. Effect of the amine structure on aminosilane on CO_2 permeance (blue) and CO_2/H_2 selectivity (red) at a feed pressure of 31.7 bar and a CO_2 partial pressure of 12.5 bar.

Effect of Functionality of Aminosilane

The aminosilanes used in Membranes M9–M11 were varied from monodentate to tridentate to study their effects. The transport properties of these membranes were measured at a feed pressure of 31.7 bar and a CO_2 partial pressure of 12.5 bar. The gas transport results are shown in Figure 2.23. As seen, by increasing the crosslinking site per molecule of the aminosilane, the CO_2 permeance reduced from 391 to 314, then to 246 GPU. The reduced CO_2 permeance was attributed to the increased crosslinking degree as discussed in Figure 2.4. A highly crosslinked polymer network was less prone to swelling in the presence of water vapor, thereby a reduced free volume for gas permeation. On the other hand, the CO_2/H_2 selectivity increased from 66 to 138, then reduced to 105. The low crosslinking degree could explain the low CO_2/H_2 selectivity of Membrane M9 (crosslinked by AS-1), where the swollen polymer network could not hamper the H_2 permeation effectively. The low selectivity of Membrane M11 (AS-3 as crosslinker), however, was mainly a consequence of the self-condensation of AS-3. The resultant formation of siloxane induced certain heterogeneity in the membrane, which could serve as defect sites for H_2 permeation. This set of experiments suggested that the bidentate aminosilane was the best crosslinker for membrane synthesis.

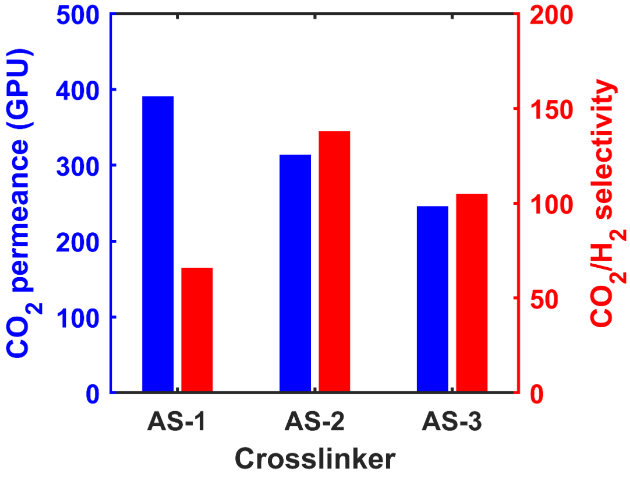

Figure 2.23. Effects of aminosilane functionality on CO_2 permeance (blue) and CO_2/H_2 selectivity (red) at a feed pressure of 31.7 bar and a CO_2 partial pressure of 12.5 bar.

Effect of Basicity of 3° Aminosilane

The levels of basicity of the aminosilanes used in Membranes M12–M14 were increased to study their effects on the CO_2 transport. As a comparison, a membrane crosslinked by the dialdehyde but not aminosilane was also studied here for comparison. The transport properties of these membranes were measured at a feed pressure of 31.7 bar and a CO_2 partial pressure of 12.5 bar. The gas transport results are shown in Figure 2.24. As seen, the membrane without aminosilane showed a low CO_2 permeance of 251 GPU and a CO_2/H_2 selectivity of 67. As discussed in Figure 2.4, the crosslinking degree of this membrane was only ca. 24%. The loosely conformed polymer matrix could not sufficiently refrain the permeation of H_2, thus the low selectivity. The low CO_2 permeance, however, was inconsistent with the loose polymer matrix. It was suspected that the chain packing of the polyalcohol was not sufficiently restricted because of the lack of acetal and siloxane linkages in this membrane. Therefore, there might be semi-crystalline regions that deterred the CO_2 permeation.

By using AS-Me as the crosslinker (Membrane M12), the CO_2 permeance increased to 314 GPU, along with a better CO_2/H_2 selectivity of 138. The incorporation of the 3° amino groups enhanced the chemisorption of CO_2, thereby the higher permeance. In addition, the higher crosslinking degree was less prone to swelling in the presence of water vapor, thereby a tighter polymer network to reduce the H_2 permeation. When the aminosilane was changed to AS-Et (Membrane M13) and AS-Pr (Membrane M14), the CO_2 permeance further increased to 327 GPU then to 331 GPU. This was in line with the increased basicity of the aminosilanes, which generated more hydroxide ions readily available for the reaction with CO_2. On the other hand, the CO_2/H_2 selectivity reduced upon the change of the aminosilane, mainly because of the inching up H_2 permeance. Likely, the bulkier ethyl and isopropyl substituents slightly increased the free volume of the membrane. Overall, AS-Et, in combination with the dialdehyde, was proven to be the best crosslinker.

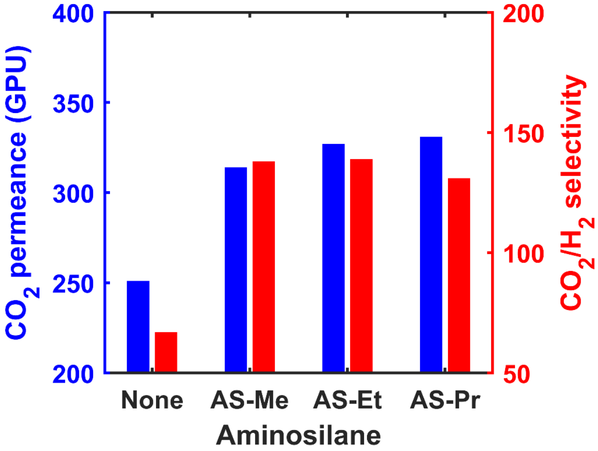

Figure 2.24. Effects of the basicity of aminosilane on CO_2 permeance (blue) and CO_2/H_2 selectivity (red) at a feed pressure of 31.7 bar and a CO_2 partial pressure of 12.5 bar.

Membrane Performances at Different CO_2 Partial Pressures

This section investigates the gas transport of membranes containing different carriers and their responses to different feed CO_2 partial pressures. The two best candidates, Membranes M4 and M15, were tested. Figure 2.25 shows the CO_2 permeances and CO_2/H_2 selectivities for these membranes with a simulated syngas at 107°C. For data with a CO_2 partial pressure less than 12.5 bar, the feed pressure was 31.7 bar; for a higher CO_2 partial pressure, the feed pressure was increased to 35 bar. The simulated syngas comprised 4% water vapor and 6000 ppm H_2S with balance of CO_2 and H_2. The CO_2 and H_2 concentrations were varied gradually to reduce the feed side CO_2 partial pressure from 13.8 to 0.5 bar, which corresponded to the feed CO_2 partial pressures before and after the bulk CO_2 removal, respectively.

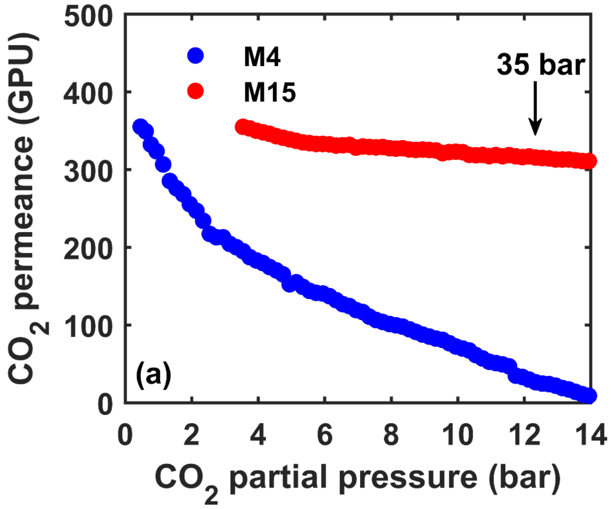

Figure 2.25. Effects of feed CO_2 partial pressure on (a) CO_2 permeance and (b) CO_2/H_2 selectivity.

As seen in Figure 2.25 (a), Membrane M4 showed the highest CO_2 permeance of 351 GPU at 0.5 bar of feed CO_2 partial pressure, and the CO_2 permeance reduced considerably with increasing CO_2 partial pressure to 12.5 bar due to the carrier saturation phenomenon, in which the lower performance was caused by less free amine carriers available in the membrane due to higher CO_2 partial pressure. H_2, on the other hand, permeated through the membrane via the solution-diffusion mechanism, and its permeance remained as constant at 0.77 GPU. Consequently, the CO_2/H_2 selectivity also reduced from 439 to 83 (see Figure 2.25 (b)).

Different from the previous trends, the feed CO_2 partial pressure had a very weak effect on the separation performance of Membrane M15. The presence of amino groups and the abundant CO_2-philic moieties possessed by Compound II enhanced the CO_2 solubility in the membrane at high CO_2 partial pressure. Consequently, a CO_2 permeance of 321–361 GPU and a very good CO_2/H_2 selectivity of 123–135 were obtained for a CO_2 partial pressure of 3.5–12.5 bar.

The different degrees of dependence on the feed CO_2 partial pressure of these membranes provide a design opportunity for a single-stage membrane process. The more permeable but less selective Membrane M15 can be implemented to the proximity of feed inlet, where the CO_2 partial pressure is high but the H_2 partial pressure is low. Upon CO_2 removal, the feed CO_2 partial pressure sharply reduces whereas the H_2 transmembrane driving force increases. In this case, Membrane M4 can be used to elevate the CO_2 permeance and CO_2/H_2 selectivity.

After changing the feed pressure to 35 bar, neither the CO_2 permeance nor the CO_2/H_2 selectivity exhibited a sharp reduction. It was in line with the good mechanical robustness of the membranes containing an optimized loading of nanofiller. Overall, the membrane (M15) tailored for the proximity of feed inlet (13.8 bar CO_2 partial pressure) exhibited a CO_2 permeance of 311

GPU and a CO_2/H_2 selectivity of 125. The membrane (M4) tailored for the proximity of retentate outlet (2.2 bar CO_2 partial pressure) showed a CO_2 permeance of 217 GPU with a CO_2/H_2 selectivity of 268.

Simultaneous H_2S and CO_2 Removal from Syngas

Figure 2.26 shows the H_2S/CO_2 selectivities of Membranes M4 and M15 at different feed CO_2 partial pressures but a constant H_2S concentration of 6000 ppm. For a H_2S/CO_2 selectivity higher than unity, the membrane is capable of removing CO_2 and H_2S simultaneously from the syngas, which results in a low-sulfur hydrogen for combustion or chemical synthesis. As seen, H_2S was generally more permeable than CO_2 through the two membranes. In addition, the CO_2 partial pressure barely affected the H_2S permeation by comparing Figure 2.26 and Figure 2.27. H_2S permeances of 980 and 810 GPU were obtained for Membranes M4 and M15, respectively; the higher H_2S permeance of Membrane M4 was attributed to its higher amine content. Overall, this led to a H_2S/CO_2 selectivity in the range of 3–7 for these membranes at 31.7 bar.

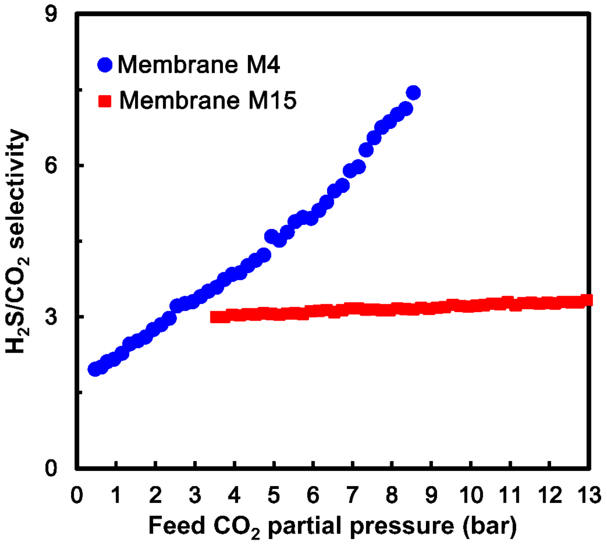

Figure 2.28. H_2S/CO_2 selectivities at different feed CO_2 partial pressures.

2.1.4 Task 4 – Preliminary Techno-Economic Analysis Performance

Summary

- A single-stage membrane process was designed to achieve 90% CO_2 removal with 95% purity.
- A cost of electricity increase of 15.30% and a H_2 recovery of 99.4% can be realized by the current membranes at 31.7-bar feed pressure.
- Increasing the feed pressure to 35 bar resulted in an improved H_2 recovery of 99.5% with the optimized membranes synthesized.

Description of Improved Process

The location of the membrane process in an integrated gasification combined cycle (IGCC) is shown in Figure 2.27. A detailed process flow diagram of the single-stage membrane process is shown in Figure 2.28. In the techno-economic analysis, Cases B5A and B5B in the U.S. Department of Energy (DOE) 2015 Cost and Performance Baseline [24] were followed for the IGCC with General Electric Energy (GEE) "radiant-only" gasifier. The high pressure shifted syngas (54.1 bar) from the low temperature water-gas-shift reactor is expanded to about 18–35 bar by a turboexpander EX-01. The thermal expansion cools the gas stream for mercury removal by an activated, sulfur-impregnated carbon adsorption bed.

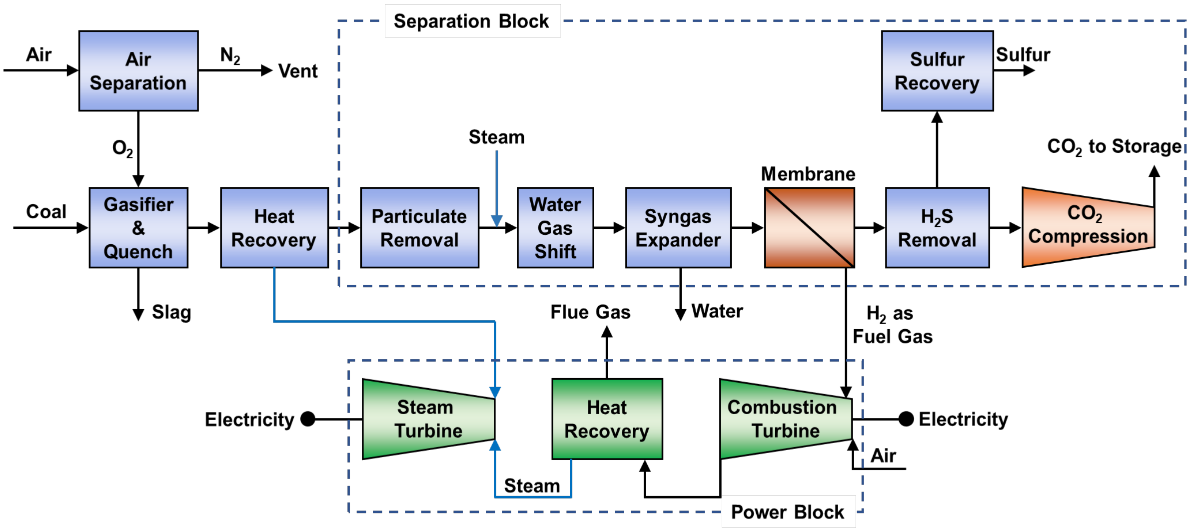

Figure 2.29. Location of the proposed membrane technology in an IGCC plant with Selexol for H_2S removal.

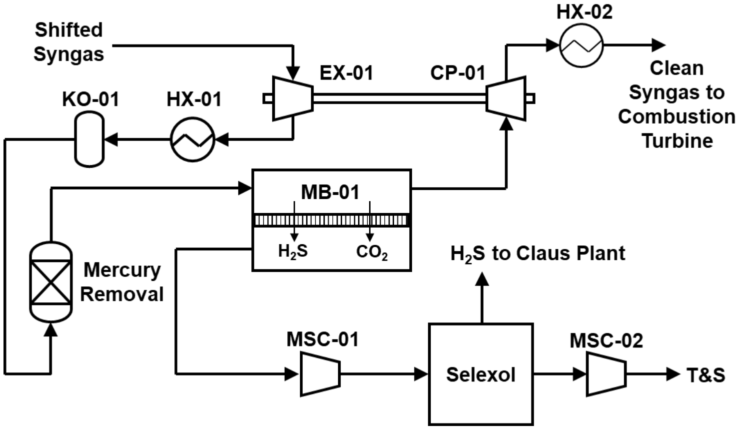

Figure 2.30. Flowsheet of membrane process for integration in IGCC with Selexol for H_2S removal.

For certain pressure range, a heat exchanger HX-01 and a water knockout drum KO-01 are used to adjust the syngas temperature to about 110°C. Then, the gas stream enters the first membrane stage MB-01 with a CO_2/H_2 selectivity >100, which separates the feed to a CO_2-depleted retentate with 90% CO_2 removal and >99% H_2 recovery, and a CO_2-rich permeate with >95% CO_2 purity on dry basis. Due to an even higher H_2S/H_2 selectivity (>300), H_2S also permeates to the downstream preferentially, resulting in <30 ppm H_2S in the retentate. It should be noted that the drastically reducing CO_2 partial pressure from the feed to the retentate typically leads to an increasing CO_2/H_2 selectivity, e.g., >300, for the facilitated transport membrane. This feature is beneficial for achieving the high H_2 recovery.

The retentate is recompressed to 31.7 bar by a coaxial compressor CP-01 driven by the turboexpander EX-01, if the discharge pressure of EX-01 is below 31.7 bar. This step is energy efficient since the CO_2 removal reduces the gas flow rate, thus a less energy consumption of the compressor. The remaining power generated by EX-01 is used for electricity generation. After recompression, the cleaned syngas rises to 196°C and is sent to the gas turbine combustor for power generation. A heat exchanger HX-02 is optional for temperature adjustment. The permeate stream is operated at 1.1 bar to maximize the transmembrane driving force without incurring extra parasitic energy.

As shown in Figure 2.28, the permeate stream is compressed to 50 bar by a 5-stage front-loaded centrifugal compressor MSC-01 and sent to a single-stage Selexol unit for H_2S removal. The recovered H_2S is further converted to elemental sulfur by a Claus plant. The H_2S-stripped CO_2 stream is eventually compressed to 153 bar by a 3-stage front-loaded centrifugal compressor MSC-02 for sequestration or enhanced oil recovery.

Process Modeling and Costing Method

Cases B5A and B5B in the baseline document [24] were followed for the process modeling. The GEE “radiant-only” gasifier was considered here since it renders the lowest cost of electricity (COE) with carbon capture. All calculations were based on a 550 MW net power IGCC plant. The gas permeation through the membrane module was assumed to be countercurrent. The equipment metric of each equipment was calculated to achieve 90% CO_2 removal and >95% CO_2 purity, along with >99% H_2 recovery. All costs were reported in 2011 dollars.

Assumptions of membrane related costs are listed as follows:

1) The membrane element cost used was \$5/ft^2 membrane area based on the current market price for spiral-wound element in natural gas sweetening [25]. A price of \$0.5/ft^2 membrane area was used for the module housing according to reverse osmosis applications with a feed pressure up to 60 bar [26].

2) An installation labor factor of 0.2 is assigned to the membrane modules. The installation material cost of the membrane skid with its associated labor cost is estimated as \$8/m^2 membrane area based on commercial-scale reverse osmosis plants [26].

3) In the calculation of the variable cost, the membrane life was assumed as 4 years, and the membrane replacement cost was \$5/ft^2. Therefore, the annual membrane replacement cost was \$1.25/ft^2.

4) 15% project contingency and 20% process contingency were assigned to the membrane process.

COE increase was selected as the cost metric for this analysis. It was defined as the percentage increase of the COE of the membrane process relative to the COE of the benchmark IGCC without carbon capture (Case B5A) [24].

Effect of Carrier Saturation Phenomenon on Separation Performance

Figure 2.29 shows the change of CO_2 partial pressure on the feed side of the membrane module upon CO_2 removal. A feed pressure of 31.7 bar and a permeate pressure of 1.1 bar were used to calculate the membrane area required for 90% CO_2 removal from the shifted gas. The horizontal axis in Figure 2.29 is the distance from the feed inlet normalized by the total length of the feed flow path (ca. 14 m for 550 MW). As seen, the CO_2 partial pressure reduced significantly due to the CO_2 removal, by which more carriers in membrane could be available to facilitate the permeation of CO_2. To utilize this feature, the more permeable but less selective Membrane M15 was used in the proximity of the feed inlet, i.e., the first 35% of the membrane stage, whereas the more selective amine-containing Membrane M4 was used in the proximity of the retentate outlet, i.e., the remaining 65% of the membrane stage. This could be achieved by connecting the central tubes of spiral-wound modules made from different membranes, from an engineering point of view. As seen, the CO_2 permeance increased from about 299 GPU to 314 GPU from the feed inlet to the retentate outlet, based on the membrane performance obtained using the simulated syngas in Figure 2.25. Since H_2 only permeated through the membrane by the solution-diffusion mechanism, its permeance was about 2.15 GPU for Membrane M15 and 0.78 for Membrane M4, which was not affected by the CO_2 partial pressure. Consequently, the CO_2/H_2 selectivity also increased from about 139 to 313 from the feed to the retentate. The drastically increased CO_2 permeance led to a 31% reduction of the required membrane area compared to the one with constant permeance corresponding to the feed inlet. More importantly, the H_2 partial pressure increased significantly upon the CO_2 removal. The tripled CO_2/H_2 selectivity approaching to the retentate outlet minimized the H_2 loss, and a H_2 recovery >99% could be achieved by a single-stage membrane process.

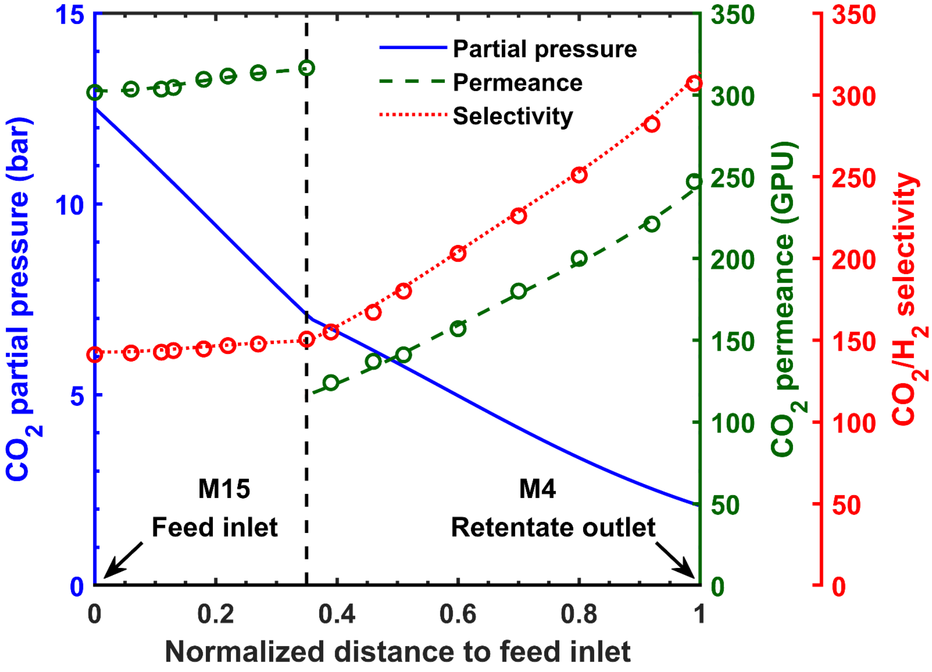

Figure 2.31. Change of CO_2 partial pressure on the feed side of membrane module. Markers are the data shown in Figure 2.25.

Effect of CO_2 Permeance

Figure 2.30 shows the effects of CO_2 permeance on the membrane area and COE increase for a feed pressure of 31.7 bar, a permeate pressure of 1.1 bar, and a CO_2/H_2 selectivity of 200. A constant CO_2 permeance was assumed for each data point, that is, the carrier saturation phenomenon is not considered. As shown, the membrane area reduced with increasing CO_2 permeance, thereby a reducing COE increase. For instance, increasing the CO_2 permeance from 50 to 200 GPU led to a decreasing membrane footprint from 2.96×10^5 to 7.41×10^4 m^2, which translated to a COE increase from 18.2 to 15.5%. Further increasing the CO_2 permeance was beneficial for reducing the system footprint, but the effect on COE increase was less significant. This was because at a higher CO_2 permeance, the membrane only contributed to less than 20% of the bare erected cost for the capture system. The dashed lines in Figure 2.30 represent the COE increases achieved in the first three quarters of BP1, during which the synthesized membrane exhibited the most significant improvement on the CO_2 permeance. As shown, by improving the CO_2 permeance near the feed inlet, the COE increase was reduced from 15.70 to 15.30% during the first three quarters of BP1. These results also suggest that the permeance of the current membrane is high enough and is not the limiting factor for the process economics. Instead, non-membrane cost components, e.g., the Selexol unit for H_2S removal, should be optimized.

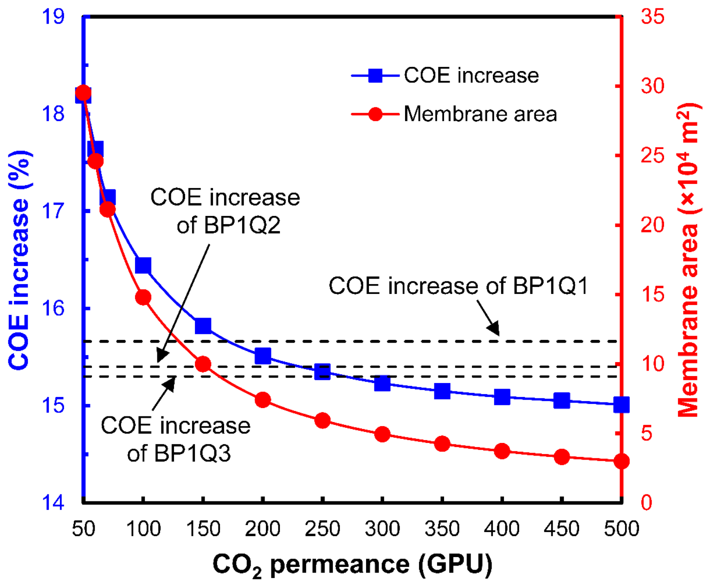

Figure 2.32. Effect of CO_2 permeance on COE increase.

Effect of H_2S/CO_2 Selectivity

Figure 2.31 shows the effect of H_2S/CO_2 selectivity on the H_2S concentration in the sweet syngas, which will be fed to the combustion turbine. A feed pressure of 31.7 bar and a permeate pressure of 1.1 bar were used for the calculation. A constant H_2S/CO_2 selectivity was assumed. As shown, a H_2S/CO_2 selectivity of 3.1 was enough to reduce the H_2S to 30 ppmv in the syngas product, which meets the stack gas emission target for an IGCC plant [24]. A H_2S concentration less than 10 ppm could be achieved by a selectivity of 4, which is beneficial for the fouling prevention of the heat recovery steam generator's cold end tubes. A higher H_2S/CO_2 selectivity could further reduce the H_2S to less than 1 ppm. The low sulfur syngas could be used for fuels production and chemical synthesis. The dashed line in Figure 2.31 shows that the current combination of Membranes M4 and M15 can reduce the H_2S concentration to 5.6 ppmv, due to a H_2S/CO_2 selectivity in the range of 3–7 for these membranes when operated at 31.7 bar.

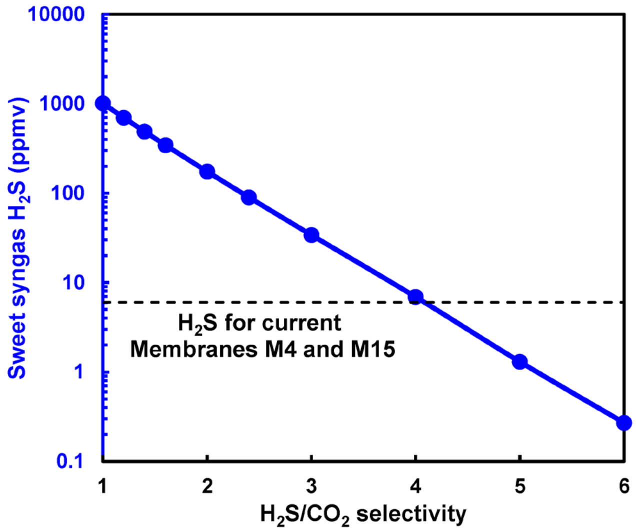

Figure 2.33. Effect of H_2S/CO_2 selectivity on H_2S concentration in retentate.

Effect of Feed Pressure

The possibility of operating the developed membranes at a feed pressure >31.7 bar was studied with two conceptual membrane modules:

1) 35% Membrane M13 and 65% Membrane M3, both with a low loading of the reinforcement filler.
2) 35% Membrane M15 and 65% Membrane M4, both with a medium loading of the reinforcement filler.

The CO_2 and H_2 permeances were determined by the local CO_2 partial pressure in accordance with the experimental data. The permeate pressure was kept at 1.1 bar. All calculations were conducted for 90% CO_2 removal. As seen in Figure 2.32, for the first case, the increasing feed pressure initially increased the H_2 recovery, but it led to a reduced recovery if the feed pressure was higher than 32 bar. Initially, the elevated feed pressure enhanced the feed-to-permeate pressure ratio, which rendered the faster removal of CO_2 and a reduced H_2 loss to the permeate side. In this region, the H_2 recovery was limited by the transmembrane driving force. At a feed pressure higher than 32 bar, however, Membranes M3 and M13 exhibited low CO_2/H_2 selectivities due to the insufficient loading of nanofiller. In this case, the H_2 recovery was limited by the membrane selectivity.

However, with the optimized Membranes M4 and M15, the CO_2/H_2 selectivities were significantly improved, which reduced the H_2 loss especially at the high feed pressure range. Therefore, the highest H_2 recovery of 99.4% was achieved at 35 bar.

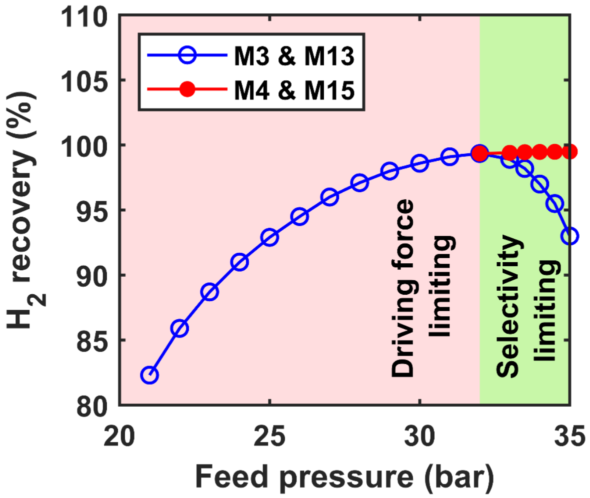

Figure 2.34. Effect of feed pressure on H_2 recovery.

2.1.5 Task 5 – Optimized Membrane Synthesis

Summary

- The thermogravimetric analyses of the composite membranes tailored for the feed inlet and retentate outlet was carried out, which indicated an excellent stability at the operating temperature.
- A high-capacity tangential filtration setup was used to speed up the purification involved in the perforation step for the reinforcement nanofiller.
- Aminoacid salts with severe steric hindrance were synthesized to investigate the feasibility of effective H_2S/CO_2 separation by membrane.

Thermal and Mechanical Stabilities of Composite Membranes

In view of the good gas separation performances of Membranes M4 and M15, their thermal and mechanical stabilities were thoroughly characterized, including the individual components used for membrane synthesis. The thermal stability of the polymer network was evaluated by a PerkinElmer (Waltham, MA) Pyris 1 TGA instrument from 20 to 600°C at a heating rate of 10°C/min under a nitrogen atmosphere (flow rate of 30 ml/min). As shown in Figure 2.33 (a), the polymer network decomposed in two steps with temperature ranges of 300–370°C for the acetal linkage ($R_2C(OR')_2$), and 410–500°C for the –C–O–Si– linkage.

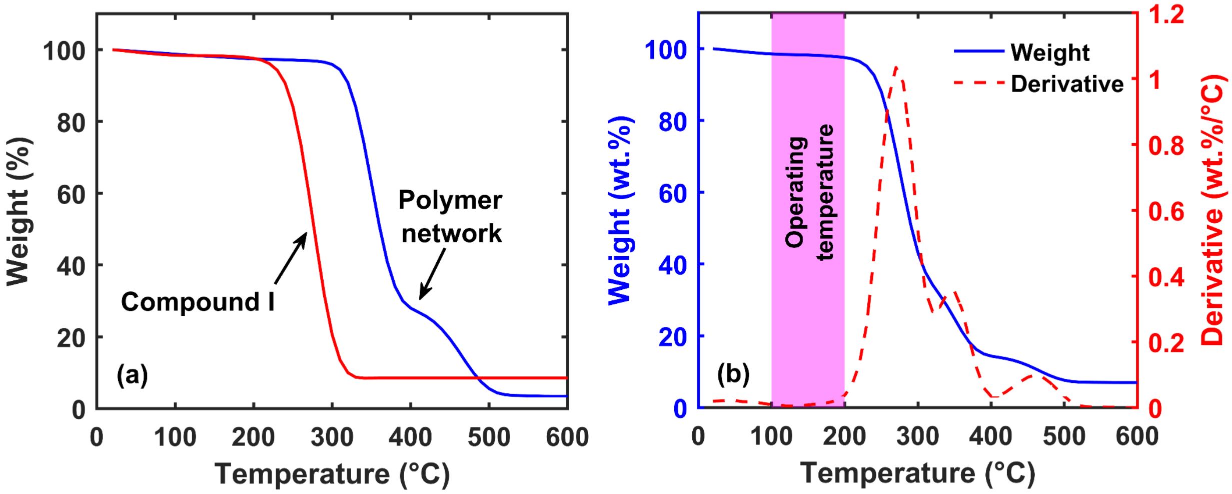

Figure 2.35. (a) TGA curves of polymer network and carrier Compound I; (b) TGA curve of a blend of the polymer network and Compound I.

The effect of mobile carrier on the thermal stability of the polymer network was also studied. The first mobile carrier evaluated herein was Compound I, an aminoacid salt tailored for the retentate outlet. The TGA curve of Compound I is shown in Figure 2.33 (a), which exhibited a single-step decomposition at 250–300°C. This carrier was then blended with the polymer network based on the membrane composition tailored for the retentate outlet. Figure 2.33 (b) shows the TGA curve of this polymer blend. As seen, the blend primarily decomposed at 270, 350, and 460°C, which were consistent with the decomposition temperatures of the polymer network and Compound I. Little weight loss was observed in the temperature range of 100–200°C, which indicated an excellent thermal stability at the operating temperature of 107°C.

The mobile carrier Compound II tailored for the feed inlet was also investigated by the TGA method, and the result is shown in Figure 2.34 (a). As seen, this compound showed a single-step decomposition at ca. 210°C, which was lower than that of Compound I due to the absence of strong Coulombic interactions. After blending Compound II with the polymer network, the composite still exhibited the characteristic decomposition temperature at ca. 200–220°C as shown in Figure 2.34 (b), which corresponded to the loss of Compound II. However, this primary decomposition temperature was higher than the operating temperature at 107°C. Therefore, the composite should be thermally stable under the operating conditions.

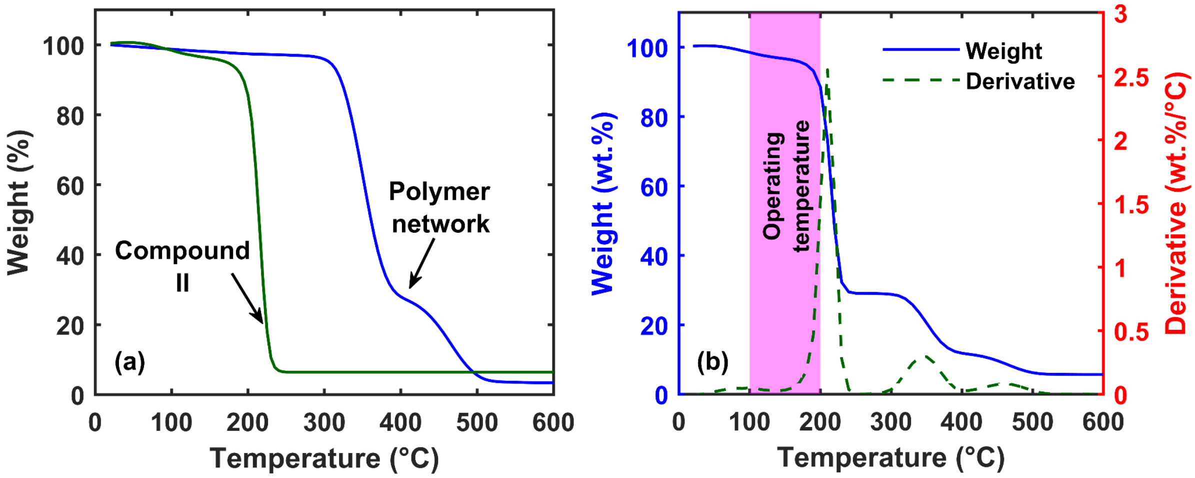

Figure 2.36. (a) TGA curves of polymer network and carrier Compound II; (b) TGA curve of a blend of the polymer network and Compound II.

The thermal stabilities of the polymer blends were further analyzed in the presence of the reinforcement nanofiller. As shown in Figure 2.35 (a) for TGA curves of selective layer materials tailored for the retentate outlet, the perforated nanofiller itself exhibited an appreciable amount of weight loss between 100–200°C due to the decomposition of an oxygen-containing functional group. After incorporated into the polymer composite, however, the nanofiller did not cause an observable weight loss of the composite. As depicted in Figure 2.35 (b) for TGA curves of selective layer materials tailored for the feed inlet, similar results were obtained. It is presumed that the labile oxygen-containing functional groups on the nanofiller has largely reacted with the amino groups in Compounds I and II. In addition, the polar acetal group in the polymer network can form hydrogen bonds with a number of surface functional groups of the nanofiller, which also improve the thermal stability of nanofiller. Overall, the synthesized polymer network proved to be a thermally stable host for the mobile carrier and reinforcement nanofiller. In addition, the mobile carriers exhibited essentially no volatility at 107°C. Therefore, the selective layer materials can potentially be thermally stable for long-term operation.

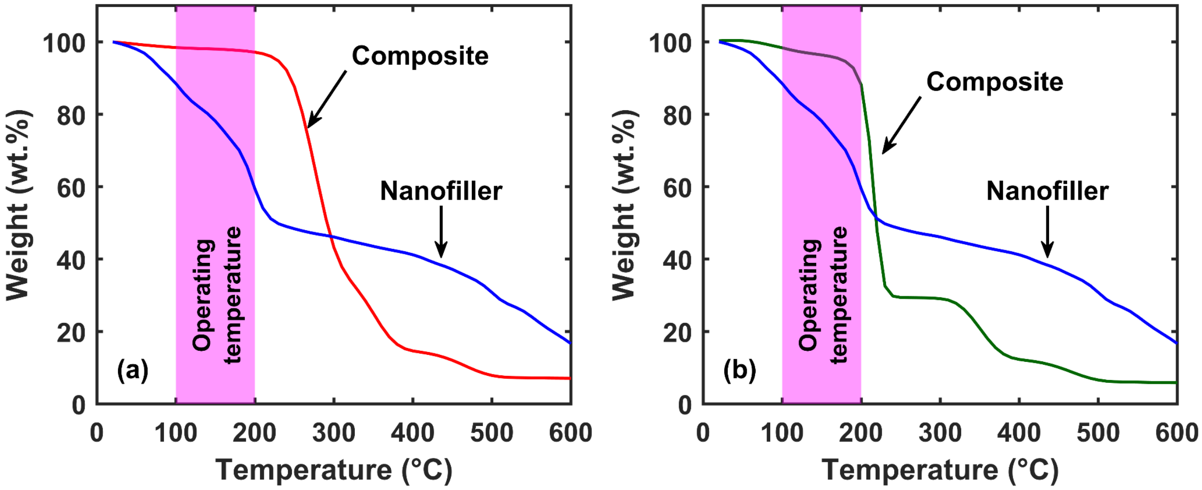

Figure 2.37. TGA curves of selective layer materials tailored for the (a) retentate outlet and (b) feed inlet containing perforated carbon sheets as reinforcement fillers.

In order to fabricate the polymer composites into thin-film composite membranes, the selective layer materials need to be coated on a mechanically robust, nanoporous polymer support. The support consists of a nanoporous polysulfone (PSf) layer and a polyethylene terephthalate (PET) non-woven fabric. Their thermal stabilities were also investigated via the TGA method, and the results are shown in Figure 2.36. As shown in Figure 2.36 (a), the PSf layer only exhibited about 10% weight loss at ca. 590°C, which was considerably higher than the operating temperature. For the PET non-woven fabric as seen in Figure 2.36 (b), it showed a primary decomposition temperature at 445°C, followed by a secondary decomposition at 560°C. Overall, the polymer support possessed an even better thermal stability than the selective layer materials. All layers in the thin-film composite membranes should be thermally stable in the designed operating conditions.

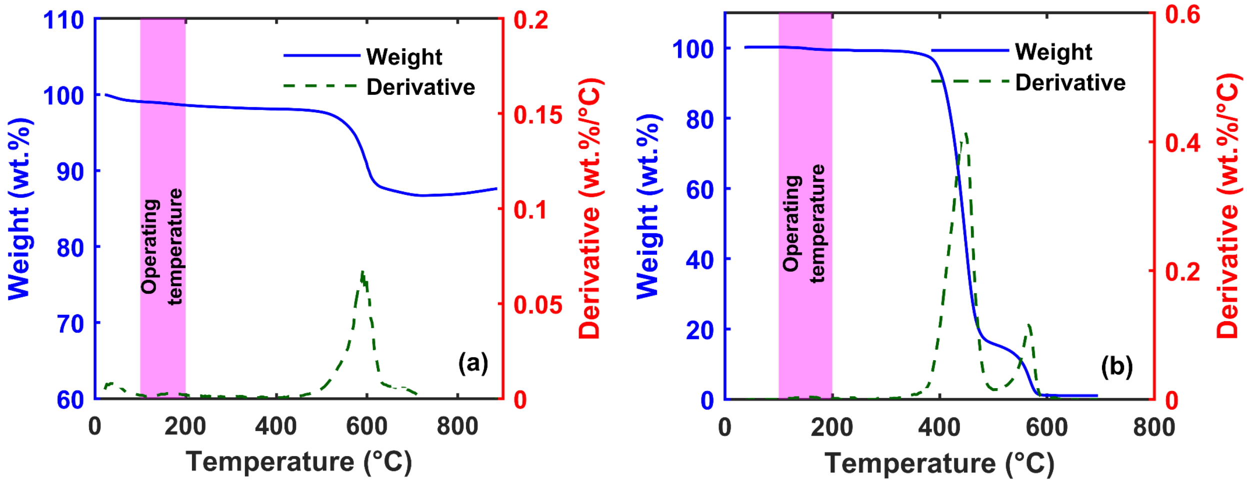

Figure 2.38. TGA curves of (a) nanoporous PSf layer and (b) PET non-woven fabric layer.

In order to evaluate the mechanical integrity of the selective layer, the mechanical property was measured by nanoindentation (MTS Nanoindenter® XP). The device was equipped with a

Berkovich indenter, the indentation by which was modeled as a paraboloid punch. The loading-unloading history is shown in Figure 2.37 (a). Each cycle consists of three phases: 1) loading (20 µm/s), 2) dwelling (30 s), and 3) unloading (–20 µm/s). After the first cycle, in which the load was up to 300 µN, the sample was reloaded for the second cycle, in which the load was doubled, up to 600 µN. The load-displacement profiles are shown in Figure 2.37 (b). As seen, the unloading curves in Cycle 1 and Cycle 2 were nearly indentically proportional to their corresponding loads, indicating that unloading behavior was purely elastic. Therefore, the Oliver–Pharr method [22] was used to calculate the reduced Young's modulus based on the unloading curves, by which a reduced Young's modulus of 0.93±0.02 GPa was determined. In comparison, polystyrene, a highly rigid thermoset, has a high modulus of 3–3.5 GPa, while flexible poly(tetrafluoroethylene) has a low modulus of 0.4 GPa [27]. Microstructurally, the nanosheets likely formed an aligned array, where the basal planes were perpendicular to the membrane's thickness direction [21]. The aligned nanosheets restricted the motion of the polymer chains, leading to higher resistance to deformation, i.e., enhanced mechanical strength. This set of data have substantiated the reinforcement effect of the nanofiller.

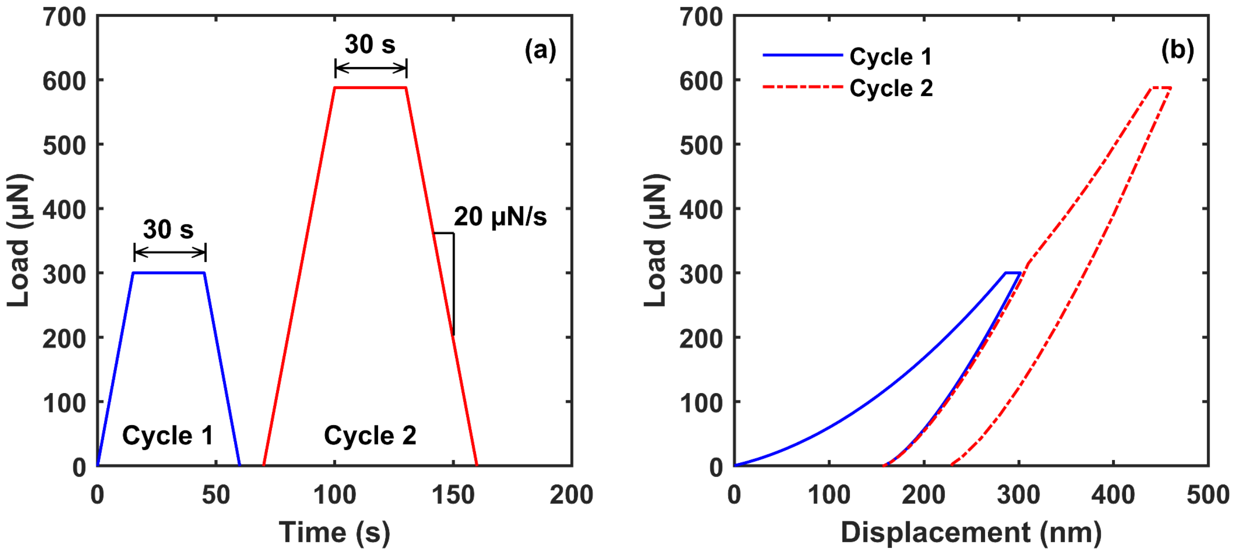

Figure 2.39. (a) Loading-unloading history and (b) load-displacement relationship of a free-standing film containing the perforated carbon nanosheet.

Scale-up Synthesis of Reinforcement Filler

In order to provide sufficient reinforcement filler for the membrane scale-up, the perforation and purification steps were further modified and scaled up. Firstly, the perforation agent was changed from HNO_3 to H_2O_2, which was more environmentally friendly. H_2O_2 can react with unsaturated carbon atoms at the damaged sites along with the existing edge sites of the carbon material, resulting in partial detachment and removal of carbon atoms from the sheet [28]. This will lead to the formation of a porous structure on the surface of the carbon material.

The most crucial and time-consuming parts of the bulk synthesis and perforation processes were both the purification steps. In BP1, a flat-sheet membrane with a surface area of 250 cm^2

was used for the tangential filtration. The purification conditions were optimized. Membrane fouling was significant when the concentration of the carbon material was 1 mg/mL. The purification process took ~7 days to purify ~2.8 g of the carbon materials. The insufficient membrane area and exhausting time were identified as the challenges for not only large-scale synthesis but also a high (> 1 mg/mL) concentration of the carbon material. The final carbon material product with a higher concentration is desirable, owing to advantages such as less area and resources for storage and transportation. In order to obtain a higher concentration, an additional centrifugation step (25 min at 10,000 rpm) was performed. However, this method was also time-consuming.

Keeping all the above points in mind, we have designed a new tangential filtration setup (see Figure 2.38) with a larger membrane area in order to purify a large quantity of the carbon material in less time. In order to increase the membrane area, the flat-sheet membrane has been replaced by a hollow-fiber membrane module. The effective area of the hollow-fiber membrane module was 0.92 m^2, which was ~36 times larger as compared to the flat-sheet membrane.

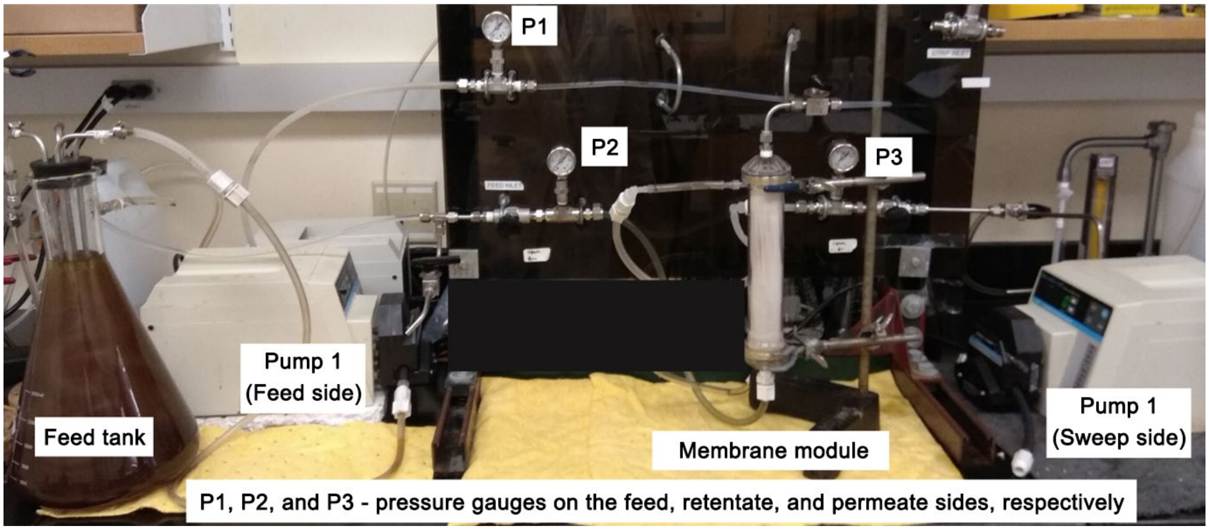

Figure 2.40. Photo of the high-capacity tangential filtration setup with a membrane area of 0.92 m^2.

This high-capacity tangential filtration setup was first used to tackle the purification steps in the bulk synthesis of the carbon material (see Figure 2.6 (a)). Owing to the specialty membrane material, we uncovered that the tangential filtration setup was inert to the harsh oxidant and deintercalation agents used in the bulk synthesis. This observation encouraged us to use the tangential filtration setup to replace the time-consuming centrifugation step for the removal of the excess reagents and byproducts.

The schematic of the improved bulk synthesis of the carbon material is illustrated in Figure 2.39. Initially, 500 mL solution containing the carbon material and the strong oxidant was diluted seven-fold with water to reach a final volume of 3.5 L. The diluted mixture was then fed to the tangential filtration setup (Filtration (1) in Figure 2.39), which fully removed the excess oxidant in ~ 12 min. Since no purge flow was used on the permeate side of the hollow-fiber module, the carbon material could form a cake layer on the membrane. Therefore, a backwashing was conducted with RO water afterward to fully recover the carbon material. Then, the recovered carbon material was stirred in a HCl solution to dissolve any metal ions (M^{n+}) complexed to the carbon material. This mixture was then fed into the tangential filtration setup again (Filtration (2) in Figure 2.39) to remove the majority of the HCl and the dissolved metal ions. In order to prevent the membrane fouling, this filtration step was conducted for ~14 min. The mixture with weak acidity was reintroduced to the tangential filtration setup with a sweep stream of RO water running countercurrently (Filtration (3) in Figure 2.39). This step fully removed the remaining HCl in ~55 min. Finally, the purified carbon material was fed to the tangential filtration setup for the last time (Filtration (4) in Figure 2.39), in which the hollow-fiber module removed certain amount of water and concentrated the carbon material to 6 mg/mL in ~15 min. Overall, the improved process took ~1.6 h to produce 7 g of carbon material, which increased the productivity by a factor of 105 compared to the previous process (see Figure 2.6 (a)).

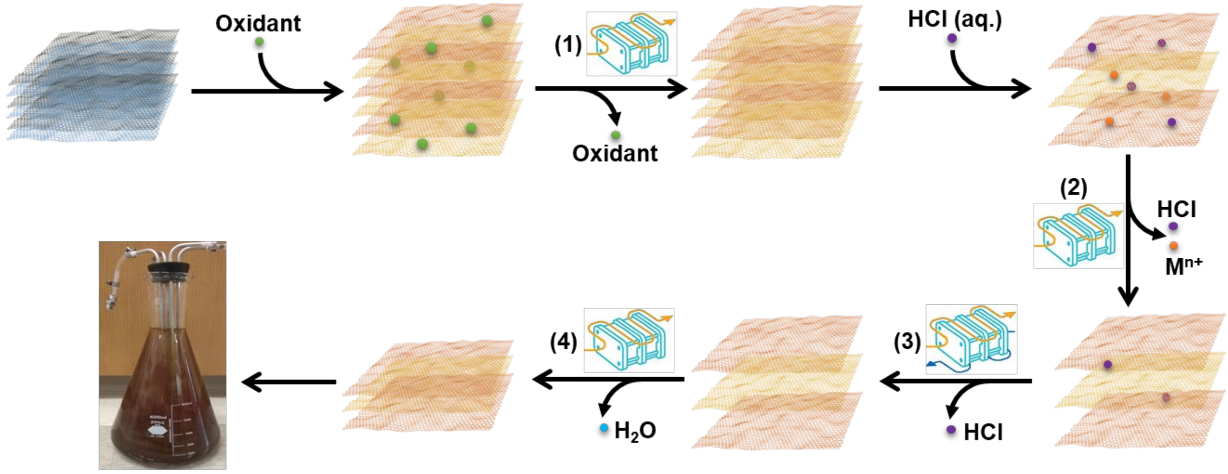

Figure 2.41. Improved bulk synthesis of the carbon material enabled by the high-capacity tangential filtration setup.

The new tangential filtration setup can also be used to scale up the purification steps involved in the perforation process (see Figure 2.6 (b)). Because the perforation agent (i.e., H_2O_2) was much less aggressive than the strong oxidant (HNO_3) and HCl, the application of the tangential filtration setup was straightforward. The improved perforation process is illustrated in Figure 2.40.

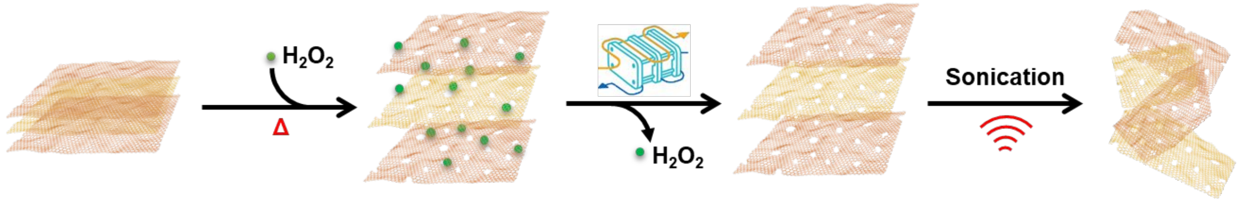

Figure 2.42. Improved perforation of the carbon material enabled by the high-capacity tangential filtration setup.

In order to evaluate the textural properties of the perforated carbon material synthesized by the scaled-up process, AFM analysis was performed, and the images are shown in Figure 2.41. The monolayer of the carbon material (Figure 2.41 (a)) had a sheet width of ca. 700 nm. Furthermore, the pores on the surface were examined by scanning the surface of the same carbon material (Figure 2.41 (b)). The 3D image was generated based on the flooding mode that covers all the areas except the pores (Figure 2.41 (c)). The pores of the carbon material were in the range of 2–12 nm, and the surface porosity was ~2.5 %.

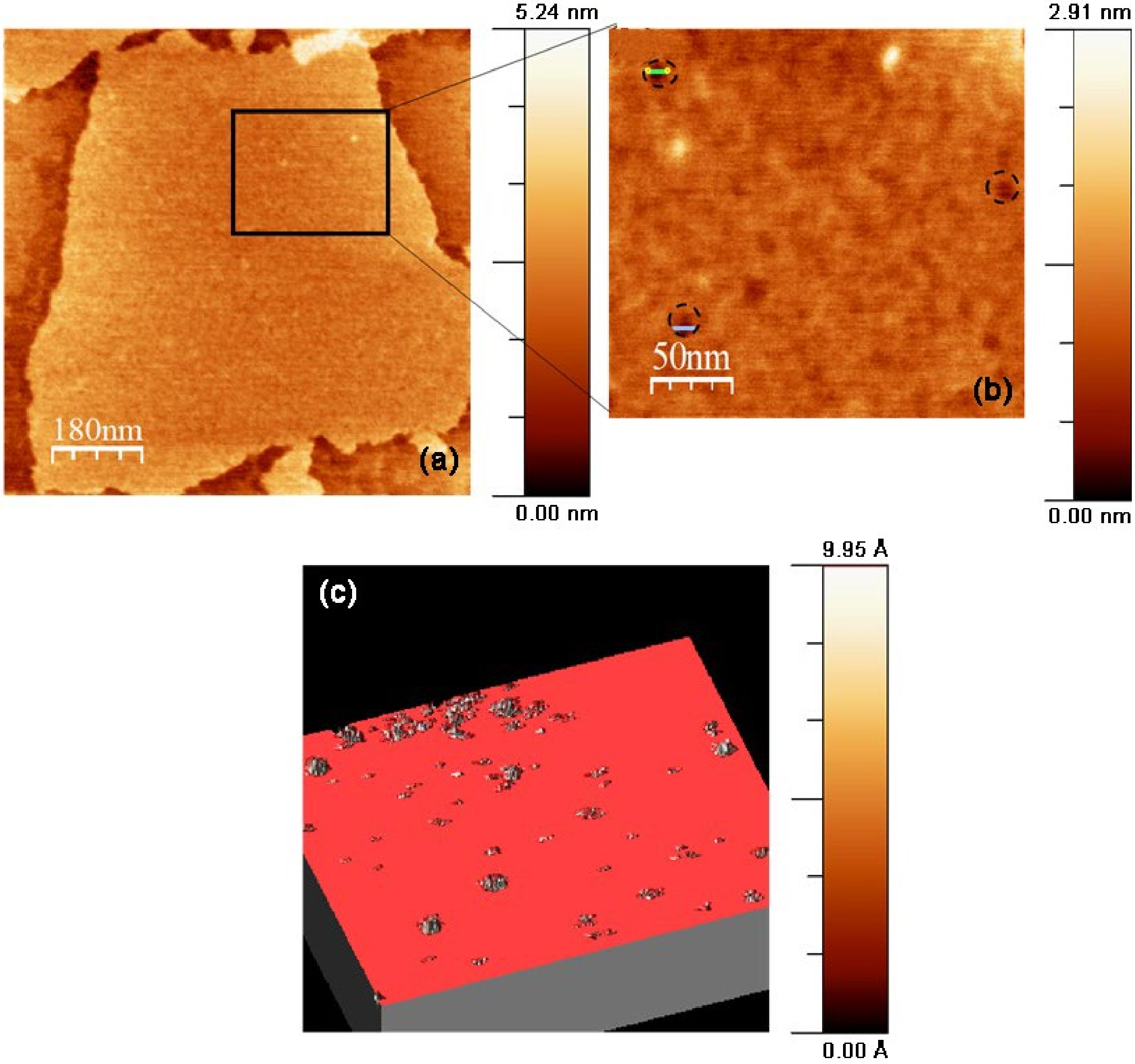

Figure 2.43. AFM images of the carbon material with different scanning areas (a) 883 nm × 883 nm, (b) 248 nm × 205 nm, and (c) 3D view of the flooding image showing pores on the surface.

The pore size and porosity were further tuned by altering the H_2O_2 concentration and thermal treatment time. Three batches of perforated carbon materials were prepared as listed in Table 2.3, and their textual properties are summarized in Figure 2.42. As shown in this figure, by using harsher perforation conditions, the porosity increased significantly from 2.5 to 9.1%. The increased porosity could decrease the transverse diffusion length of gas molecules and hence mitigate their mass transfer resistances through the carbon material. On the other hand, the pore size distributions thus obtained were all in the range of 2–16 nm, indicating a negligible effect of perforation conditions on the pore size distribution. The available literature suggested that further extension of the treatment time might lead to aggressive etching of the carbon material, increase in the pore size, sheet breakage, and complete destruction [29,30]. Hence, conditions like temperature, amount of H_2O_2, and treatment time are crucial factors that can affect the overall pores size, pore density, and porosity of the carbon materials.

Table 2.3. Perforated carbon materials synthesized by the improved procedures.

Sample	H_2O_2%	Temperature	Treatment time
A	Low	High	Short
B	High	High	Long
C	Medium	High	Long

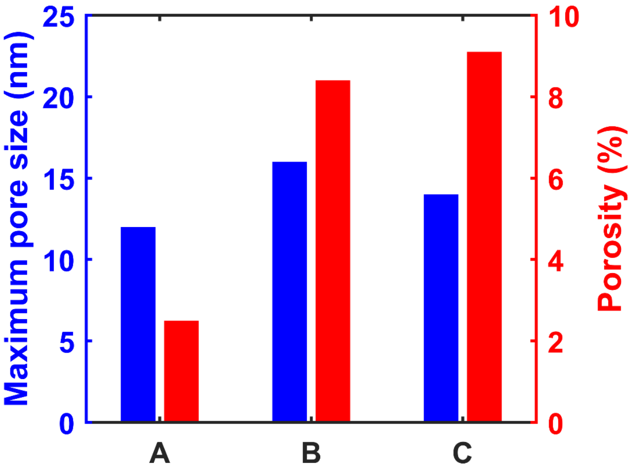

Figure 2.44. Maximum pore sizes and porosities of perforated carbon materials listed in Table 2.3.

Enhancement of H_2S/CO_2 Selectivity

In BP1, a single-stage Selexol process was used to remove the H_2S from the captured CO_2. This step was then identified as a major cost center for the COE with carbon capture. As exemplified in Section 2.1.13, the Selexol process can be replaced by a continuous membrane column, provided that the H_2S/CO_2 selectivity was greater than 10. This motivated the synthesis of task-specific mobile carriers for selective H_2S removal against CO_2.

H_2S is generally more permeable than CO_2 in amine-containing membranes. Due to its acidic nature and inability of nucleophilic addition, H_2S reacts with amine via proton transfer:

$$H_2S + R\text{–}NH_2 \rightleftharpoons HS^- + R\text{–}NH_3^+$$
$$HS^- + R\text{–}NH_2 \rightleftharpoons S^{2-} + R\text{–}NH_3^+$$

Because of the smaller kinetic diameter of proton, these reactions are generally faster than the reaction between CO_2 and amine [9,31,32]. In addition, the reaction between this Brønsted acid–base pair is not restricted by the steric hindrance of the amine due to the small proton size. Rather, a more hindered amine, typically possessing a higher pKa, reacts with H_2S more swiftly. On the contrary, steric hindrance retards the carbamate bond formation significantly, and the amine–CO_2 reaction rate reduces with increasing steric hindrance. Based on this difference, we devise new aminoacid salt carriers with severe steric hindrance to achieve higher H_2S/CO_2 selectivity. In accordance with this rationale, six aminoacid salts, Compounds IV–IX were synthesized as H_2S mobile carriers, which are described below.

Compound IV – Unhindered 1° aminoacid salt: This carrier was synthesized from an off-the-shelf aminoacid salt containing a 1° amino group. The aminoacid was deprotonated by an equimolar amount of KOH to form the aminoacid salt. This carrier served as a reference for comparison.

Compound V – Mildly hindered 2° aminoacid salt: This carrier was synthesized from an off-the-shelf aminoacid salt containing a 2° amino group. The aminoacid was deprotonated with an equimolar amount of KOH to form the aminoacid salt. This carrier also served as a reference for comparison.

Compound VI – Severely hindered 2° aminoacid salt: This carrier was synthesized by the alkylation of a hindered 1° amine by a bromo ester as shown in Figure 2.43. The hindered 1° amine acted as a nucleophile and attacked the bromo ester to form an amino ester. K_2CO_3 was used to abstract the bromide formed during the reaction. The reaction was carried out overnight in acetonitrile (ACN), using excess of amine and elevated temperatures to drive the conversion. After the reaction, the resultant mixture was cooled to ambient temperature, filtered to remove insoluble inorganic salts, and concentrated by evaporation under vacuum. The solution thus obtained was acidified using dilute HCl to a pH of 1 in order to carry out the acid hydrolysis of the amino ester. The hydrolysis was carried out overnight at 90°C in a methanol-water medium. The resultant mixture was cooled to ambient temperature and ion-exchanged to remove the excess acid. The solution was then evaporated under vacuum to obtain the severely hindered 2° aminoacid product.

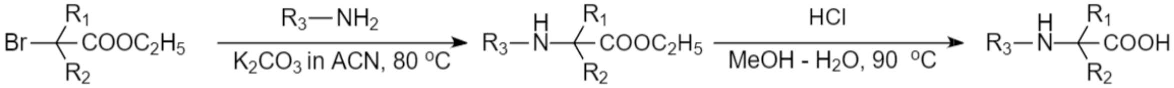

Figure 2.45. Synthesis of Compound VI, a severely hindered 2° aminoacid salt, from 1° amine and bromo ester. R_1, R_2 and R_3 represent alkyl substituents.

Compound VII – More severely hindered 2° aminoacid salt: A more severely hindered 2° aminoacid salt was synthesized via the route shown in Figure 2.44. A hindered bromo ester and a hindered 1° amine were dissolved in ACN, along with a stoichiometric amount of K_2CO_3. The hindered 1° amine acted as a nucleophile and attacked the bromo ester to form an amino ester. The reaction mixture was stirred overnight at 80°C to drive the conversion. After the reaction, the solution was cooled to ambient temperature, filtered to remove insoluble inorganic salts, and evaporated under vacuum to remove the ACN. The residue was extracted with ethyl acetate. The ethyl acetate layer was then washed several times with saturated brine to remove residual water. The organic layer was then evaporated under vacuum to obtain the crude amino ester. The crude ester was then dissolved in methanol (MeOH) for base hydrolysis. Excess KOH was added to drive the hydrolysis. The reaction mixture was stirred at ambient temperatures overnight. After the reaction, ion exchange was used to remove the KOH. The resultant solution was then evaporated under vacuum to give the severely hindered 2° aminoacid salt.

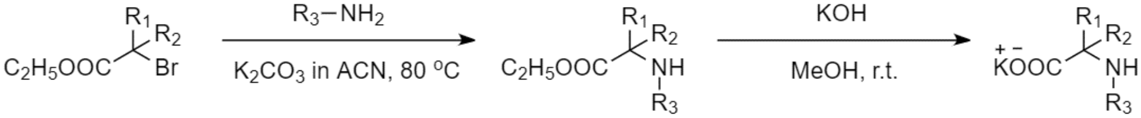

Figure 2.46. Synthesis of Compound VII, a more severely hindered 2° aminoacid salt from 1° amine and bromo ester. R_1, R_2, and R_3 represent alkyl substituents.

Compound VIII – More severely hindered 2° aminoacid salt with a hydrophilic functional group: In order to address issues of low solubility associated with severely hindered aminoacid salts, a hydrophilic functional group is devised to be incorporated into the alkyl fragment. A synthesis route has been designed as shown in Figure 2.45. A trichloromethide anion is formed from chloroform and acetone under strong basic conditions, which can attack an amine to form the aminoacid salt.

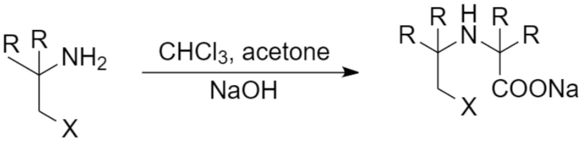

Figure 2.47. Synthesis of more severely hindered aminoacid salt with a hydrophilic group. R represents an alkyl substituent or a hydrogen; X represents a hydrophilic group.

Compound IX – 3° aminoacid salt: This carrier was synthesized by the reductive alkylation of a hindered 1° amino acid as shown in Figure 2.46. The reductive alkylation was carried out using zinc dust in aqueous alkaline media according to the procedure described by Giovanni et al. [33]. KOH was used to provide the basic medium necessary to deprotonate the aminoacid and to promote the imine reduction by zinc. In order to drive the conversion and obtain a satisfactory yield, it was necessary to use excess zinc and aldehyde. Depending on the reaction time and the aldehyde concentration, the 1° amine could be completely converted to a 3° amine. After the reaction, ion exchange was conducted to remove the KOH. The resultant mixture was then filtered to remove insoluble zinc salts and evaporated under vacuum to obtain the 3° aminoacid. The aminoacid thus obtained was further purified by re-dissolving in methanol and evaporation under vacuum to afford the pure product. This compound was converted into its aminoacid salt and then used to synthesize membranes.

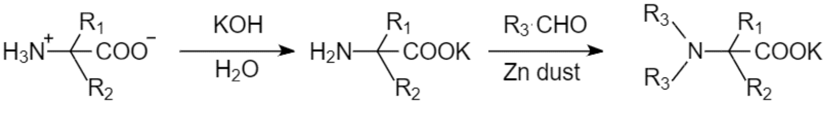

Figure 2.48. Synthesis of Compound IX, a 3° aminoacid salt, from hindered 1° aminoacid. R_1, R_2 and R_3 represent alkyl substituents.

Crosslinked polymer matrix devoid of CO_2-philic functionalities: The polymer network used to synthesize Membranes M4 and M15 contained a strongly hydrogen-bonding functional group, which could promote the CO_2 transport through favorable hydrogen bonding with the bicarbonate anion, the reaction product of CO_2 and water. In order to improve the H_2S/CO_2 selectivity, this CO_2-philic functional group was eliminated via a crosslinking reaction as shown in Figure 2.47. The crosslinked polymer lacked electropositive hydrogen atoms. This should reduce the favorable hydrogen-bonding interactions with CO_2 and hence increase the H_2S/CO_2 selectivity. This polymer network was used to host Compounds IV–IX to form the membranes. For each carrier, moderate and high contents of the carrier were incorporated in the crosslinked polyalcohol to form the membranes, which are listed in Table 2.4.

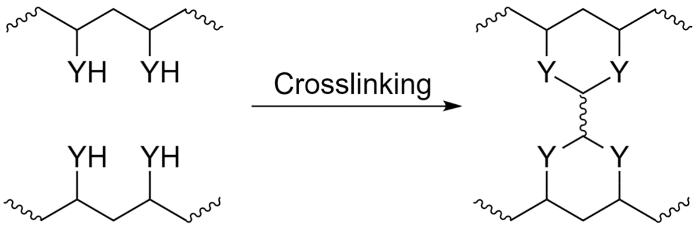

Figure 2.49. Crosslinking of polymer matrix to eliminate a functional group that can form hydrogen bond with bicarbonate. Here, –YH represents the hydrogen bond donor.

Table 2.4. Representative membrane compositions and thicknesses for selective H_2S removal.

Amine type	M #	Mobile carrier	Steric hinderance	Carrier content	Thickness (μm)
1°	16	Compound IV	None	Moderate	10
	17	Compound IV	None	High	10
2°	18	Compound V	Low	Moderate	10
	19	Compound V	Low	High	10
	20	Compound VI	Moderate	Moderate	10
	21	Compound VI	Moderate	High	10
	22	Compound VII	High	Moderate	10
	23	Compound VII	High	High	10
	24	Compound VIII	Very high	Moderate	10
	25	Compound VIII	Very high	High	10
3°	26	Compound IX	Not applicable	Moderate	10
	27	Compound IX	Not applicable	High	10

2.1.6 Task 6 – Optimized Membrane Characterization

Summary

- The stabilities of the best membranes tailored for the feed inlet (Membrane M15) and retentate outlet (Membrane M4) were tested at 107°C with a CO_2 partial pressures of 13.8 and 1.1 bar, respectively.
- Both membranes exhibited stable performances for 120 h at 107°C and a total feed pressure of 35 bar.
- The CO_2/H_2 separation results were affected significantly by the operating temperature, and both membranes exhibited the best performances at 107°C.
- The membrane containing Carrier VIII (Membrane M25) exhibited a H_2S permanence of 560 GPU and a H_2S/CO_2 selectivity of 19.5 with a feed containing 1.2% H_2S.
- For this membrane, a strong dependence of the H_2S permeation on the H_2S concentration was observed. Contrarily, the CO_2 permeation was rather insensitive to the feed gas composition.
- At a reduced H_2S concentration of 0.5%, Membrane M25 exhibited a very high H_2S permeance of 764 GPU and a high H_2S/CO_2 selectivity of 25.2.
- A theoretical model was developed to analyze the carrier saturation behaviors. The model clearly indicated that the severely hindered amine carrier (Carrier VIII) was largely inactive to react with CO_2, which corresponded to its high H_2S/CO_2 selectivity.

Membrane Stabilities with Simulated Syngas

The 120-hour stabilities of the best membranes tailored for the feed inlet (Membrane M15) and retentate outlet (Membrane M4) were tested at 107°C, a feed pressure of 35 bar, and a permeate pressure of 1.1 bar. The simulated syngas was conditioned at a CO_2 partial pressure of 13.8 bar for the feed-inlet membrane containing Compound II (multifunctional alkanolamine) as the mobile carrier; for the retentate-outlet membrane containing Compound I (sterically hindered aminoacid salt) as the mobile carrier, the CO_2 partial pressure was at 1.1 bar.

As shown in Figure 2.48 (a), the feed-inlet membrane exhibited an average CO_2 permeance of 310 GPU with a CO_2/H_2 selectivity of 125 and remained stable for 120 h. Similarly, the retentate-outlet membrane also showed a stable performance with a permeance of 217 GPU and a CO_2/H_2 selectivity of 268. Although a longer and more thorough test is needed, the 120-h stability has shed promising light on the following aspects. First, Compounds I and II likely possess essentially no volatility in the polymeric membrane, which minimizes the possibility of loss through volatility. Second, the high level of H_2S does not affect the transport performance of the carrier to a significant extent, which is likely due to the weak acidity of H_2S; a cumulation of sulfur species in the membrane is not anticipated. Third, the polymer matrix is fully rubbery and not subject to a conformational relaxation, i.e., no physical aging is expected. These three aspects are in line with the thermogravimetric analysis described in Section 2.1.5.

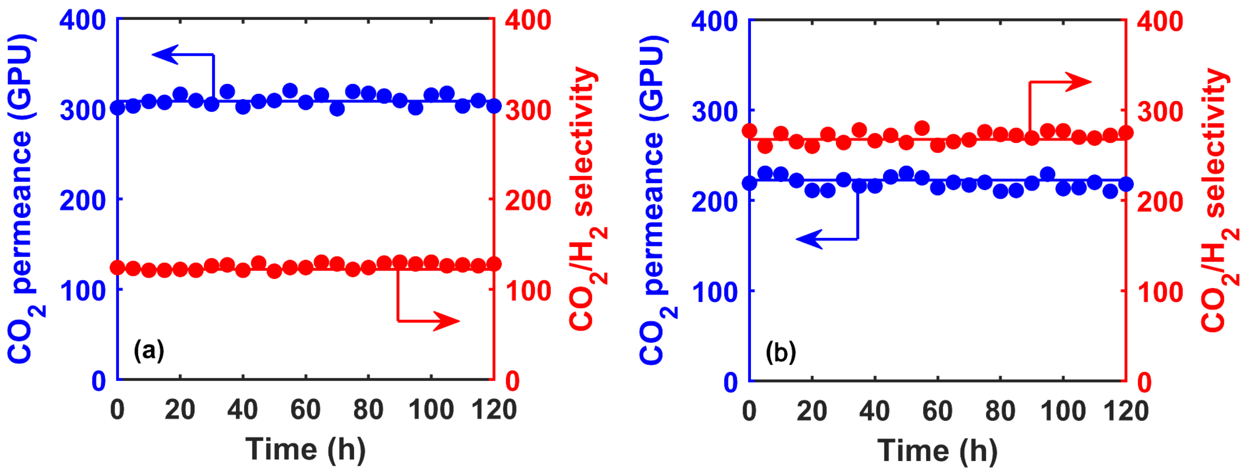

Figure 2.50. Stabilities of membranes tailored for the (a) feed inlet and (b) retentate outlet at 107°C with the CO_2 partial pressures of 13.8 and 1.1 bar, respectively.

Effect of Operating Temperature

The membranes tailored for the feed inlet and retentate outlet were tested at 100–120°C, a feed pressure of 35 bar, and a permeate pressure of 1.1 bar. The simulated syngas was conditioned at a CO_2 partial pressure of 13.8 bar for the feed-inlet membrane; for the retentate-outlet membrane, the CO_2 partial pressure was at 1.1 bar.

As shown in Figure 2.49 (a), the feed-inlet membrane exhibited an average CO_2 permeance of 236 GPU with a CO_2/H_2 selectivity of 100 at 100°C. The permeance and selectivity increased to 312 GPU and 126, respectively, when the temperature increased to 107°C. At 114°C, the permeance further increased to 373 GPU but the selectivity reduced to 75. An even higher temperature at 120°C, however, resulted in the reduced permeance and selectivity of 171 GPU and 50, respectively.

Similarly, the performance of the retentate-outlet membrane also showed a strong dependence on the operating temperature as seen in Figure 2.49 (b). At 100°C, the membrane exhibited a CO_2 permeance of 175 GPU and a CO_2/H_2 selectivity of 242. An increased temperature at 107°C improved the permeance to 219 GPU as well as an increased selectivity of 267. However, both the permeance and selectivity reduced considerably at higher temperatures. For instance, the membrane showed a low permeance of 117 GPU and a relatively low selectivity of 167 at 120°C.

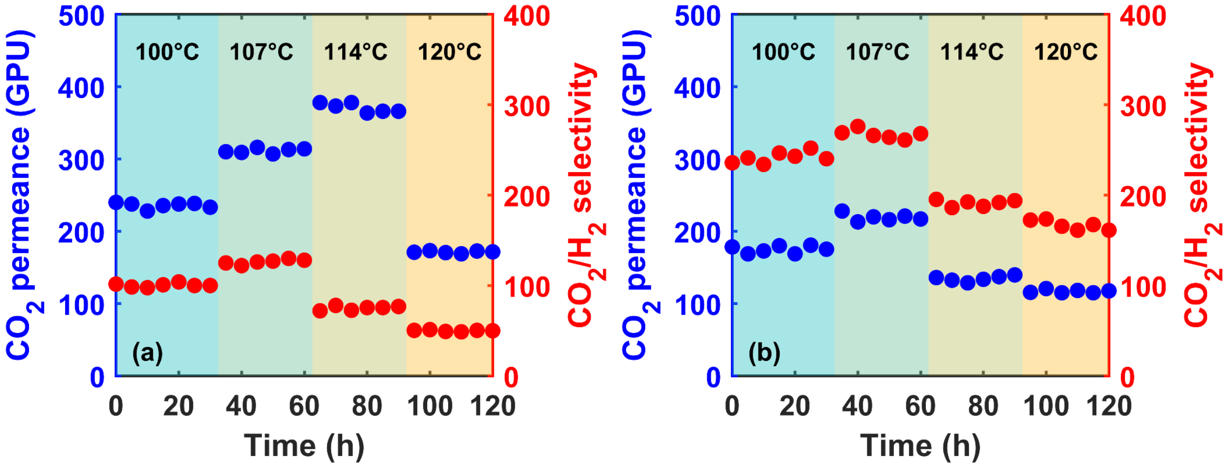

Figure 2.51. Separation performances of membranes tailored for the (a) feed inlet and (b) retentate outlet at 100–120°C with the CO_2 partial pressures of 13.8 and 1.1 bar, respectively.

In general, the initial increase in the permeance and selectivity with increasing temperature was attributed to the faster gas diffusion in the membrane. At a temperature higher than 107°C, however, the reduced physisorption and chemisorption of CO_2 outweighed any increase in the diffusivity, thereby resulting in the reduced separation performances. In addition, the polymer network tended to be less swollen at a higher temperature due to the reduced water sorption. Consequently, the gas diffusion could be hindered by the more compact polymer chain packing.

Effect of Steric Hindrance on the H_2S/CO_2 Separation

The membranes containing the amine carriers with different degrees of steric hindrance (see Table 2.4) were tested at 107°C and 7-atm feed pressure with a feed gas containing 1.2% H_2S and balance of CO_2. The feed gas was fully saturated with water vapor at the given temperature and pressure. The results for the membranes containing a moderate content of the carriers (i.e., M16, M18, M20, M22, M24, and M26 in Table 2.4) are shown in Figure 2.50 (a). With the increasing degree of steric hindrance from Carrier IV to Carrier VIII, the H_2S/CO_2 selectivity increased from 5.3 to 16.8, which could be attributed to the weakened amine–CO_2 reaction when the steric hindrance was severe. No clear correlation was observed between the H_2S permeance and the degree of steric hindrance. However, the more hindered carrier (e.g., Carriers VI– VIII) rendered a higher H_2S permeance in the range of 360–470 GPU, which was considerably higher than the unhindered Carrier IV (250 GPU). For the tertiary amine Carrier IX, the corresponding membrane exhibited a H_2S/CO_2 selectivity of 17.7 with a H_2S permeance of 740 GPU.

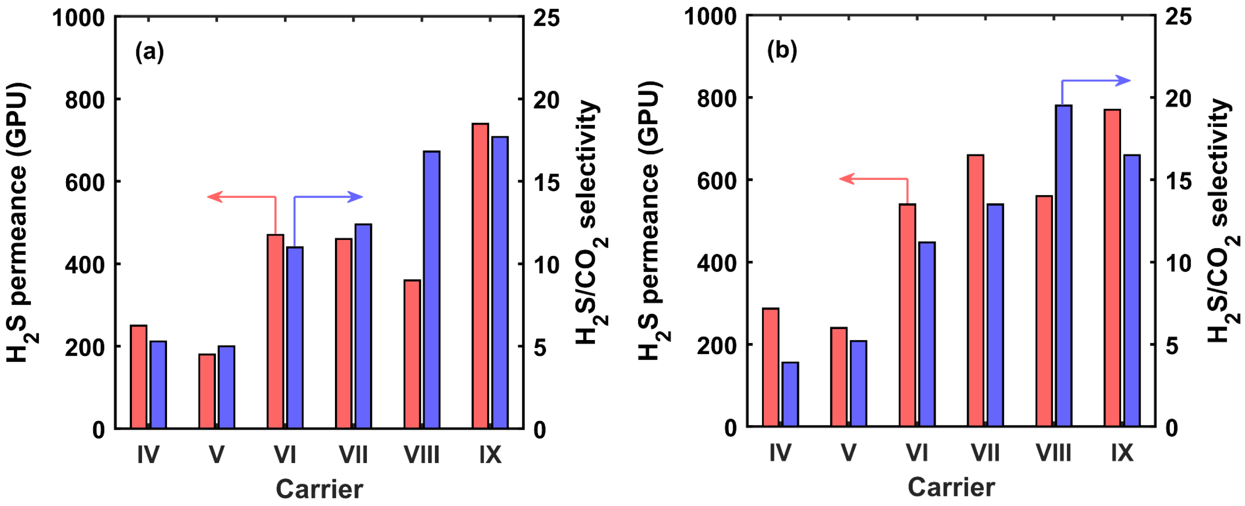

Figure 2.52. H_2S permeances and H_2S/CO_2 selectivities of membranes containing (a) moderate and (b) high contents of amine carriers as listed in Table 2.4.

The membranes containing a high content of the carriers (i.e., M17, M19, M21, M23, M25, and M27 in Table 2.4) were also tested at the same conditions, and the results are shown in Figure 2.50 (b). In general, a higher carrier content increased the H_2S permeance. For instance, higher contents of Carriers VII and VIII resulted in an increase in the H_2S permeance of ca. 200 GPU. The best performance was achieved by the membrane containing Carrier VIII (i.e., M25), which demonstrated a H_2S permeance of 560 GPU and a H_2S/CO_2 selectivity of 19.5.

In view of the promising performance of the Membrane M25, it was used to study the effect of H_2S concentration on the separation performance. The feed H_2S concentration was varied in the range 0.5–30%, and the results are shown in Figure 2.51. As seen, appreciable increases in the H_2S permeance and H_2S/CO_2 selectivity were observed with reducing H_2S concentration. At ca. 30% H_2S, Membrane M25 exhibited a permeance of 217 GPU and a selectivity of 7.7. By reducing the H_2S concentration to 0.5%, the membrane rendered a high permeance of 764 GPU and a high selectivity of 25.2. The uprising H_2S permeance could be attributed to the mitigated carrier saturation, through which the Carrier VIII because more available for the facilitated transport of H_2S when the H_2S concentration was lower [34,35]. On the contrary, the CO_2 permeance remained at ca. 30 GPU, which suggested that the CO_2 permeation was mainly based on the solution-diffusion mechanism rather than the facilitated transport mechanism. This might be due to the severe steric hindrance of Carrier VIII, which resulted in its inability to react with CO_2.

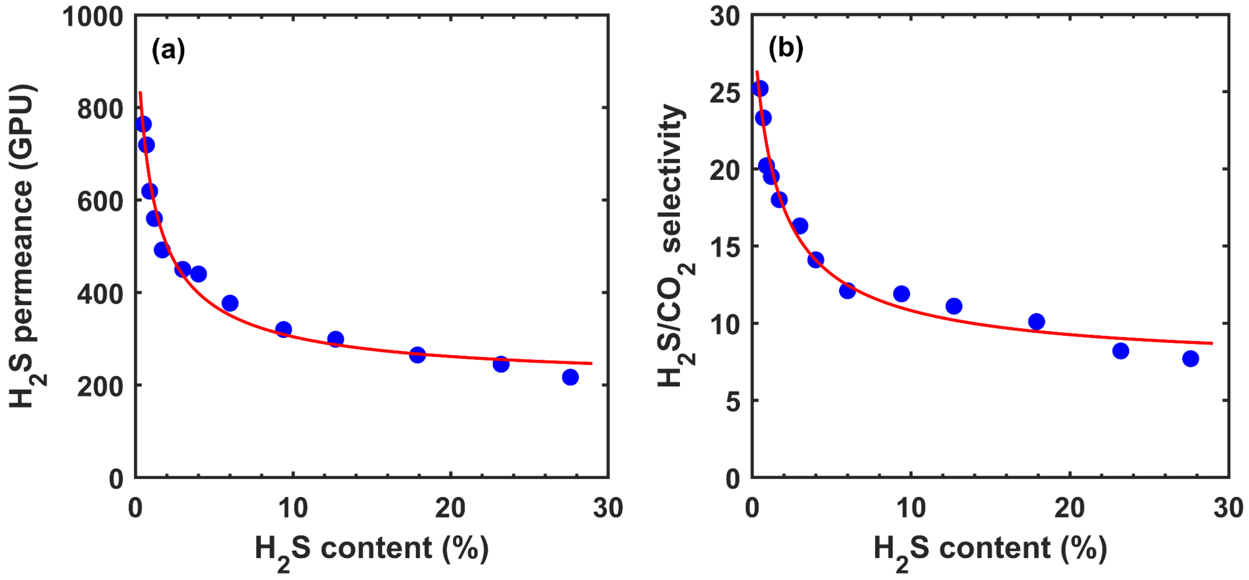

Figure 2.53. (a) H_2S permeances and (b) H_2S/CO_2 selectivities of the membrane containing Carrier VIII (M25) at different feed H_2S contents. The trendlines are only for the guide of the eyes.

In order to further analyze the carrier saturation behaviors, Membrane M25 containing the severely hindered carrier vs. Membrane M17 containing the unhindered carrier (Carrier IV) were further analyzed, and a homogeneous reactive diffusion model has been developed with the following assumptions:

- The solution-diffusion mechanism is negligible compared to the facilitated transport of H_2S and CO_2.
- H_2S reacts with the carrier as:

  $$H_2S + R\text{–}NH_2 \rightleftharpoons HS^- + R\text{–}NH_3^+$$

- CO_2 reacts with the carrier as:

  $$CO_2 + R\text{–}NH_2 + H_2O \rightleftharpoons HCO_3^- + R\text{–}NH_3^+$$

- The pH does not change significantly throughout the membrane due to the high carrier content.
- Both reactions are at equilibrium, and electroneutrality can be assumed throughout the membrane.
- The water concentration is treated as a constant due to its abundancy in the membrane.

With these assumptions, the concentration of HS^- in the membrane at the feed/membrane interface ($c_{\mathrm{HS^-}}$) can be related to the H_2S mole fraction in the feed gas ($x_{\mathrm{H_2S}}$), and the fluxes of HS^- and H_2S can be estimated as:

$$J_{H_2S} = J_{HS^-} = \frac{D_{HS^-}}{\ell}(c_{HS^-} - 0) \tag{1}$$

where D_{HS^-} is the diffusivity of HS^- and ℓ the membrane thickness. After normalizing the H_2S flux by the transmembrane driving force ($p^h x_{H_2S}$), the H_2S permeance (P_{H_2S}/ℓ) takes a simplified form as:

$$\frac{P_{H_2S}}{\ell} = \frac{J_{H_2S}}{p^h x_{H_2S}} = \frac{1}{\sqrt{a\, x_{H_2S} + b(1 - x_{H_2S})}} \tag{2}$$

where the fitting parameters a and b describe the overall affinity of the carrier to H_2S and CO_2, respectively, and p^h is the feed pressure. In other words, a larger b value indicates a stronger competitive transport of CO_2 against H_2S. The fitting results are also shown in Figure 2.52 with the red lines representing the best fits and the red shades depicting the fitting errors. The determined fitting parameters are listed in Table 2.5.

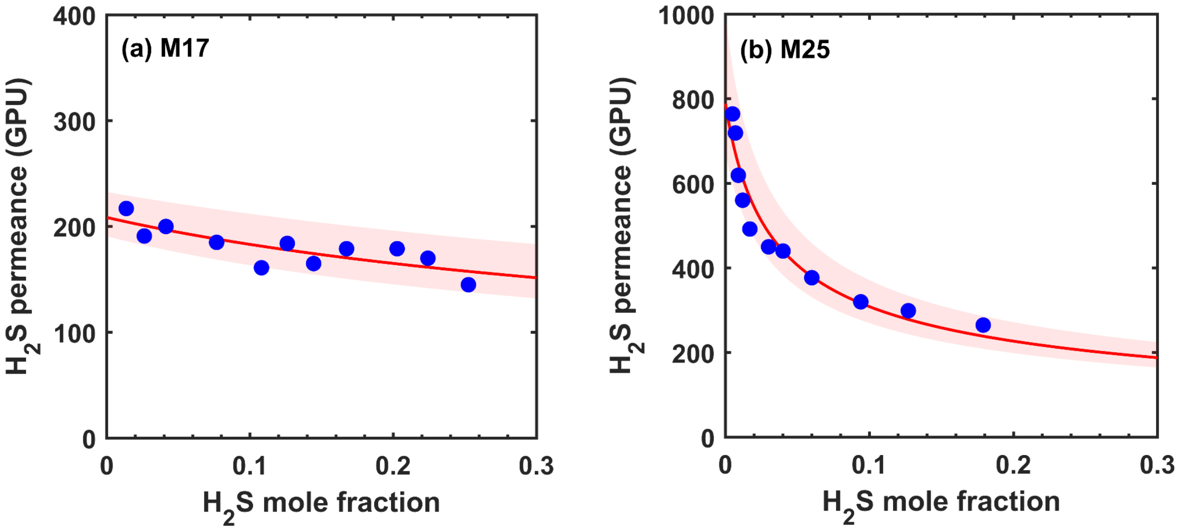

Figure 2.54. H_2S permeances of Membranes (a) M17 and (b) M25 at different feed H_2S mole fractions. The red lines are the best fit based on Eq. (2), and the red shades represents the fitting errors.

Table 2.5. Fitting parameters based on Eq. (2) for Membranes M1 and M2.

Membrane #	a (10^{-5} GPU^{-2})	b (10^{-5} GPU^{-2})
M17	9.14 ± 3.53	2.30 ± 0.45
M25	9.06 ± 2.70	0.16 ± 0.06

As shown in this figure, the model can describe the carrier saturation behaviors relatively well. The determined values of a were similar for both membranes (ca. 9.0×10^{-5} GPU^{-2}), indicating that steric hindrance did not have a significant effect on the H_2S–carrier reaction. On the contrary, the *b* value for Membrane M17 (2.3×10^{-5} GPU^{-2}) was considerably higher than that for Membrane M25 (0.16×10^{-5} GPU^{-2}). These results further confirmed that the transport of CO_2 could be stifled by increasing the steric hindrance of the amine carrier. Experimentally, we observed that the CO_2 permeance of Membrane M25 remained low at ca. 30 GPU regardless of the CO_2 mole fraction, which was consistent with the inability of Carrier VIII to react with CO_2.

Another insight from this mathematical analysis was the competitive facilitated transport between H_2S and CO_2. The weak concentration dependence as illustrated in Figure 2.52 (a) for Membrane M17 did not suggest a weak reaction between Carrier IV and H_2S. Rather, Membranes M17 and M25 possessed similar a values, which suggested similar reactivity for Carriers IV and VIII with H_2S. For Membrane M17, the low H_2S permeance at a reduced H_2S mole fraction was mainly due to the severe competitive facilitated transport of CO_2. For this reason, the experimentally measured H_2S/CO_2 selectivities for Membrane M17 were all in the range of 3–4 regardless of the H_2S mole fraction.

2.1.7 Task 7 – Optimized Membrane Scale-up Fabrication

Summary

- The roll-to-roll continuous coating machine at OSU has been adjusted for the prototype membrane coating, including the alignment of a 21-inch wide polymer support, the calibration of the coating knife, and the operation of the convection oven for membrane curing.
- In order to prevent the pin-hole defect formation on the membrane in the roll-to-roll continuous coating process, a method was established to neutralize the surface charge on the polymer support prior to coating. The charge neutralizing device was installed on the continuous coating machine, which successfully eliminated any defects in the selective layer.
- In total, 105 ft of scale-up membranes were fabricated for prototype membrane module rolling.

Roll-to-Roll Continuous Coating Machine

The scale-up fabrication of the membrane was demonstrated by using the pilot-scale thin-film coating (TFC) assembly of the continuous roll-to-roll machine at OSU. The setup of the thin-film coating assembly of the coating machine for the scale-up fabrication of membranes is shown schematically in Figure 2.53 (a). The 21-inch wide PSf substrate roll at the unwind roll was rotated by the unwind motor to deliver the web onto the coating knife assembly. Before passing through the coating knife, the substrate was treated by a charge neutralizer to avoid pin-hole formation during the coating (see Figure 2.53 (b)). The coating solution was stored in the coating trough chamber between the coating knife and the back plate. The thickness of the membrane was controlled by setting the gap between the coating knife and the base of the coating knife assembly (gap setting, as shown in Figure 2.53 (b)) as well as the coating speed of the PSf substrate roll. The coated membrane was dried and cured at 120°C for 16 minutes inside the convection oven by flowing hot air into the oven for a complete removal of the solvent and a complete crosslinking reaction of the polymer network. The tension used to flatten the PSf substrate rolls was 10 lb_f. A photo of the continuous coating machine is shown in Figure 2.53 (c).

With the installed charge neutralizer, pin-hole defects were successfully eliminated, rendering a quality coating of the selective layer. More importantly, an overly viscous coating solution was not required for avoiding the pin-hole formation in the improved process. Therefore, the shelf life of the coating solution was significantly prolonged, and the time window for coating was extended. A photo of the fabricated membrane is shown in Figure 2.53 (d). Multiple scale-up coating runs were conducted with the conditions listed in Table 2.6. FTM2 prototype membrane was for the feed-inlet membrane containing Compound II as the mobile carrier. FTM1 prototype membrane was for the retentate-outlet membrane containing Compound I as the mobile carrier. In total, ca. 50 ft of scale-up membrane was fabricated for each membrane type, which was used for the spiral-wound membrane element rolling.

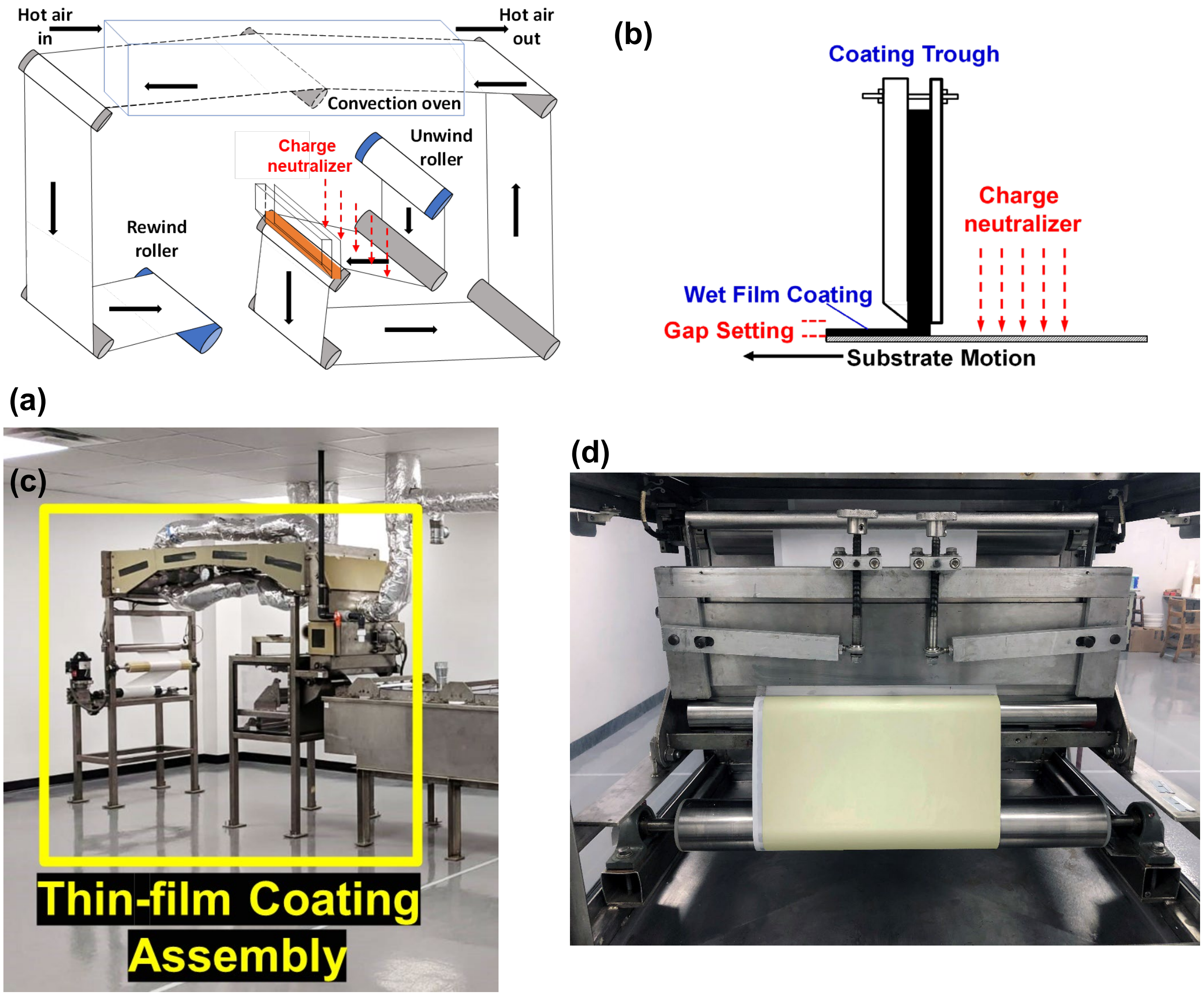

Figure 2.55. Pilot-scale coating machine for the scale-up fabrication of membranes: (a) schematic of the machine setup, (b) schematic of the coating knife assembly, (c) photo of the coating machine, and (d) photo of fabricated membrane.

Table 2.6. Scale-up coating conditions for scale-up membranes fabricated in this project.

Membrane Type	Carrier	Corresponding lab-scale membrane	Targeted thickness (μm)	Length (ft)
I	Compound II	M15	15	50
II	Compound I	M4	25	55

2.1.8 Task 8 – Optimized Scale-up Membrane Characterization

Summary

- The uniformity of the selective layers was evaluated, which indicated that the targeted thicknesses and a good uniformity were successfully achieved using the continuous coating machine.
- The scale-up membranes showed good CO_2/H_2 separation performances on par with those synthesized in lab scale.

Quality Control of Selective Layer Coating

In order to assure the uniformity of the selective layer, multiple membrane samples were taken from the far left, left, middle, right, and far right locations across width direction for scale-up FTM2 and FTM1 membranes. The selective layer thicknesses were measured by a Mitutoyo electronic indicator (Model 543-252B, Mitutoyo America Corp, Aurora, IL) with an accuracy of ±0.5 μm, and the results are shown in Figure 2.54. In the boxplot, the band in the box is the median, and the whiskers represent the maximum and minimum of the data set. The top and bottom bands delimiting the box are the first and third quartiles. As seen, most of the regions rendered a selective layer thickness within ±1 μm of the targeted thickness (i.e., the green bands in Figure 2.54). The middle location exhibited the least thickness variation, and the left and right locations were also fairly uniform. Larger thickness variations were observed for the far left and far right locations, which were near the edges of the membrane. It should be noted that after the membrane is rolled into a spiral-wound membrane module, the far left and far right regions will be covered by glue lines. Therefore, the module performance should not be affected by the coating near the edges.

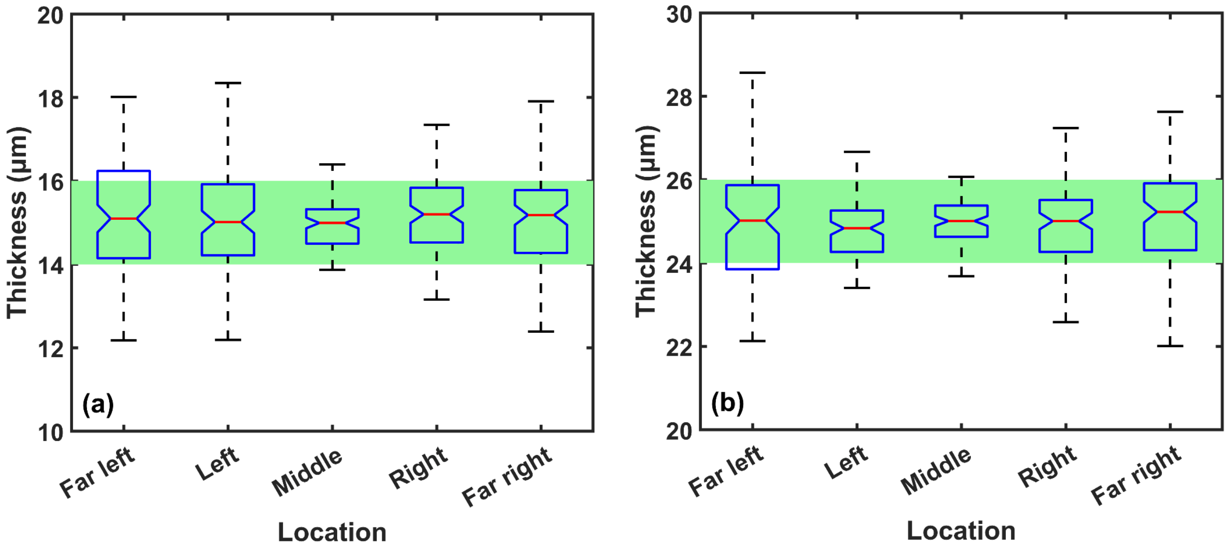

Figure 2.56. Thicknesses of the selective layer on the far left, left, middle, right, and far right locations along the width direction for the scale-up membranes: (a) FTM2 and (b) FTM1. The green bands represent the region within ±1 μm of the targeted thickness.

CO_2/H_2 Separation Performance

Membrane stamps were taken from the scale-up membranes and the CO_2/H_2 separation performances were tested at 107°C, a feed pressure of 35 bar, and a permeate pressure of 1.1 bar. As shown in Figure 2.55, the membrane samples tailored for the feed inlet (FTM2) exhibited an average CO_2 permeance of 312±12 GPU and a CO_2/H_2 selectivity of 126±6. The membrane samples tailored for the retentate outlet (FTM1) showed a CO_2 permeance of 217±17 GPU and a CO_2/H_2 selectivity of 265±7. The deviations were less than 5% except those of the CO_2 permeance of FTM1 samples tailored for the retentate outlet. The transport results were on par with the membranes synthesized in lab scale.

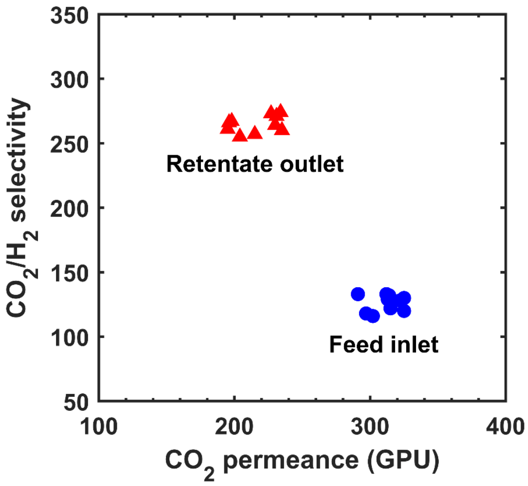

Figure 2.57. CO_2/H_2 separation results of the membranes tailored for feed inlet (FTM2) and retentate outlet (FTM1).

Modeling of Facilitated Transport Feature

The FTM2 and FTM1 scale-up membranes were also tested at CO_2 fugacities in the range of 0–14 bar. The measured CO_2 permeances are shown in Figure 2.56. The concentration dependence of CO_2 permeance on the gas composition is described by a homogeneous reactive diffusion model developed in our previous work for amine-containing membranes [36]:

$$\frac{P_i}{\ell} = \frac{P_i^0}{\ell}\left[1 + \eta_i\left(\sqrt{1 + \frac{f_i^*}{f_i^h}} - 1\right)\right] \tag{3}$$

where P_i^0/ℓ is the permeance of CO_2 due to the solution-diffusion mechanism, η_i represents the relative contribution from the facilitated transport, and f_i^* is the onset fugacity for carrier saturation. Eq. (3) is valid if the reaction timescale is much smaller than the diffusion timescale (i.e., a Damköhler number $\mathrm{Da} \gg 1$), by which an asymptotic regime exists and reaction equilibrium can be assumed throughout the membrane [37]. This requirement is generally satisfied for CO_2/H_2 separation facilitated transport membranes since the membrane thicknesses are often a few microns [23,38-40] and the large characteristic length guarantees a large diffusion timescale [41-43]. Apparently, $P_i/\ell \to P_i^0/\ell$ if $f_i^h \gg f_i^*$, and the facilitated transport of species i (CO_2) diminishes when the carriers are fully saturated, i.e., all reacted.

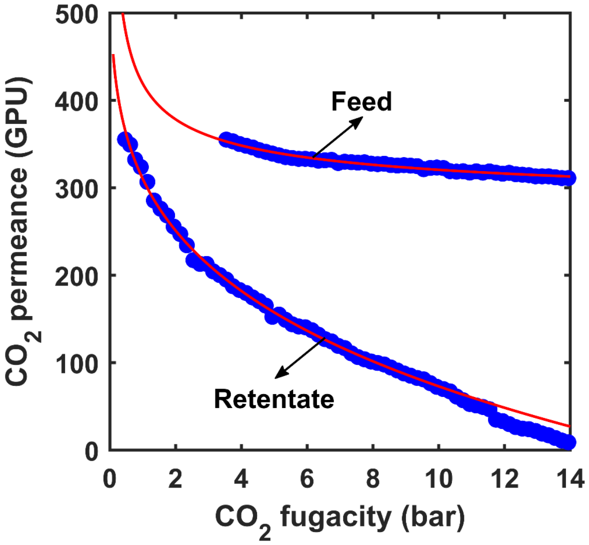

Figure 2.58. Dependence of CO_2 permeance on the CO_2 fugacity for the membranes tailored for the feed inlet and retentate outlet. The red solid lines are the best fits based on Eq. (1).

As seen in Figure 2.56, the facilitated transport model agrees reasonably well with the experimental data. Eq. (3) predicts the carrier saturation behavior of the FTM, where the CO_2 permeance reduces with increasing CO_2 fugacity. The initial non-linear decrease of CO_2 permeance indicates a consumption of free amine carriers in the membrane [44,45]. When all the amine carriers have reacted with CO_2, a transition to a flux plateau is observed, where the permeance reduces linearly as the CO_2 fugacity increases. The fitting parameters are listed in

Table 2.7. In this table, the ideal selectivity between a reactive gaseous species i (e.g., CO_2) and an inert species j (e.g., H_2) is defined as:

$$\alpha_{ij} = \alpha_{ij}^0 \left[1 + \eta_i \left(\sqrt{1 + \frac{f_i^*}{f_i^h}} - 1 \right) \right] \tag{4}$$

where $\alpha_{ij}^0 = P_i^0 / P_j^0$ is the ideal selectivity contributed by the solution-diffusion mechanism. This simplified model is used to describe the dependence of CO_2 permeance on the feed CO_2 fugacity in the techno-economic modeling. Unless otherwise specified, the FTM1 FTM is used in the sensitivity study, which will be discussed in Section 2.1.13.

Table 2.7. Fitting parameters for the carrier saturation behaviors of Types I and II membranes.

Type	Gas	P_i^0/ℓ (GPU†)	η_i	f_i^* (bar)	$\alpha_{CO_2/i}^0$
FTM2	CO_2	300	0.5	5	–
	H_2	2	0	–	150
	H_2O	300	0	–	1
	H_2S	900	0	–	0.33
FTM1	CO_2	50	0.5	10	–
	H_2	1	0	–	50
	H_2O	50	0	–	1
	H_2S	150	0	–	0.33

2.1.9 Task 9 – Prototype Membrane Module Fabrication

Summary

- Three 800-cm^2 spiral-wound (SW) membrane module was fabricated with the scale-up membrane containing the hydroxyethyl moiety for the feed inlet (FTM2). In addition, six 1600-cm^2 SW membrane module was fabricated from the scale-up membrane containing the sterically hindered amine for the retentate outlet (FTM1).

Spiral-Wound Module Design

The fabrication steps of the SW membrane element are illustrated in Figure 2.57.

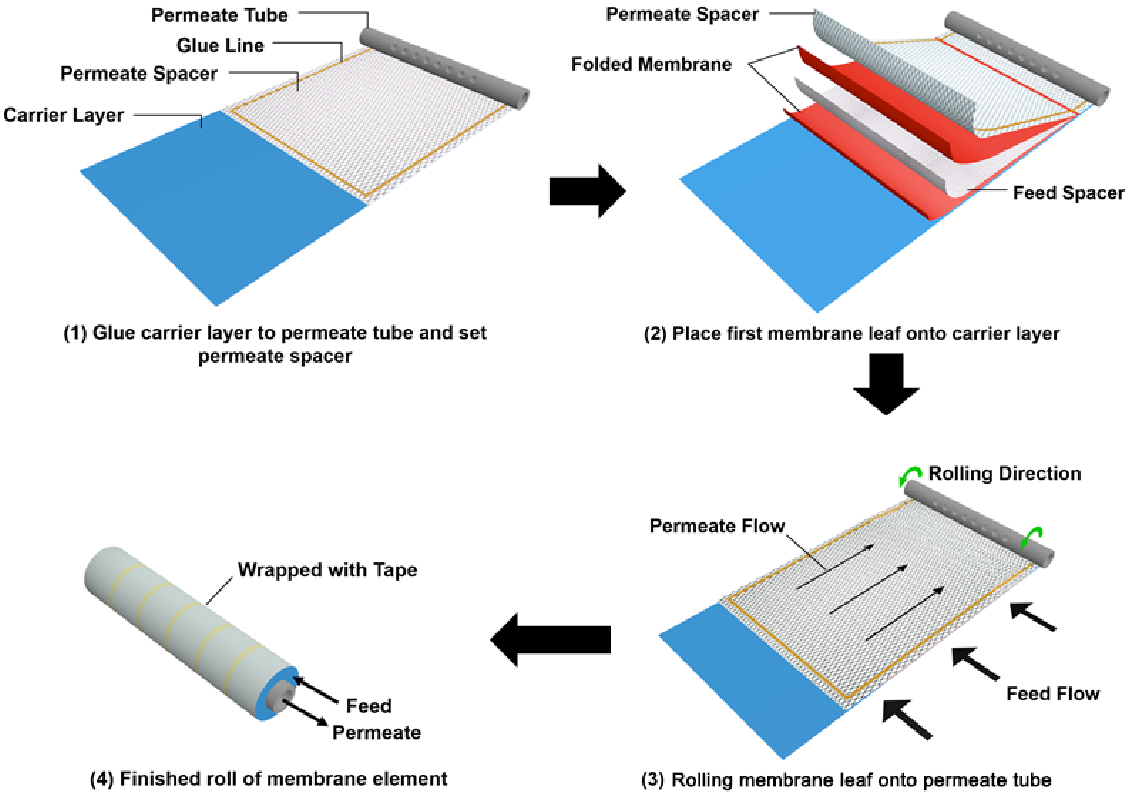

Figure 2.59. Procedure of single-leaf SW membrane element fabrication.

(1) The carrier layer is a 14″-wide non-woven fabric sheet to support the membrane leaf that will be placed on top. A single membrane leaf is used in the element. The carrier layer is laid out on a platform and attached to a stainless-steel permeate tube (ID 1.0″, OD 1.5″, length 16″), which has one line of permeate holes (diameter: 0.5″) drilled on the side. Since a tension can be applied on the carrier layer during the rolling to achieve a tight roll, the layer needs to be attached to the permeate tube firmly. Hence, the layer is glued to the permeate tube. Next, a permeate spacer is inserted between the carrier layer and the permeate tube, and an epoxy glue line is placed manually using a glue applicator along the three sides of the permeate spacer. The glue line is kept 0.5″ away from the edge to leave enough room for the glue to spread.

(2) Next, a piece of membrane of 14″ × 9″ is folded in half to form a 14″ × 4.5″ envelope, with the selective layer of the membrane facing inward, and a feed spacer is sandwiched in between. Glue is applied along the inner side of the fold to seal any possible damage resulting from the folding, and a permeate spacer is put above the folded membrane. The folded membrane, with the feed and permeate spacers, is treated as a single membrane leaf. For the SW element with 1600 cm^2 area, the length of the membrane is increased to 18″.

(3) Subsequently, the rolling of the element, in the direction of the curved arrows, is done using an in-house rolling machine. The permeate tube is fixed firmly between a chuck and a tailstock so that it does not slip when the chuck rotates at 2.5 rpm. As the rotation begins, the carrier layer is pulled away from the permeate tube to supply a tension, which is sustained throughout the rolling process. After the leaf is in the roll, certain extra length of the carrier layer is rolled onto the

element to maintain the tightness of the roll. The diameter of the fabricated SW element is designed to be 2.5″.

(4) Finally, the roll is sat for overnight at room temperature for the glue to set. Two sets of straight arrows in Figure 2.57 (3) and (4) illustrate the idealized crossflow pattern during the module's operation: as the feed flows in parallel to the permeate tube, the permeate moves radially towards the tube on the other side of the membrane.

Figure 2.58 (a) shows the photo of one of the three 800-cm^2 SW elements that were successfully fabricated using the scale-up membrane tailored for the feed inlet (FTM2 membrane). The element contained one membrane leaf of 14″ × 4.5″, resulting in a membrane area of 800 m^2. The diameter of the fabricated SW element was 2.5″. The membrane element also contained a thermally stable fiber-reinforced plastic (FRP) outer layer for the high-pressure operation. Carbon fiber (black color) was chosen as the FRP material. By using a new FRP wrapping machine, the wrapping started from one side of the element and went back and forth 5 times as one cycle, resulting in a 75-mil thick of FRP layer.

Six 1600-cm^2 SW module were also fabricated with the scale-up membrane tailored for the retentate outlet (FTM1 membrane); the photo of one of the modules is shown in Figure 2.58 (b). Due to the short membrane leaf lengths of 4.5″ and 9″ for the 800-cm^2 and 1600-cm^2 elements, respectively, the two photos in Figure 2.58 (a) and (b) look similar. The SW membrane element was eventually loaded in the stainless-steel housing to become the membrane module as shown in Figure 2.58 (c).

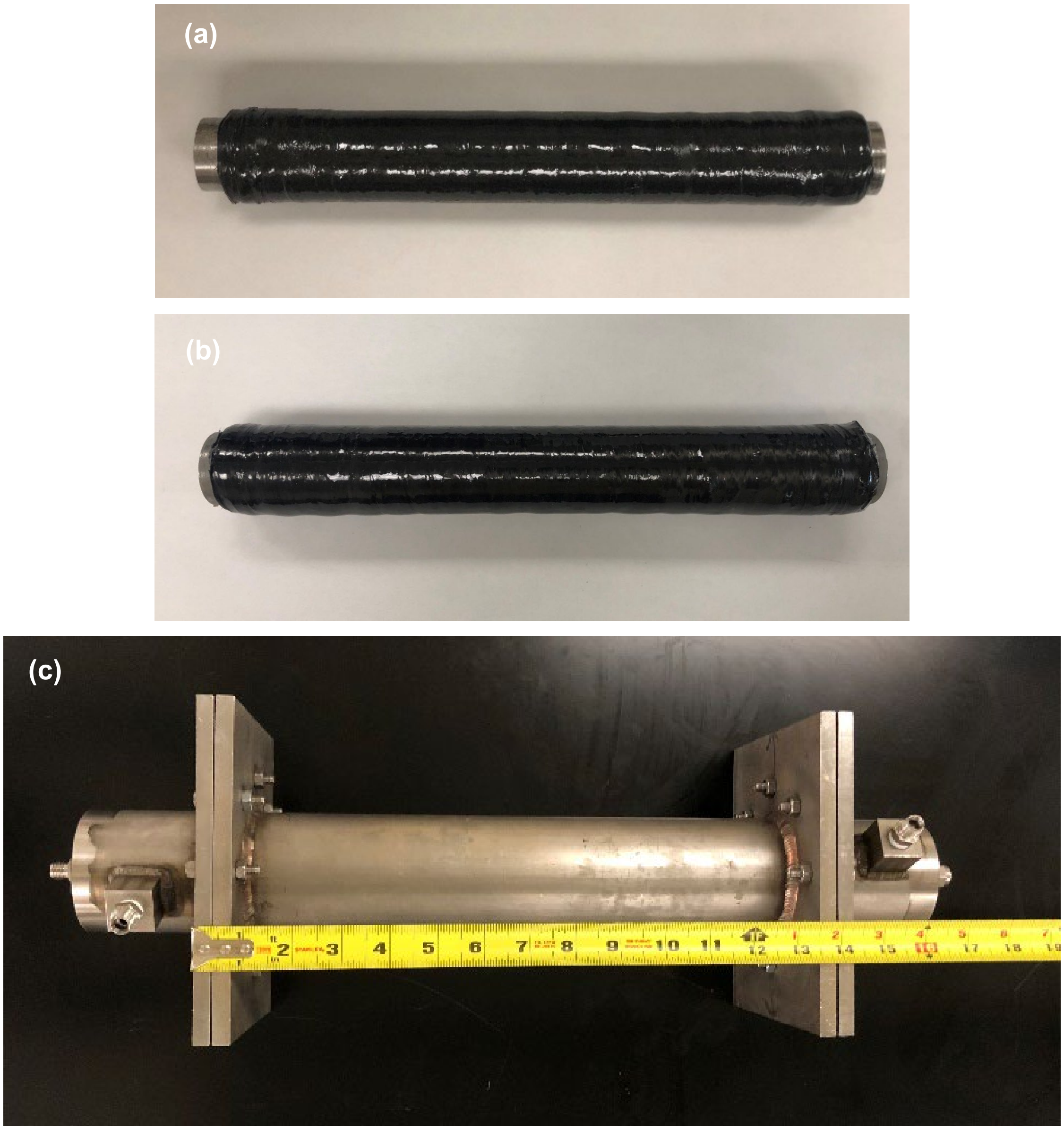

Figure 2.60. Photos of (a) 800 cm^2 prototype SW membrane element, (b) 1600 cm^2 prototype SW membrane element, and (c) prototype SW membrane module.

2.1.10 Task 10 – Prototype Membrane Module Testing

Summary

- The 800 cm^2 SW module containing the FTM2 membrane was tested at 107°C and 35 bar feed pressure with a simulated syngas.
- The 1600 cm^2 SW module containing the FTM1 membrane was also tested at the same conditions.

- By altering the syngas flow rate, the CO_2/H_2 separation performances of both SW modules were studied and compared with the modeling results. A reasonably good agreement was obtained.

CO_2/H_2 Separation Performances of Individual Modules

The 800 cm^2 SW module containing the FTM2 membrane tailored for the feed inlet was tested at 107°C and 35 bar feed pressure. The 1600 cm^2 SW module containing the FTM1 membrane tailored for the retentate outlet was also tested at the same conditions. By altering the syngas flow rate, the CO_2 recovery, CO_2 purity, and H_2 recovery were measured, and the results are shown in Figure 2.59. As shown, the CO_2 purity and H_2 recovery reduced with increasing CO_2 recovery. At 90% CO_2 recovery, the FTM2 SW module exhibited a CO_2 purity of 98.0% and a H_2 recovery of 98.2%. For the FTM1 SW module, a CO_2 purity of 95.0% and a H_2 recovery of 97.1% were achieved at 90% CO_2 recovery. The experimental results were also compared with the theoretical predictions calculated by a crossflow model for multicomponent gas permeation, which is detailed in our recent publication [46]. Based on the crossflow model, the facilitated transport model reported in Section 2.1.8 was used to describe the CO_2/H_2 transport performances of the two types of membranes. As depicted in Figure 2.59, a reasonably good agreement was observed between the experimental and theoretical results. Therefore, the crossflow model was used for the process modeling in the TEA.

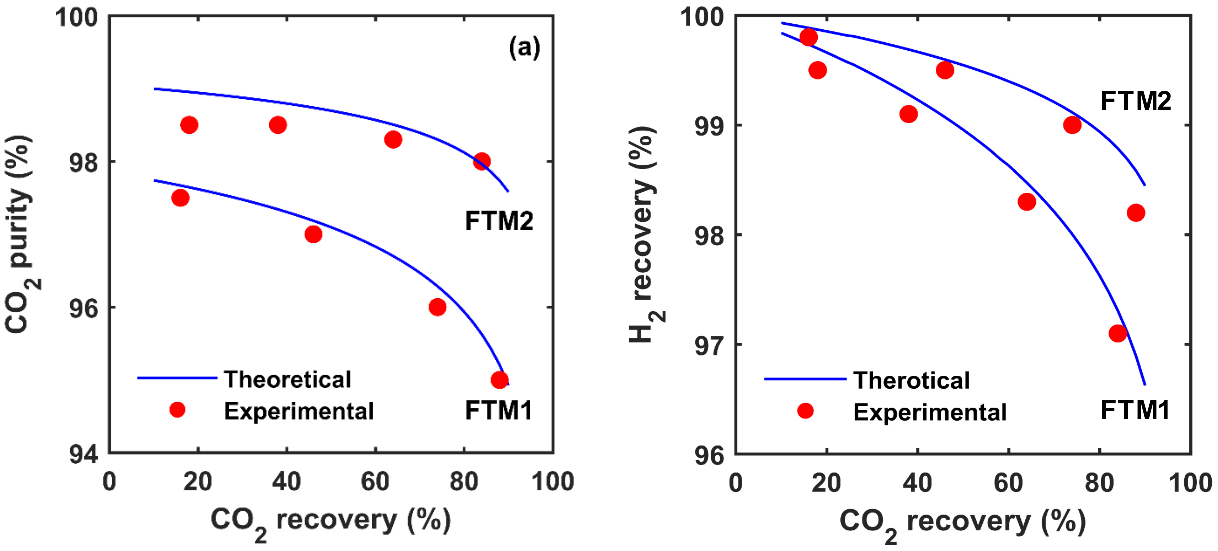

Figure 2.61. (a) CO_2 purities and (b) H_2 recoveries at different CO_2 recoveries for the SW modules containing the FTM1 and FTM2 membranes.

2.1.11 Task 11 – Parametric Testing with Prototype Modules in Series

Summary

- The FTM2 and FTM1 SW modules were connected in series to form a hybrid configuration of the two membrane types. By altering the syngas flow rate, the CO_2/H_2 separation performances of the module array were studied and compared with the modeling results. A reasonably good agreement was obtained.

- At the optimized conditions, the module array demonstrated a H_2 recovery of 99.3% at 90% CO_2 removal and a CO_2 purity of 95.2%.

<u>CO_2/H_2 Separation Performances of Hybrid Module Array</u>

The FTM2 and FTM1 SW modules were connected in series to form a hybrid configuration of the two membrane types, which was tested with a simulated syngas at 107°C and 35 bar feed pressure. By altering the syngas flow rate, the CO_2 recovery, CO_2 purity, and H_2 recovery were measured, and the results are shown in Figure 2.60. As shown, the CO_2 purity and H_2 recovery reduced with increasing CO_2 recovery. At 90% CO_2 recovery, the two SW modules in series exhibited a CO_2 purity of 95.2% and a H_2 recovery of 99.3%. The experimental results were also compared with the theoretical predictions calculated by a crossflow model for multicomponent gas permeation [46]. As depicted in Figure 2.60, a reasonably good agreement was observed between the experimental and theoretical results.

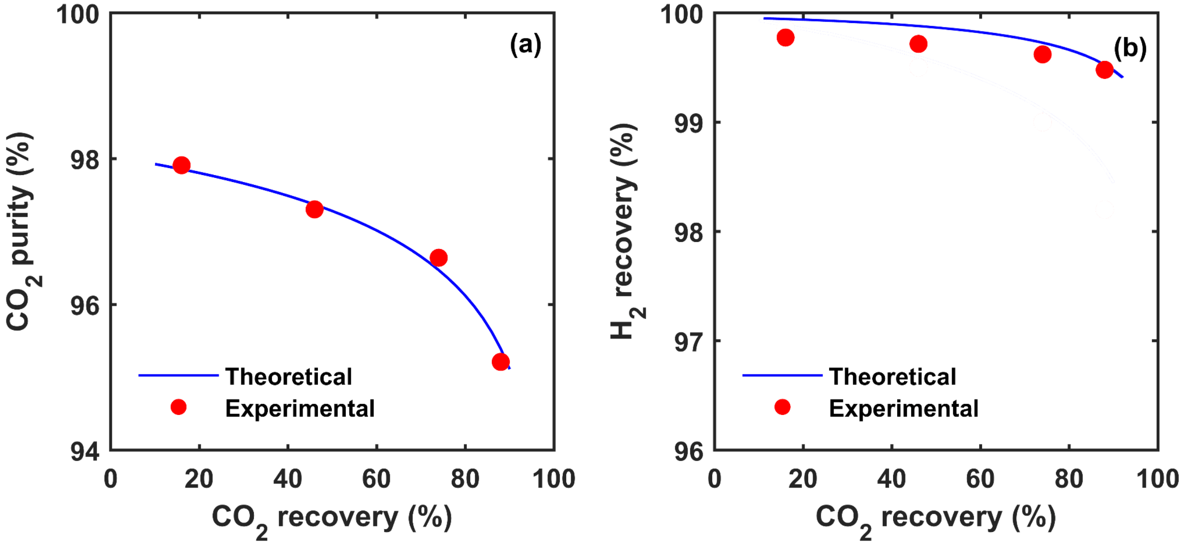

Figure 2.62. (a) CO_2 purities and (b) H_2 recoveries at different CO_2 recoveries for the two SW modules in series.

2.1.12 Task 12 – Continuous Steady Operation with Modules in Series

<u>Summary</u>

- The hybrid configuration of two membrane modules connected in series was tested with a simulated syngas for 200 hours, which demonstrated a stable CO_2/H_2 separation performance.

<u>Steady-State CO_2/H_2 Separation Performance</u>

The stability of the two SW membrane modules connected in series is shown in Figure 2.61. The solid lines represent the average results. Over the course of 200 h, the membrane modules connected in series showed an average CO_2 purity of 95.2% with a H_2 recovery of 99.3% and remained stable. Although a longer and more thorough test is needed, the 200-h stability has shed promising light on the following aspects. First, the mobile carriers possess a negligible volatility in the polymeric membrane, which minimizes the possibility of loss through volatility. Second, the membranes are mechanically stable under the high syngas pressure. Last, the polymer matrix is fully rubbery and not subject to a conformational relaxation, i.e., no physical aging is expected.

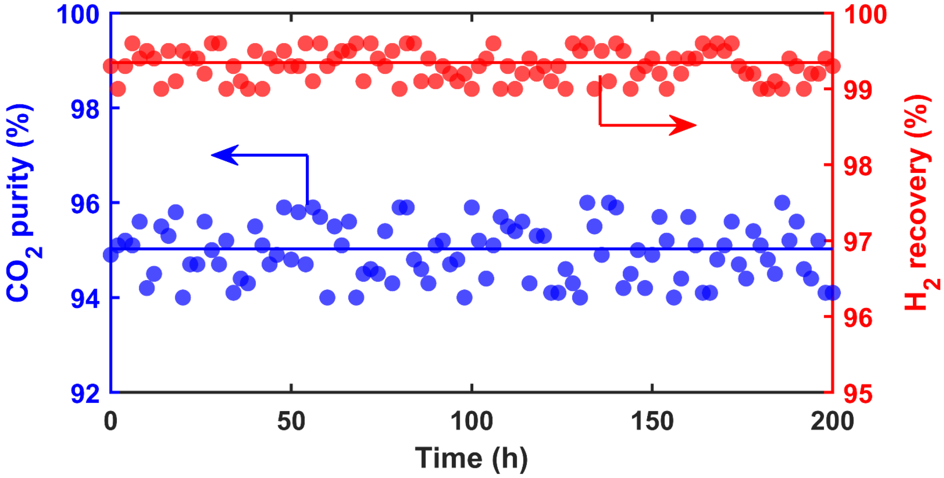

Figure 2.63. Stability of the two SW membrane modules connected in series. The solid lines represent the average results.

2.1.13 Task 13 – Final Updated Techno-Economic Analysis

Summary

- A sensitivity study was carried out to evaluate the technical and economic feasibility of the developed membranes.
- The single-stage Selexol process for the H_2S removal from the captured CO_2 can be replaced by a continuous membrane column. The best membrane developed in this project possesses a H_2S/CO_2 selectivity of 16.3, which leads to a low COE increase of 14.9%.
- The TEA has been updated based on the 2019 DOE Cost and Performance Baseline document (Revision 4), which results in a cost of electricity (COE) of \$124.4/MWh. This value corresponds to a COE increase of 15.3%, which is significantly lower, i.e., 54.5%, than the benchmark two-stage Selexol process (i.e., COE increase of 33.6%).
- The Final Techno-Economic Analysis Report has been submitted to DOE-NETL.

Minimum Selectivity for Non-Reactive Polymeric Membrane

The necessity of using a highly CO_2-selective membrane for the proposed single-stage membrane process is studied by calculating the CO_2 purities and the H_2 recoveries for CO_2 permeances ranging from 100 to 1000 GPU and CO_2/H_2 selectivities between 5 and 200. The membrane is assumed as non-reactive, and the η_i values are set to zero in Eq. (10). The feed and permeate pressures are 31.7 and 1.1 bar, respectively, and the CO_2 recovery is fixed at 90%. The results are shown in Figure 2.62.

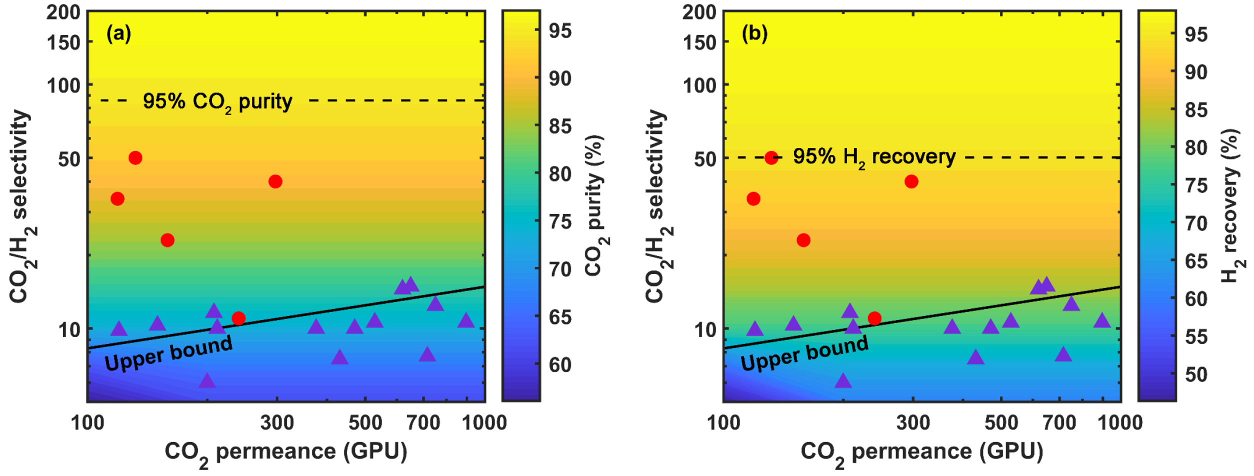

Figure 2.64. Effects of CO_2 permeance and CO_2/H_2 selectivity on (a) CO_2 purity and (b) H_2 recovery for a non-reactive polymeric membrane (i.e., $\eta_i = 0$) with p^h and p^l at 31.7 and 1.1 bar, respectively. The black line is the theoretical CO_2/H_2 upper bound at 25°C assuming a membrane thickness of 1 μm [47]. Symbols: polyethers (▲) and amine-containing FTMs (●) as summarized and reviewed by Han and Ho [48].

As shown in Figure 2.62 (a), a CO_2/H_2 selectivity greater than 85 is required to achieve >95% CO_2 purity. In order to put this requirement into perspective, the theoretical CO_2/H_2 upper bound for non-reactive rubbery polymers at 25°C [47] is plotted in Figure 2.62 (a) assuming a membrane thickness of 1 μm. Also plotted are the CO_2/H_2 transport results of selected amine-containing FTMs and polyethers as reviewed in our recent publication [48]. As seen, the non-reactive polymers generally exhibit a CO_2/H_2 selectivity less than 15, which at most renders a CO_2 purity of ca. 80%. The captured CO_2 needs to be further enriched by another membrane [49] or cryogenic distillation [50] to achieve 95% purity. In addition, these non-reactive membranes are usually operated at –20 to 30°C [51]; the CO_2/H_2 selectivity is expected to reduce with increasing temperature due to the weakened CO_2/H_2 solubility selectivity [52]. Therefore, the heat duty to cool the shifted syngas from 240°C could be prohibitive. Contrarily, a higher CO_2/H_2 selectivity of 50 can be achieved by certain amine-containing FTMs, which leads to a CO_2 purity of ca. 90%. These FTMs can also be operated at a temperature higher than 100°C, and the mitigated syngas cooling can be conducted by more synergy-efficient methods such as thermal expansion rather than direct contact cooling [24].

A similar trend is observed for the H_2 recovery as shown in Figure 2.62 (b). A CO_2/H_2 selectivity of 50 is required for 95% H_2 recovery, which is within the reach of amine-containing FTMs. The non-reactive polymeric membranes can only recover 75–80% of H_2 by a single membrane stage. Compared to the two-stage Selexol process as reported in the Baseline Document, however, it can retain 99.7% of the H_2 at 90% CO_2 recovery [24]. Further analysis indicates that a CO_2/H_2 selectivity of 300 is needed for the non-reactive membrane process to achieve >99% H_2 recovery.

Minimum Selectivity for FTM

In order to further analyze how the CO_2/H_2 selectivity affects the H_2 recovery, the changes of H_2 flux from the feed inlet to the retentate outlet are calculated for two non-reactive membranes with CO_2/H_2 selectivities of 50 and 300, respectively. The feed and permeate pressures are fixed at 31.7 and 1.1 bar, respectively, and the CO_2 recovery is varied between 30% and 90%. As illustrated in Figure 2.63 (a), at 30% CO_2 recovery, little difference is observed between the H_2 fluxes by using the moderately and highly selective membranes. Such a difference is more pronounced at a greater CO_2 recovery, where the H_2 concentration increases considerably near the retentate outlet due to the CO_2 separation. However, even at 90% CO_2 recovery, the moderately and highly selective membranes exhibit similar H_2 fluxes from the feed inlet to ca. 30% of the total membrane area. A high CO_2/H_2 selectivity is only required in the proximity of the retentate outlet in order to reduce the H_2 permeation.

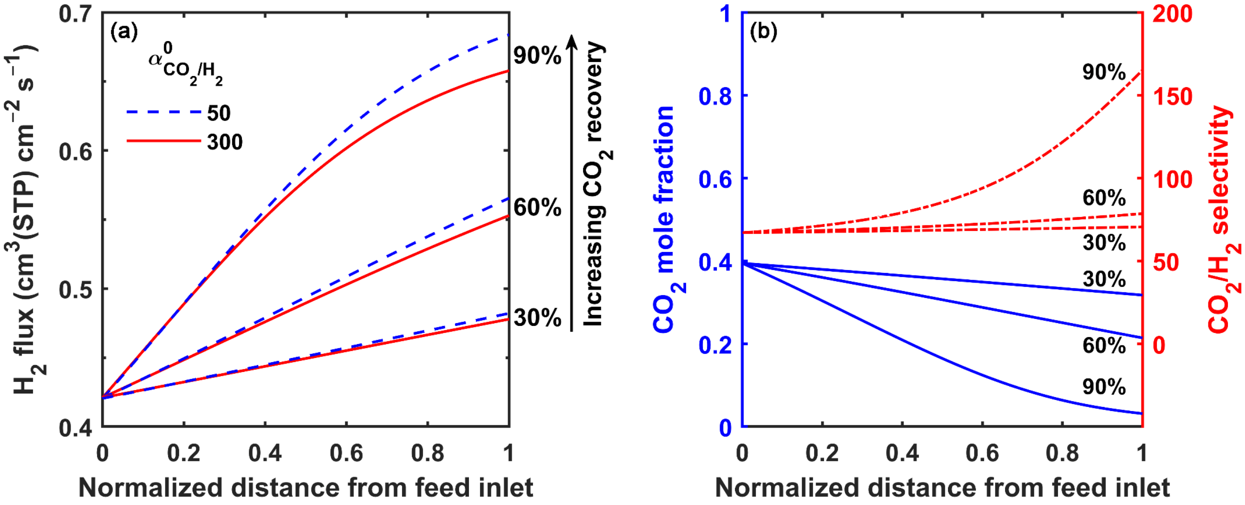

Figure 2.65. (a) Changes of H_2 flux at CO_2 recoveries of 30%, 60%, and 90% for non-reactive membranes (i.e., $\eta_i = 0$) with CO_2/H_2 selectivities (α) of 50 and 300; (b) Changes of feed CO_2 mole fraction (—) and CO_2/H_2 selectivity (----) at CO_2 recoveries of 30%, 60%, and 90% for a FTM with $\alpha^0_{CO_2/H_2}$ = 50, η_{CO_2} = 0.5, and $f^*_{CO_2}$ = 10 bar. p^h = 31.7 bar and p^l = 1.1 bar.

Conceptually, an uprising CO_2/H_2 selectivity could be achieved by a FTM if the onset fugacity for carrier saturation (i.e., $f^*_{CO_2}$) is larger than the CO_2 fugacity at the retentate outlet (i.e., $f_{CO_2}\big|_{A=A_0}$). Such an effect is demonstrated in Figure 2.63 (b) for an exemplary FTM with $\alpha^0_{CO_2/H_2}$ = 50, η_{CO_2} = 0.5, and $f^*_{CO_2}$ = 10 bar for 30%, 60%, and 90% CO_2 recoveries. The feed and permeate pressures are fixed at 31.7 and 1.1 bar, respectively. With increasing CO_2 recovery, the CO_2 mole fraction on the feed side reduces considerably upon the CO_2 removal. The reduced CO_2 content mitigates the carrier saturation and leads to a significant increase in the CO_2 permeance from the feed inlet to the retentate outlet. As the H_2 permeation follows the solution-diffusion mechanism and its permeance does not depend strongly on the gas composition, the improved CO_2 permeance can result in an uprising CO_2/H_2 selectivity upon the CO_2 removal. For the exemplary FTM as shown in Figure 2.63 (b), the CO_2/H_2 selectivity is more than doubled from the feed inlet to the retentate outlet at 90% CO_2 recovery.

Aside from the CO_2 recovery, the change of CO_2/H_2 selectivity is also affected by the intrinsic facilitated transport properties of the FTM. In order to demonstrate the influence of facilitated transport feature on the separation performance, the captured CO_2 purities and H_2 recoveries are calculated for a FTM with $\eta_{CO_2} = 0.5$. The CO_2/H_2 selectivity at full saturation (i.e., $\alpha^0_{CO_2/H_2}$) is varied in the range of 50–300 and the onset fugacity for carrier saturation $f^*_{CO_2}$ is changed between 0 and 10 bar. The feed and permeate pressures are 31.7 and 1.1 bar, respectively, and the CO_2 recovery is fixed at 90%. As shown in Figure 2.64 (a), for a given $\alpha^0_{CO_2/H_2}$, the CO_2 purity increases with increasing $f^*_{CO_2}$ value. Since the fraction of membrane under carrier saturation reduces with increasing $f^*_{CO_2}$, the mitigated carrier saturation improves the overall CO_2 purity. For a $f^*_{CO_2}$ value of 6 bar, a $\alpha^0_{CO_2/H_2}$ value of only 60 is required to achieve 95% CO_2 purity. The $\alpha^0_{CO_2/H_2}$ value can be further reduced to 50 if $f^*_{CO_2}$ is increased to 10 bar. Recall that a CO_2/H_2 selectivity of 85 is needed for a non-reactive membrane to reach the same degree of CO_2 purity. Therefore, the facilitated transport feature relaxes the requirement on the membrane selectivity.

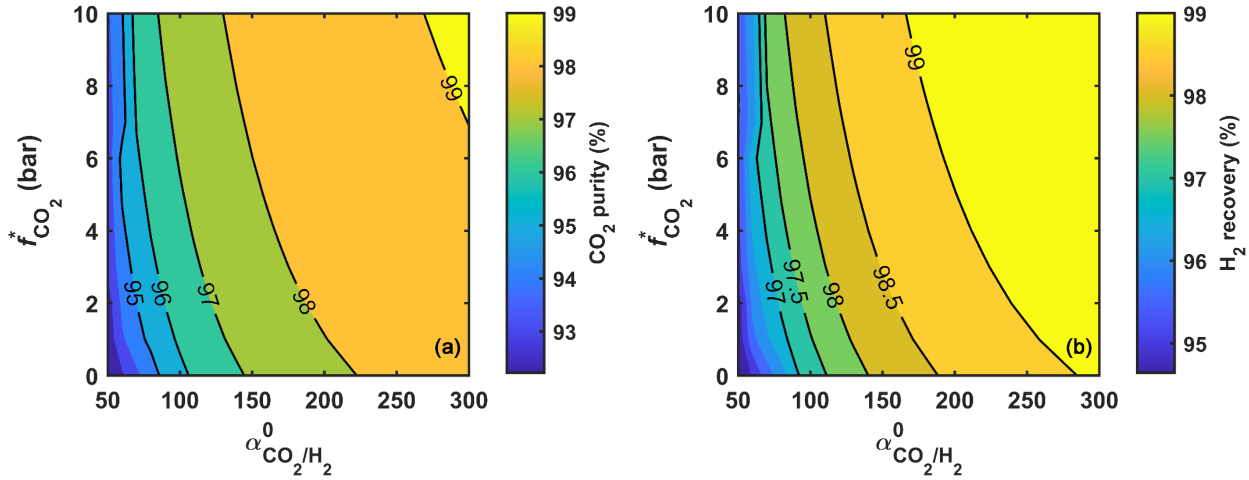

Figure 2.66. Effects of CO_2/H_2 selectivity at full saturation ($\alpha^0_{CO_2/H_2}$) and onset saturation fugacity ($f^*_{CO_2}$) on (a) CO_2 purity and (b) H_2 recovery for a FTM with $\eta_{CO_2} = 0.5$, $p^h = 31.7$ bar, and $p^l = 1.1$ bar.

Unsurprisingly, the facilitated transport feature also benefits the H_2 recovery. As shown in Figure 2.64 (b), a $\alpha^0_{CO_2/H_2}$ value of 160 is sufficient for a H_2 recovery of 99% if the $f^*_{CO_2}$ is equal to 10 bar. Compared with the non-reactive membranes, the CO_2/H_2 selectivity requirement is also greatly relaxed. At first glance, the improved H_2 recovery might be attributed to the uprising CO_2/H_2 selectivity and thereby a lower H_2 flux. However, as shown in Figure 2.65 (a), the use of FTM ($\alpha^0_{CO_2/H_2} = 50$, $\eta_{CO_2} = 0.5$, and $f^*_{CO_2} = 10$ bar) actually results in an overall higher H_2 flux compared to the non-reactive membranes with CO_2/H_2 selectivities of 50 and 300, especially in the proximity of retentate outlet. In this case, the higher H_2 recovery renders a higher H_2 concentration on the feed side, thus the higher H_2 flux. In order to understand the cause of the improved H_2 recovery, the membrane areas for 90% CO_2 recovery with various η_{CO_2} and $f^*_{CO_2}$ values are calculated, and the results are shown in Figure 2.65 (b). Here, the dimensionless membrane area is plotted, which has been detailed in our previous publication [36]. As seen, an appreciable reduction in the membrane area is observed at large η_{CO_2} and $f^*_{CO_2}$ values, which is a consequence of the increasing CO_2 permeance upon bulk CO_2 removal. For the FTM with η_{CO_2} = 0.5 and $f^*_{CO_2}$ = 10 bar, the membrane area is reduced by ca. 25% compared to the non-reactive membrane with $\eta_{CO_2} = 0$. Therefore, the reduced membrane area outweighs the increased H_2 flux, and thereby the lower H_2 permeation rate with the facilitated transport feature.

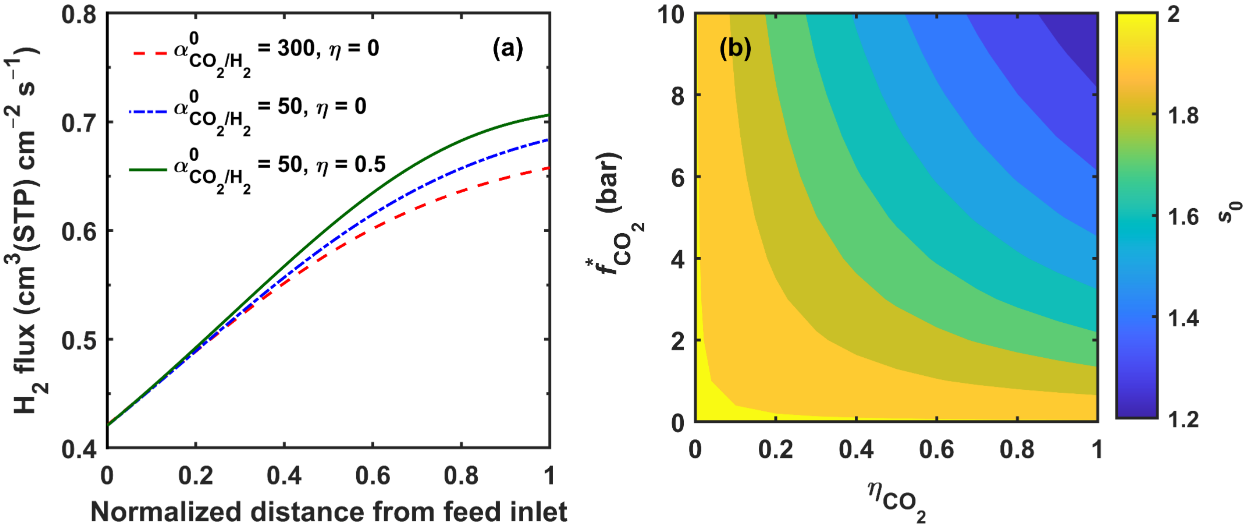

Figure 2.67. (a) Changes of H_2 flux for two non-reactive polymeric membranes and a FTM with $\alpha^0_{CO_2/H_2}$ = 50, η_{CO_2} = 0.5, and $f^*_{CO_2}$ = 10 bar. (b) Effect of mitigated carrier saturation on dimensionless membrane area (s) for a FTM with $\alpha^0_{CO_2/H_2}$ = 50. p^h = 31.7 bar, p^l = 1.1 bar, and CO_2 recovery = 90%.

Effect of Feed Pressure

The sensitivity of process economics with respect to the feed pressure is studied for a FTM with a $\alpha^0_{CO_2/H_2}$ value of 50 and a η_{CO_2} value of 0.5. The $f^*_{CO_2}$ values are varied between 1 and 20 bar. The permeate pressure is 1.1 bar, and the CO_2 recovery is fixed at 90%. As shown in Figure 2.66 (a), the COE initially reduces with increasing feed pressure, but an excessively high feed pressure affects the process economics adversely. As abovementioned, the feed pressure to the membrane is controlled by expanding the shifted syngas via EX-01; the CO_2-lean retentate is recompressed to 31.7 bar by CP-01 for the combustion turbine if the feed pressure is lower than this value. In addition, if the thermal expansion cannot cool the syngas to 110°C, an additional syngas cooler HX-01 is used to condition the syngas for the membrane separation. The initial reduction in the COE is attributed to the reduced membrane cost as well as the reduced capital costs associated with EX-01 and CP-01 as illustrated in Figure 2.66 (b). However, the heat duty of HX-01 increases significantly since the thermal expansion cannot cool the syngas to an appreciable extent at a high feed pressure to the membrane. For instance, at a feed pressure of 50 bar, the membrane cost is reduced to 5.9 million dollars, but the cost of the syngas cooler is prohibitively high (27.9 million dollars). The trade-off between the membrane cost and syngas cooling cost results in an optimal feed pressure in the range of 30–40 bar. The actual optimal feed pressure depends on the facilitated transport feature of the membrane. For a FTM with a higher onset fugacity of carrier saturation $f_{\mathrm{CO_2}}^*$, the membrane is less prone to carrier saturation at a higher feed pressure. In this case, the increased transmembrane driving force is not compromised by the reduced CO_2 permeance. Therefore, the optimal feed pressure increases with increasing $f_{\mathrm{CO_2}}^*$ value.

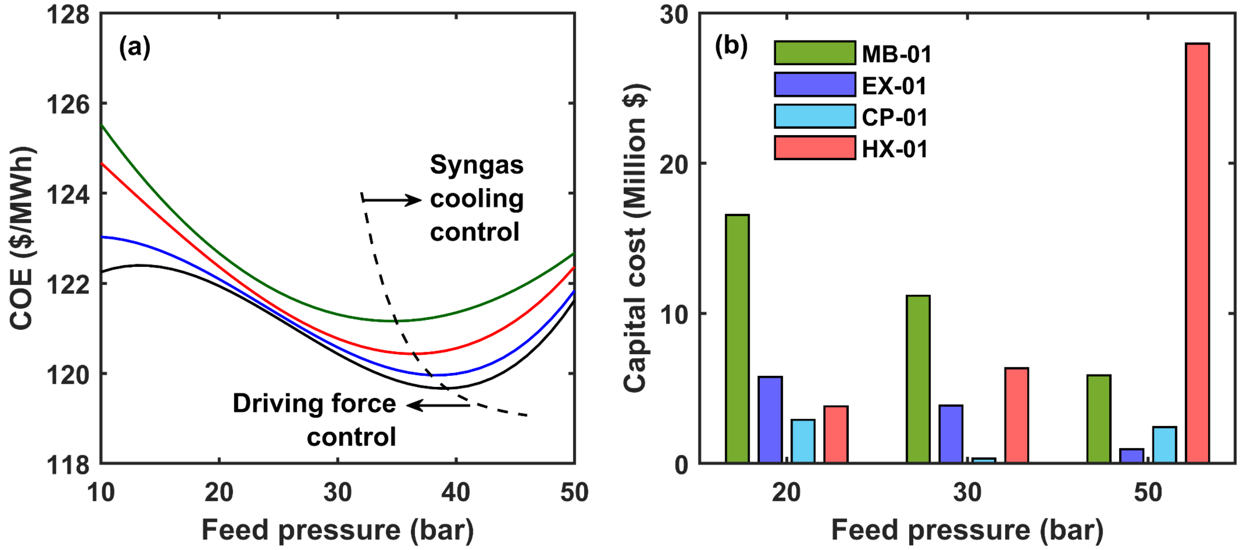

Figure 2.68. (a) Effect of feed pressure on COE for $f_{\mathrm{CO_2}}^*$ values of 1, 5, 10, and 20 bar (from top to bottom); $\alpha_{\mathrm{CO_2/H_2}}^0 = 50$, $\eta_{\mathrm{CO_2}} = 0.5$, $p^l = 1.1$ bar, and CO_2 recovery = 90%. (b) Capital costs of membrane (MB-01), turboexpander (EX-01), syngas re-compressor (CP-01), and syngas cooler (HX-01) at $f_{\mathrm{CO_2}}^* = 10$ bar.

Effect of Permeate Pressure

The effect of permeate pressure is studied for a FTM with a $\alpha_{\mathrm{CO_2/H_2}}^0$ value of 50, a $\eta_{\mathrm{CO_2}}$ value of 0.5, and a $f_{\mathrm{CO_2}}^*$ value of 10 bar. The feed pressure is fixed at 31.7 bar, while the permeate pressure is varied in the range of 1.1–4 bar. As shown in Figure 2.67, a higher permeate pressure results in a lower energy consumption for the CO_2 compression (i.e., the total energy consumption of MSC-01 and MSC-02 shown in Figure 2.28). However, the reduced transmembrane driving force also renders a larger membrane area. This trade-off leads to the optimal permeate pressure at 2 bar. Particularly, the COE is less sensitive to the permeate pressure when it is between 1.1 and 2 bar. For a permeate pressure higher than 3 bar, the COE increases considerably due to the larger membrane area.

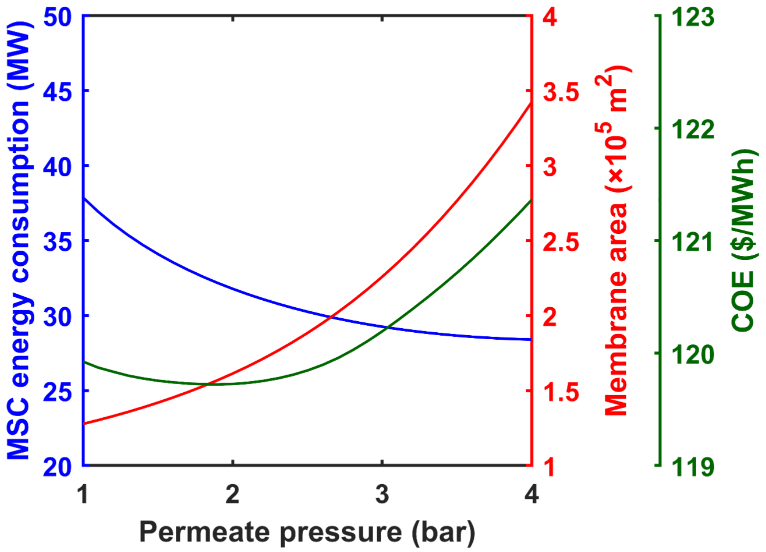

Figure 2.69. Effects of permeate pressure on multistage CO_2 compression (MSC) energy consumption, membrane area, and COE. A FTM with $\eta_{\mathrm{CO_2}}$ = 0.5, $\alpha^0_{\mathrm{CO_2/H_2}}$ = 50, and $f^*_{\mathrm{CO_2}}$ = 10 bar is used. p^h = 31.7 bar and CO_2 recovery = 90%.

Effect of CO_2 Permeance

The effect of CO_2 permeance ($P^0_{\mathrm{CO_2}}/\ell$) on the process economics is studied for (1) a FTM with $\eta_{\mathrm{CO_2}}$ = 0.5, $\alpha^0_{\mathrm{CO_2/H_2}}$ = 50, and $f^*_{\mathrm{CO_2}}$ = 10 bar and (2) a non-reactive membrane with $\eta_{\mathrm{CO_2}}$ = 0 and $\alpha^0_{\mathrm{CO_2/H_2}}$ = 50. For the FTM as shown in Figure 2.68 (a), the membrane area reduces with increasing CO_2 permeance, thereby a reducing COE increase. For instance, the membrane area reduces from 1.8×10^5 to 8.9×10^4 m^2 if the $P^0_{\mathrm{CO_2}}/\ell$ value increases from 50 to 100 GPU. Accordingly, the COE reduces from $120.2/MWh to $119.5/MWh. However, the CO_2 permeance has little effect on the COE when it is greater than 200 GPU. In this case, the membrane cost is outweighed by those of the rotating equipment and heat exchangers. Therefore, a more permeable membrane is not beneficial for the process economics. With a sufficiently high CO_2 permeance of 250 GPU, the COE approaches to $118.9/MWh, which corresponds to a 15.9% COE increase compared to the baseline case without carbon capture (i.e., Case B5A in the Baseline Document (Rev. 2b) [24]). It should be noted that a higher CO_2 permeance might reduce the footprint of the capture system, which could be ideal for the integration of membrane capture into an IGCC plant.

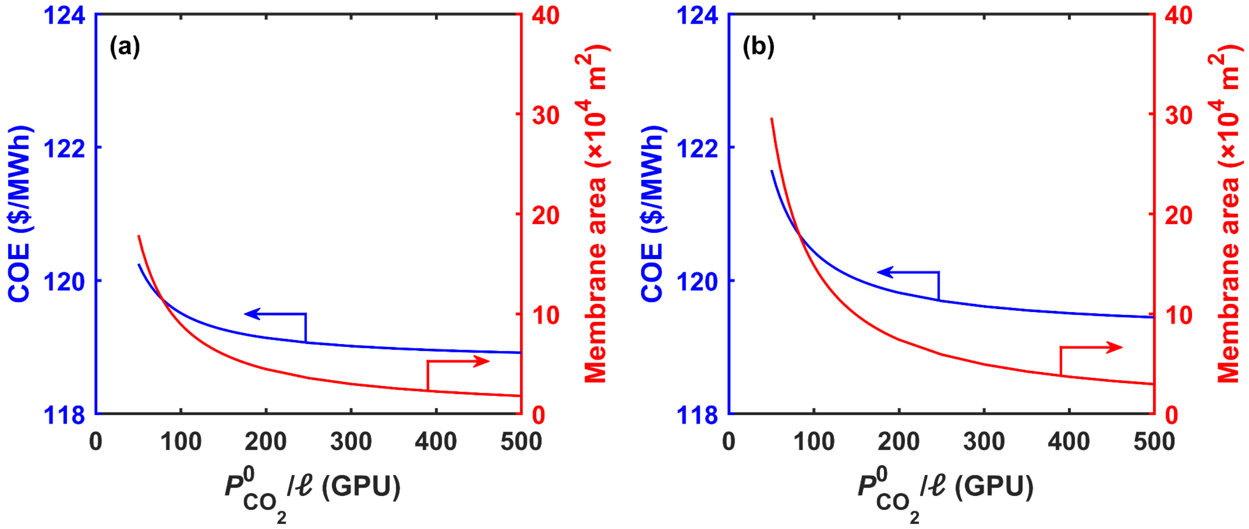

Figure 2.70. Effects of CO2 permeance $P^0_{CO_2}/\ell$ on COE and membrane area for (a) a FTM with η_{CO_2} = 0.5, $\alpha^0_{CO_2/H_2}$ = 50, and $f^*_{CO_2}$ = 10 bar and (b) a non-reactive membrane with η_{CO_2} = 0 and $\alpha^0_{CO_2/H_2}$ = 50. p^h = 31.7 bar, p^l = 1.1 bar, and CO2 recovery = 90%.

In comparison, as shown in Figure 2.68 (b), the non-reactive membrane requires a CO2 permeance as high as 400 GPU to achieve a membrane area similar to that of the FTM. The COE also shows a stronger dependence on the CO2 permeance. As discussed in Figure 2.65, a FTM exhibits an uprising CO2 permeance upon CO2 removal, which leads to a smaller membrane area relative to its non-reactive membrane counterpart. Even at a CO2 permeance of 500 GPU, the process using a non-reactive membrane exhibits a high COE of $119.4/MWh (16.4% COE increase), which is still higher than that for the FTM with a CO2 permeance of 250 GPU.

Cost of Hybrid Membrane Configuration

The hybrid membrane configuration has been discussed in Section 2.1.4. Specifically, the highest H2 recovery can be achieved by using ca. 35% FTM2 with the remaining using the FTM1. Figure 2.69 compares the COE values of the GEE gasifier without carbon capture (i.e., Case B5A in the Baseline Document [24]), the two-stage Selexol process (i.e., Case B5B in the Baseline Document [24]), and the single-stage membrane processes using the FTM1 alone, using the FTM2 alone, and using the hybrid membrane configuration as illustrated in Figure 2.29, i.e., 35% FTM2 and 65% FTM1. For all the three membrane arrangements discussed herein, the single-stage membrane process shows a considerably lower COE than that of the two-stage Selexol process. In particular, the hybrid membrane configuration renders a COE of $118.4/MWh, which corresponds to a 15.4% COE increase compared to the no capture scenario. Along with a H2 recovery of 99.4%, the single-stage membrane process with hybrid membrane configuration proves to be a more economical alternative to the Selexol process.

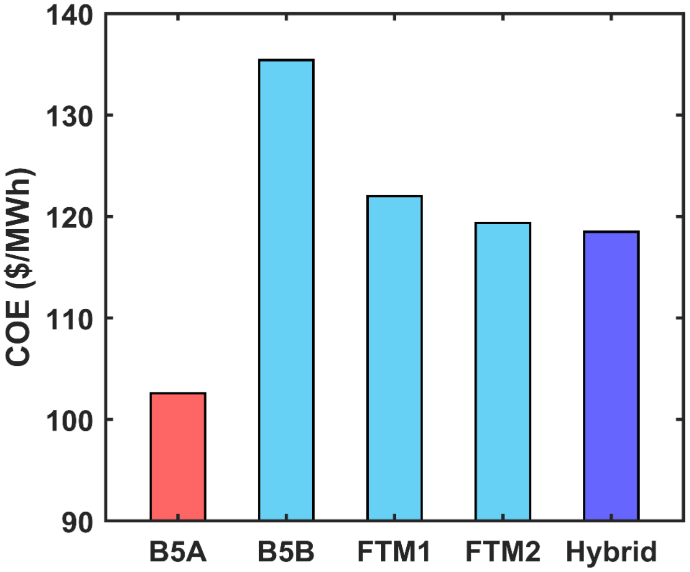

Figure 2.71. Comparison of COE values by using GEE gasifier B5A (without carbon capture), two-stage Selexol (B5B), FTM1, FTM2, and the hybrid membrane configuration with 35% FTM2 and 65% FTM1.

Selective H_2S Removal from Captured CO_2

A further inspection of the process economics indicates that the single-stage Selexol unit, which removes the H_2S from the captured CO_2, accounts for ca. 33% of the capital cost. In order to further reduce the capture cost, a continuous membrane column process was designed to replace the single-stage Selexol process for removing H_2S from the captured mixture of H_2S and CO_2 to produce a high-purity CO_2 product. This alternative process is depicted in Figure 2.70, where the permeate of MB-01 could be compressed to 15 bar by a 3-stage front-loaded centrifugal compressor MSC-01 and sent to the second membrane stage MB-02 unit for H_2S removal. This stage utilizes membrane containing a severely sterically hindered amine carrier with a high H_2S/CO_2 selectivity. The H_2S-stripped CO_2 stream is eventually compressed to 153 bar by a 3-stage front-loaded centrifugal compressor MSC-02 for sequestration or enhanced oil recovery.

Special attention should be paid to the second membrane stage MB-02. In order to enrich the H_2S from 1.5% (as in MB-01 permeate) to 35% (as for the Claus process), MB-02 needs to be operated as a continuous membrane column, the schematic of which is shown in Figure 2.71. As seen, MB-02 is split into two substages in-series. The permeate gas of MB-01 is compressed by MSC-01 to 15 bar and sent to the interconnection of the two substages. The H_2S permeates from the high-pressure to the low-pressure side. The majority of the H_2S-stripped, pressurized CO_2 is sent to MSC-02 for further compression; the remaining of it is expanded and recycled to the low-pressure side. Similarly, the majority of the H_2S-rich, low-pressure permeate is sent the Claus process for sulfur recovery; the remaining of it is recompressed and recycled to the high-pressure side. The two recycle streams enhance the transmembrane driving force for H_2S. Therefore, a high H_2S enrichment factor can be achieved with a practical H_2S/CO_2 selectivity.

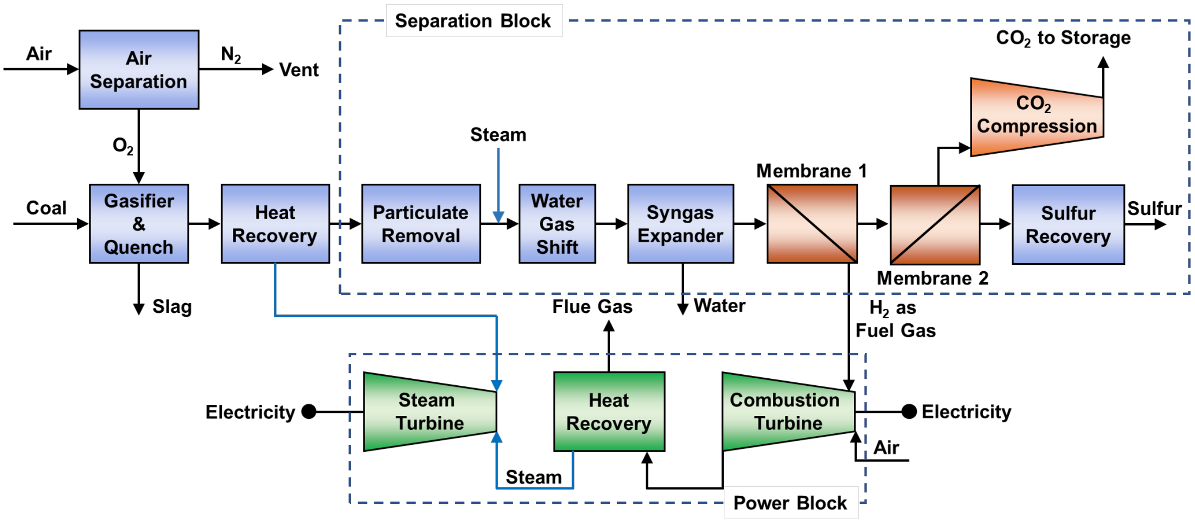

Figure 2.72. Location of the membrane separation units in an IGCC power plant with a CO_2-selective membrane stage (Membrane 1 or MB-01) for bulk acid gas removal and a H_2S-selective continuous membrane column (Membrane 2 or MB-02) for H_2S removal.

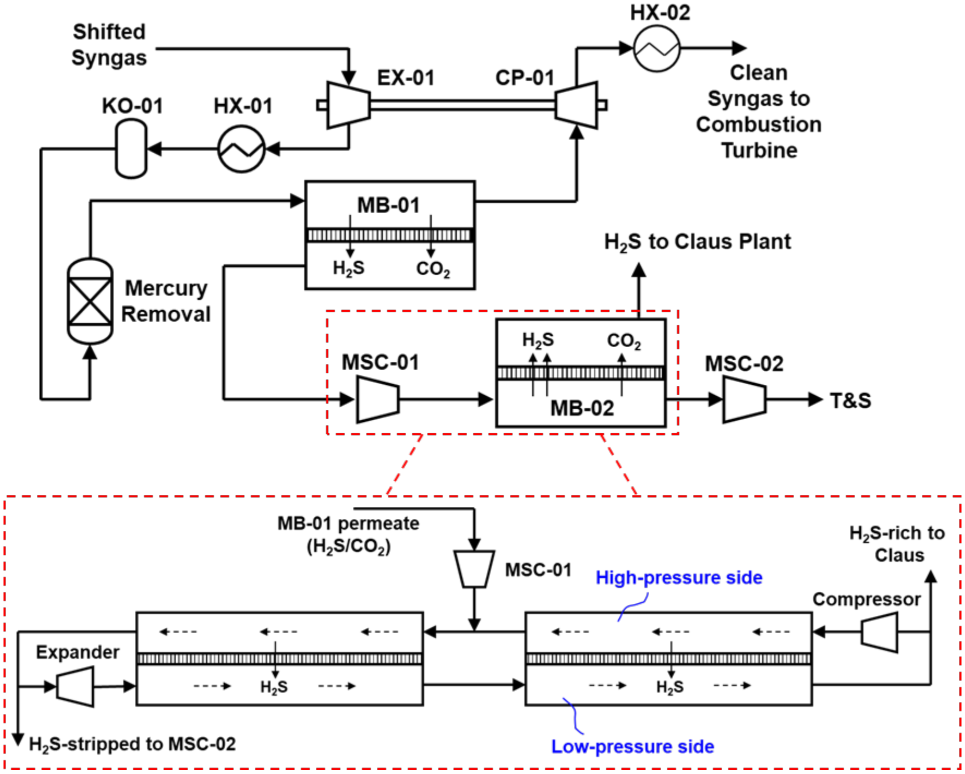

Figure 2.73. Flowsheet of membrane process for integration in IGCC using a continuous membrane column for H_2S removal.

The continuous membrane column shown in Figure 2.71 has been modeled to calculate the required H_2S/CO_2 selectivity to enrich the H_2S from 1.5% to 35%. The process economics has also been evaluated in terms of the increase in COE. The feed and permeate pressures are fixed at 15 and 1.1 bar, respectively. As shown in Figure 2.72, a minimum selectivity of 10 is required to achieve the separation specifications. A higher selectivity reduces the COE increase, with a minimum achieved at 20–25 selectivity. Also shown in Figure 2.72 is the COE increase if a single-stage Selexol process was used for the H_2S separation. As seen, a selectivity of 14 is required for the membrane column to be as cost-effective as the Selexol process. With a selectivity of 25, the COE increase could be reduced to 14.5%. Further increasing the selectivity leads to no significant cost reduction.

Also shown in Figure 2.72 are the COE increases corresponding to the best membrane M25 as shown in Table 2.4. As seen, the high H_2S/CO_2 selectivity reduces the COE increase from 15.3% to 14.9%. The associated system is more cost-effective than the single-stage Selexol process. In the consideration of the early development stage of the membrane containing the severely sterically hindered amine carrier, future compositional improvement could provide a higher H_2S/CO_2 selectivity to make the continuous membrane column even more advantageous economically.

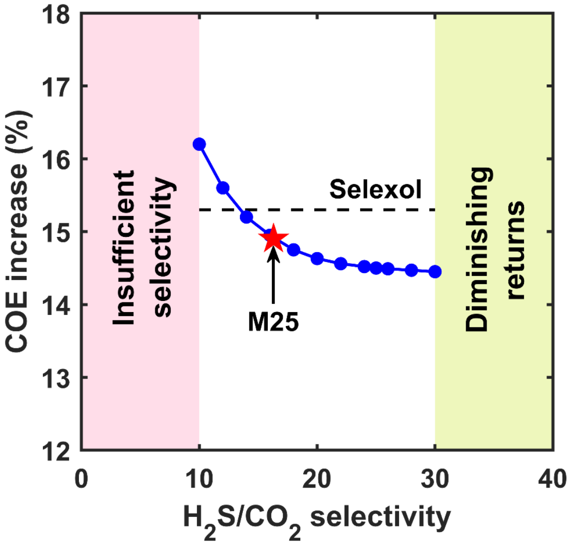

Figure 2.74. Effect of H_2S/CO_2 selectivity on COE increase. The dashed line represents the COE increase when the single-stage Selexol was used for sulfur removal.

Updated TEA Based on Baseline Document Revision 4

In the previous sections, Cases B5A and B5B in the DOE Cost and Performance Baseline for Fossil Energy Plants Volume 1b: Bituminous Coal (IGCC) to Electricity Revision 2b—Year Dollar Update (Revision 2b, 2015) [24] are taken as reference for the process and cost modeling. All calculations are based on a 550 MW_e net power IGCC power plant, and the COE is reported in 2011 U.S. dollars. Although it is not requested by DOE-NETL, we have taken the initiative to update the TEA based on the Cost and Performance Baseline for Fossil Energy Plants Volume 1: Bituminous Coal and Natural Gas to Electricity (Revision 4, 2019) [53]. Due to the limited time, only the optimized process with the continuous membrane column for selective H_2S removal (i.e., that shown in Figure 2.71) has been updated. The changes in terms of process and cost modeling are as follows:

- The shifted syngas flow rate and composition have been adjusted based on Case B5B in the 2019 Baseline Document.
- The shifted syngas pressure has been reduced from 54.1 bar (based on Stream 12 in the 2015 Baseline Document) to 47.9 bar (based on Stream 17 in the 2019 Baseline Document).
- The shifted syngas temperature has been reduced from 240°C (based on Stream 12 in the 2015 Baseline Document) to 225°C (based on Stream 17 in the 2019 Baseline Document).
- For the continuous membrane column, the H_2S is enriched to 45.8% (based on Stream 27 in the 2019 Baseline Document) rather than the 34.77% (based on Stream 19 in the 2015 Baseline Document).
- The equipment cost has been escalated from 2011 to 2018 U.S. dollars.
- The waste disposal cost has been increased from $27.80/tonne to $38.00/tonne.
- The COE for the IGCC plant without carbon capture (i.e., Case 5BA) has been increased from $102.6/MWh to $107.9/MWh. In accordance, the COE for the two-stage Selexol process (i.e., Case B5B) has also been increased from $134.5/MWh to $144.2/MWh. Therefore, the COE increase incurred by the two-stage Selexol process has been increased from 31.1% to 33.6%.

Figure 2.73 shows the equipment costs calculated based on the 2015 (Revision 2b) and 2019 (Revision 4) Baseline Documents. As shown in this figure, the largest cost increase is observed for the multi-stage compressor (MSC), which increased by $3.0 million; this increase is purely caused by the inflation from 2011 to 2018 U.S. dollars. The syngas cooler (HX) cost also increases by $1.6 million. Due to the reduced shifted syngas pressure, the turbo expander (EX) cannot cool the syngas to the same extent via thermal expansion; therefore, the cooling duty of the syngas cooler is increased. Another major increase in capital cost is the continuous membrane column for H_2S/CO_2 separation (MB-02), which is mainly caused by the higher H_2S concentration required for the Claus plant. The capital cost for the CO_2/H_2 separation membrane (MB-01) actually reduces slightly due to the lower syngas flow rate.

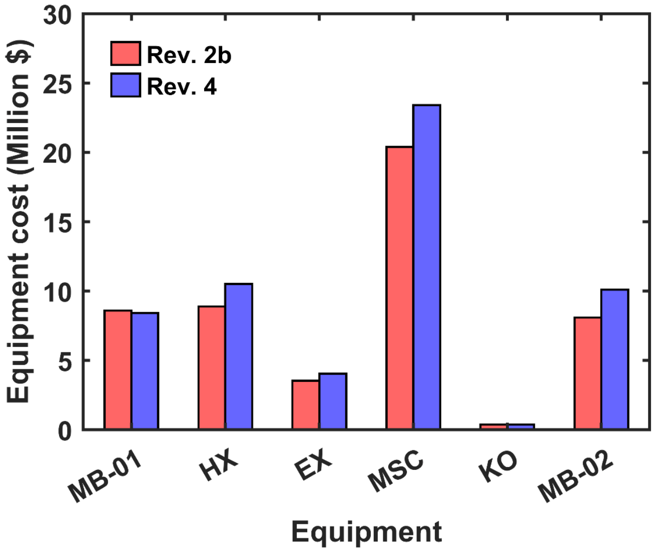

Figure 2.75. Equipment costs calculated based on the 2015 (Rev. 2b) [24] and 2019 (Rev. 4) [53] Baseline Documents. Acronyms: MB-01 = membrane for CO_2/H_2 separation; HX = syngas cooler; EX = turbo exchanger; MSC = multi-stage compressor; KO = knockout vessel; MB-02 = continuous membrane column for H_2S/CO_2 separation.

Figure 2.74 shows the COE values calculated based on the 2015 (Revision 2b) and 2019 (Revision 4) Baseline Documents. As seen, the COE of the membrane process increases from \$117.9/MWh to \$124.4/MWh. Therefore, the COE increase with respect to Case B5A also increases from 14.9% to 15.3%. In comparison, the two-stage Selexol process leads to COE increase values of 31.1% and 33.6% based on the 2015 and 2019 Baseline Documents, respectively. Therefore, the membrane process is still advantageous compared with the two-stage Selexol process.

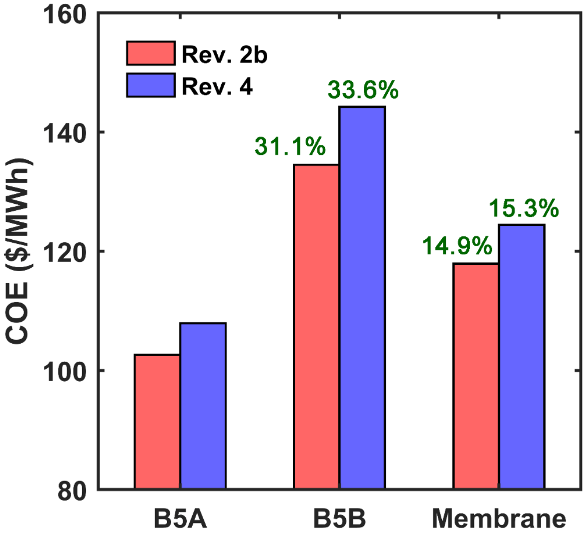

Figure 2.76. COE values calculated based on the 2015 (Rev. 2b) [24] and 2019 (Rev. 4) [53] Baseline Documents. The green numeric values are the COE increase with respect to Case B5A.

2.1.14 Task 14 – State Point Data Table

The following table lists the state-point data for our membrane-based system.

Table 2.8. State point data table.

	Units	Measured/ Estimated Performance	Projected Performance
Materials Properties			
Materials of Fabrication for Selective Layer		Hydroxyethyl-containing moiety and sterically hindered amine carriers in crosslinked polymer membrane matrix	
Materials of Fabrication for Support Layer (If applicable)		Nanoporous polymer (polysulfone) support	
Nominal Thickness of Selective Layer (μm)		15–25	15–25
Membrane Geometry		Flat sheet	Flat sheet
Max Trans-Membrane Pressure	bar	34	34
Hours tested without significant degradation		200 h	>1500 h (~ 4 years)
Membrane Performance			
Temperature	°C	107	>100
Pressure Normalized Flux for Permeate (CO_2)	GPU or equivalent	217–311	225–300
Permeate/H_2O Selectivity	-	~1	~1
Permeate/N_2 Selectivity	-	Not applicable	Not applicable
H_2S/Permeate Selectivity	-	3–19.5	>3
CO_2/H_2 Selectivity	-	125–268	120–140
H_2/CO_2 Selectivity	-	Not applicable	Not applicable
Type of Measurement (Ideal or mixed gas)	-	Mixed gas and simulated coal syngas	Simulated coal syngas
Proposed Module Design			
Flow Arrangement	-	Countercurrent in spiral-wound module	
Packing Density	m^2/m^3	2000	
Shell-Side Fluid	-	Not applicable, CO_2-rich permeate flow	

2.1.15 Task 15 – Final Technology Maturation Plan

- The Final Technology Maturation Plan has been submitted to DOE-NETL. The topical report will be further revised and finalized after incorporating NETL's input and review comments.

2.1.16 Task 16 – Environmental Health & Safety Risk Assessment

- The Environmental Health & Safety Risk Assessment has been submitted to DOE-NETL. The topical report will be further revised and finalized after incorporating NETL's input and review comments.

2.2 Success Criteria Status

All the success criteria pertained to this project have been met upon the submission of this report. The criteria concerning the lab-scale membrane performance and the process economics are briefly described as follows:

- Demonstrate CO_2 permeance = 200–275 GPU and CO_2/H_2 selectivity = 100–120 at ~110°C and 31.7 bar feed inlet (12.5 bar CO_2).
  - This criterion was met in the 3rd quarter of BP1 via a series of compositional improvement, including 1) better amine carrier with optimal steric hindrance, 2) optimized nanofiller geometry, and 3) improved polymer matrix with high CO_2 uptake.
  - The synthesis of the polymer matrix has been further improved from the 3rd quarter to now, which has led to the most advanced membrane with a CO_2 permeance of 314 GPU and a CO_2/H_2 selectivity of 138.

- Show the feasibility of a COE increase of 15.0%.
  - This criterion was met in the 6th quarter of BP2 with the membranes achieving the CO_2/H_2 and H_2S/CO_2 separation targets.
  - The removal of H_2S from the captured CO_2 is identified as the limiting factor for further reduction of the COE increase. Therefore, a continuous membrane column featuring a H_2S-selective membrane is proposed, and the required membrane performance is determined.
  - The best membrane synthesized for selective H_2S removal has the potential to reduce the COE increase to 14.9%.

The criteria concerning the membrane scale-up and module fabrication are briefly described as follows:

- Demonstrate CO_2 permeance = 275–350 GPU and CO_2/H_2 selectivity = 120–140 at ~110°C of the scale-up membranes.
  - This criterion was met in the 3rd quarter of BP2 via the (1) the scale-up synthesis of reinforcement filler, (2) improvement on the roll-to-roll coating machine to avoid pin-hole formation, and (3) demonstration of continuous coating for over 105 ft of membranes in length.
  - The gas separation performances of the scale-up membranes were on par with those synthesized in lab scale.

- Demonstrate >95% CO_2 purity with simulated syngas for 200 h for the hybrid configuration of two membrane modules in series.
  - This criterion was met in the 6th quarter of BP2 with the two SW membrane modules containing the FTM2 and FTM1 membranes, respectively, connected in series.
  - The hybrid configuration of two membrane modules in series demonstrated a H_2 recovery of 99.3% at 90% CO_2 removal and a CO_2 purity of 95.2%.
  - The hybrid configuration of two membrane modules in series remained stable for 200 h with the simulated syngas at 107°C.

2.3 Schedule Status

Budget Period 1

Table 2.9. Milestone status report for Budget Period 1.

Milestone Title Description	Planned Completion Date	Actual Completion Date	Verification Method	Comments
Task 1. Project Management and Planning	**3/31/2020**	3/31/2020	–	
Updated PMP submitted	10/31/2018	9/24/2018	Updated PMP file	
Project kick-off meeting held	11/16/2018	11/16/2018	Presentation file	
BP1 project review meeting held	02/18/2020	02/18/2020	Presentation file	
Task 2. Synthesis of Transformational Membranes	**12/31/2019**	3/31/2020	–	
Sterically hindered amines as CO_2 carriers	12/31/2019	12/27/2019	Membrane synthesis reported in quarterly report	
Incorporate ethylene oxide moieties	12/31/2019	12/27/2019	Membrane synthesis reported in quarterly report	
Study the MW of polyethylene glycol and derivatives	12/31/2019	12/27/2019	Membrane synthesis reported in quarterly report	
Add amine-containing hydroxyethyl moieties	12/31/2019	12/27/2019	Membrane synthesis reported in quarterly report	
Incorporate nanofillers	12/31/2019	12/27/2019	Membrane synthesis reported in quarterly report	
Synthesize higher MW polyalcohol	3/31/2020	3/31/2020	Membrane synthesis reported in quarterly report	
Synthesize higher MW polyamines	3/31/2020	3/31/2020	Membrane synthesis reported in quarterly report	
Task 3. Membrane Characterization	**3/31/2020**	3/31/2020	–	
Demonstrate CO_2 permeance = 200–275 GPU and CO_2/H_2 selectivity = 100–120 at ~110°C and 31.7 bar feed inlet (12.5 bar CO_2)	3/31/2020	3/31/2020	Performance data reported in quarterly report	
Task 4. Preliminary Techno-economic Analysis Performance	**3/31/2020**	3/31/2020	–	
Show the feasibility of a COE increase of 15.3%	3/31/2020	3/31/2020	Submission of preliminary TEA report	

Quarterly Reports submitted	01,04,07, 10/30/2019 and 01, 04/30/2020	Q1: 01/28/2019 Q2: 04/14/2019 Q3: 07/23/2019 Q4: 10/26/2019 Q5: 01/27/2020 Q6: 04/23/2020	Project Officer	

Budget Period 2

Table 2.10. Milestone status report for Budget Period 2.

Milestone Title Description	Planned Completion Date	Actual Completion Date	Verification Method	Comments
Task 1. Project Management and Planning	**9/30/2021**		–	
Task 5. Optimized Membrane Synthesis	**7/31/2020**	9/30/2021	Performance data reported in quarterly report	
Task 6. Optimized Membrane Characterization	**7/31/2020**		–	
Demonstrate CO_2 permeance = 275–350 GPU and CO_2/H_2 selectivity = 120–140 at ~110°C and 31.7 bar feed inlet (12.5 bar CO_2)	7/31/2020	9/30/2021	Performance data reported in quarterly report	
Task 8. Optimized Scale-up Membrane Characterization	**10/31/2020**		–	
Demonstrate CO_2 permeance = 275–350 GPU and CO_2/H_2 selectivity = 120–140 at ~110°C and 31.7 bar feed inlet (12.5 bar CO_2)	10/31/2020	10/31/2020	Performance data reported in quarterly report	
Task 10. Prototype Membrane Module Testing	**6/30/2021**		–	
Demonstrate CO_2 permeance = 275–350 GPU and CO_2/H_2 selectivity = 120–140 at ~110°C and 31.7 bar feed inlet (12.5 bar CO_2)	6/30/2021	6/30/2021	Performance data reported in quarterly report	
Task 11. Complete Parametric Testing with Prototype Modules	**7/31/2021**			
Complete parametric testing with conditions identified for steady state operation	7/31/2021	9/30/2021	Performance data reported in quarterly report	
Task 12. Complete Steady-State Operation of Prototype Modules	**9/30/2021**		–	
Demonstrate >95% CO_2 purity with simulated syngas for 200 hours	9/30/2021	9/30/2021	Performance data reported in quarterly report	

Task 13. Final Techno-economic Analysis	**9/30/2021**		–	
Show the feasibility of a COE increase of 15.0%	9/30/2021	9/30/2021	Submission of final TEA report	
Task 14. State point data table submitted	**9/30/2021**	9/30/2021	Submission of state point data table	
Task 15. Technology Maturation Plan submitted	**9/30/2021**	10/22/2021	Submission of TMP	
Task 16. EH&S Risk Assessment submitted	**9/30/2021**	10/22/2021	Submission of EH&S Risk Assessment report	
Quarterly Reports Submitted	Q7: 07/30/2020 Q8: 10/30/2020 Q9: 01/30/2021 Q10: 04/30/2021 Q11: 07/30/2021 Q12: 10/30/2021 Q13: 01/30/2022 Q14: 04/30/2022	Q7: 07/22/2020 Q8: 10/24/2020 Q9: 01/26/2021 Q10: 04/26/2021 Q11: 07/23/2021 Q12: 10/26/2021 Q13: 01/17/2022 Q14: 04/30/2022	Project Officer	
Final Report Submitted	06/30/2022	06/11/2022	Submission of Final Report	

References

1. W. S. W. Ho and K. K. Sirkar, Membrane Handbook, Kluwer Academic Publishers, Boston (2001).
2. J. Zou and W. S. W. Ho, "CO_2-Selective Polymeric Membranes Containing Amines in Crosslinked Poly(vinyl alcohol)", Journal of Membrane Science, 286, 310–321 (2006).
3. H. Bai and W. S. W. Ho, "Carbon Dioxide-Selective Membranes for High-Pressure Synthesis Gas Purification", Industrial & Engineering Chemistry Research, 50, 12152–12161 (2011).
4. R. Xing and W. S. W. Ho, "Crosslinked Polyvinylalcohol–Polysiloxane/Fumed Silica Mixed Matrix Membranes Containing Amines for CO_2/H_2 Separation", Journal of Membrane Science, 367, 91–102 (2011).
5. Y. Zhao and W. S. W. Ho, "Steric Hindrance Effect on Amine Demonstrated in Solid Polymer Membranes for CO_2 Transport", Journal of Membrane Science, 415, 132–138 (2012).
6. Y. Zhao, B. T. Jung, L. Ansaloni, and W. S. W. Ho, "Multiwalled Carbon Nanotube Mixed Matrix Membranes Containing Amines for High Pressure CO_2/H_2 Separation", Journal of Membrane Science, 459, 233–243 (2014).
7. J. Zou, J. Huang, and W. S. W. Ho, "CO_2-Selective Water Gas Shift Membrane Reactor for Fuel Cell Hydrogen Processing", Industrial & Engineering Chemistry Research, 46, 2272–2279 (2007).
8. J. Zou and W. S. W. Ho, "Hydrogen Purification for Fuel Cells by Carbon Dioxide Removal Membrane Followed by Water Gas Shift Reaction", Journal of Chemical Engineering of Japan, 40, 1011–1020 (2007).
9. J. Huang, J. Zou, and W. S. W. Ho, "Carbon Dioxide Capture Using a CO_2-Selective Facilitated Transport Membrane", Industrial & Engineering Chemistry Research, 47, 1261–1267 (2008).
10. A. Sabetghadam and T. Mohammadi, "Effect of Annealing Temperature and Time on Structure and Performance of Poly(Vinylalcohol) Nanocomposite Membranes", Polymer Engineering & Science, 50, 2392–2399 (2010).
11. Q. G. Zhang, Q. L. Liu, Z. Y. Jiang, L. Y. Ye, and X. H. Zhang, "Effects of Annealing on the Physico-Chemical Structure and Permeation Performance of Novel Hybrid Membranes of Poly(vinyl alcohol)/γ-Aminopropyl-Triethoxysilane", Microporous and Mesoporous Materials, 110, 379–391 (2008).
12. Q. G. Zhang, Q. L. Liu, S. P. Huang, W. W. Hu, and A. M. Zhu, "Microstructure-Related Performances of Poly(vinyl alcohol)-Silica Hybrid Membranes: A Molecular Dynamics Simulation Study", Journal of Materials Chemistry, 22, 10860–10866 (2012).
13. M. Krumova, D. Lopez, R. Benavente, C. Mijangos, and J. Perena, "Effect of Crosslinking on the Mechanical and Thermal Properties of Poly(vinyl alcohol)", Polymer, 41, 9265–9272 (2000).
14. J. S. Park, J. W. Park, and E. Ruckenstein, "On the Viscoelastic Properties of Poly(vinyl alcohol) and Chemically Crosslinked Poly(vinyl alcohol)", Journal of Applied Polymer Science, 82, 1816–1823 (2001).
15. L. Ansaloni, Y. Zhao, B. T. Jung, K. Ramasubramanian, M. G. Baschetti, and W. S. W. Ho, "Facilitated Transport Membranes Containing Amino-Functionalized Multi-Walled Carbon Nanotubes for High-Pressure CO_2 Separations", Journal of Membrane Science, 490, 18–28 (2015).
16. Y. Zhu, S. Murali, M. D. Stoller, K. Ganesh, W. Cai, P. J. Ferreira, A. Pirkle, R. M. Wallace, K. A. Cychosz, and M. Thommes, "Carbon-Based Supercapacitors Produced by Activation of Graphene", Science, 332, 1537–1541 (2011).
17. G. Sartori and D. W. Savage, "Sterically Hindered Amines for Carbon Dioxide Removal from Gases", Industrial & Engineering Chemistry Fundamentals, 22, 239–249 (1983).

18. Z. Tong and W. S. W. Ho, "New Sterically Hindered Polyvinylamine Membranes for CO_2 Separation and Capture", Journal of Membrane Science, 543, 202–211 (2017).
19. F. Rindfleisch, T. P. DiNoia, and M. A. McHugh, "Solubility of Polymers and Copolymers in Supercritical CO_2", The Journal of Physical Chemistry, 100, 15581–15587 (1996).
20. H. Lin and B. D. Freeman, "Materials Selection Guidelines for Membranes That Remove CO_2 from Gas Mixtures", Journal of Molecular Structure, 739, 57–74 (2005).
21. H. Ha, J. Park, S. Ando, C. B. Kim, K. Nagai, B. D. Freeman, and C. J. Ellison, "Gas Permeation and Selectivity of Poly(dimethylsiloxane)/Graphene Oxide Composite Elastomer Membranes", Journal of Membrane Science, 518, 131–140 (2016).
22. W. C. Oliver and G. M. Pharr, "An Improved Technique for Determining Hardness and Elastic Modulus Using Load and Displacement Sensing Indentation Experiments", Journal of Materials Research, 7, 1564–1583 (1992).
23. Y. Han and W. S. W. Ho, "Recent Advances in Polymeric Membranes for CO_2 Capture", Chinese Journal of Chemical Engineering, 26, 2238–2254 (2018).
24. T. Fout, A. Zoelle, D. Keairns, M. Turner, M. Woods, N. Kuehn, V. Shah, V. Chou, L. Pinkerton, and J. Black, Cost and Performance Baseline for Fossil Energy Plants Volume 1b: Bituminous Coal (IGCC) to Electricity Revision 2b—Year Dollar Update, U.S. Departmeant of Energy, Report Number: DOE/NETL-2015/1727, Washington, DC, USA, 2015.
25. J. Hao, P. Rice, and S. Stern, "Upgrading Low-Quality Natural Gas with H_2S- and CO_2-Selective Polymer Membranes: Part II. Process Design, Economics, and Sensitivity Study of Membrane Stages with Recycle Streams", Journal of Membrane Science, 320, 108–122 (2008).
26. N. Voutchkov, Desalination Engineering: Planning and Design, McGraw Hill Professional, New York (2012).
27. R. Stoller and S. Zinkle, "On the Relationship between Uniaxial Yield Strength and Resolved Shear Stress in Polycrystalline Materials", Journal of Nuclear Materials, 283, 349–352 (2000).
28. X. Zhao, C. M. Hayner, M. C. Kung, and H. H. Kung, "Flexible Holey Graphene Paper Electrodes with Enhanced Rate Capability for Energy Storage Applications", ACS Nano, 5, 8739–8749 (2011).
29. Y. Xu, C. Y. Chen, Z. Zhao, Z. Lin, C. Lee, X. Xu, C. Wang, Y. Huang, M. I. Shakir, and X. Duan, "Solution Processable Holey Graphene Oxide and Its Derived Macrostructures for High-Performance Supercapacitors", Nano Letters, 15, 4605–4610 (2015).
30. X. Chen, Z. Feng, J. Gohil, C. M. Stafford, N. Dai, L. Huang, and H. Lin, "Reduced Holey Graphene Oxide Membranes for Desalination with Improved Water Permeance", ACS Appl Mater Interfaces, 12, 1387–1394 (2020).
31. K. Ramasubramanian, M. Song, and W. S. W. Ho, "Spiral-Wound Water-Gas-Shift Membrane Reactor for Hydrogen Purification", Industrial & Engineering Chemistry Research, 52, 8829–8842 (2013).
32. W. Salim, Y. Han, V. Vakharia, D. Wu, D. J. Wheeler, and W. S. W. Ho, "Scale-up of Amine-Containing Membranes for Hydrogen Purification for Fuel Cells", Journal of Membrane Science, 573, 465–475 (2019).
33. G. B. Giovenzana, D. Imperio, A. Penoni, and G. Palmisano, "Reductive Amination with Zinc Powder in Aqueous Media", Beilstein Journal of Organic Chemistry, 7, 1095–1099 (2011).
34. W. S. W. Ho and D. Dalrymple, "Facilitated Transport of Olefins in Ag^+-Containing Polymer Membranes", Journal of Membrane Science, 91, 13–25 (1994).

35. Y. Han, D. Wu, and W. S. W. Ho, “Simultaneous Effects of Temperature and Vacuum and Feed Pressures on Facilitated Transport Membrane for CO_2/N_2 Separation”, Journal of Membrane Science, 573, 476–484 (2019).
36. Y. Han and W. S. W. Ho, “Design of Amine-Containing CO_2-Selective Membrane Process for Carbon Capture from Flue Gas”, Industrial & Engineering Chemistry Research, 59, 5340–5350 (2020).
37. Y. Han and W. S. W. Ho, “Recent Advances in Polymeric Facilitated Transport Membranes for Carbon Dioxide Separation and Hydrogen Purification”, Journal of Polymer Science, 58, 2435–2449 (2020).
38. Z. Tong and W. S. W. Ho, “Facilitated Transport Membranes for CO_2 Separation and Capture”, Separation Science and Technology, 52, 156–167 (2017).
39. K. Ramasubramanian, Y. Zhao, and W. S. W. Ho, “CO_2 Capture and H_2 Purification: Prospects for CO_2-Selective Membrane Processes”, AIChE Journal, 59, 1033–1045 (2013).
40. P. Li, Z. Wang, Z. Qiao, Y. Liu, X. Cao, W. Li, J. Wang, and S. Wang, “Recent Developments in Membranes for Efficient Hydrogen Purification”, Journal of Membrane Science, 495, 130–168 (2015).
41. C. Zhang, Z. Wang, Y. Cai, C. Yi, D. Yang, and S. Yuan, “Investigation of Gas Permeation Behavior in Facilitated Transport Membranes: Relationship between Gas Permeance and Partial Pressure”, Chemical Engineering Journal, 225, 744–751 (2013).
42. S. Li, Z. Wang, W. He, C. Zhang, H. Wu, J. Wang, and S. Wang, “Effects of Minor SO_2 on the Transport Properties of Fixed Carrier Membranes for CO_2 Capture”, Industrial & Engineering Chemistry Research, 53, 7758–7767 (2014).
43. R. Rea, M. G. D. Angelis, and M. G. Baschetti, “Models for Facilitated Transport Membranes: A Review”, Membranes, 9, 26 (2019).
44. J. D. Goddard, J. S. Schultz, and S. R. Suchdeo, “Facilitated Transport via Carrier-Mediated Diffusion in Membranes: Part II. Mathematical Aspects and Analyses”, AIChE Journal, 20, 625–645 (1974).
45. J. S. Schultz, J. D. Goddard, and S. R. Suchdeo, “Facilitated Transport via Carrier-Mediated Diffusion in Membranes: Part I. Mechanistic Aspects, Experimental Systems and Characteristic Regimes”, AIChE Journal, 20, 417–445 (1974).
46. Y. Han and W. S. W. Ho, “Facilitated Transport Membranes for H_2 Purification from Coal-Derived Syngas: A Techno-Economic Analysis”, Journal of Membrane Science, 636, 119549 (2021).
47. H. Lin, E. Van Wagner, B. D. Freeman, L. G. Toy, and R. P. Gupta, “Plasticization-Enhanced Hydrogen Purification Using Polymeric Membranes”, Science, 311, 639–642 (2006).
48. Y. Han and W. S. W. Ho, “Polymeric Membranes for CO_2 Separation and Capture”, Journal of Membrane Science, 628, 119244 (2021).
49. V. Vakharia, K. Ramasubramanian, and W. S. W. Ho, “An Experimental and Modeling Study of CO_2-Selective Membranes for IGCC Syngas Purification”, Journal of Membrane Science, 488, 56–66 (2015).
50. H. Lin, Z. He, Z. Sun, J. Kniep, A. Ng, R. W. Baker, and T. C. Merkel, “CO_2-Selective Membranes for Hydrogen Production and CO_2 Capture – Part II: Techno-Economic Analysis”, Journal of Membrane Science, 493, 794–806 (2015).
51. H. Lin, Z. He, Z. Sun, J. Vu, A. Ng, M. Mohammed, J. Kniep, T. C. Merkel, T. Wu, and R. C. Lambrecht, “CO_2-Selective Membranes for Hydrogen Production and CO_2 Capture – Part I: Membrane Development”, Journal of Membrane Science, 457, 149–161 (2014).

52. B. W. Rowe, L. M. Robeson, B. D. Freeman, and D. R. Paul, “Influence of Temperature on the Upper Bound: Theoretical Considerations and Comparison with Experimental Results”, Journal of Membrane Science, 360, 58–69 (2010).
53. R. James, A. Zoelle, D. Keairns, M. Turner, M. Woods, and N. Kuehn, Cost and Performance Baseline for Fossil Energy Plants Volume 1: Bituminous Coal and Natural Gas to Electricity, U.S. Department of Energy, Report Number: DOE/NETL-Pub-22638, Washington, DC, USA, 2019.

Suppliers

1. Sigma-Aldrich, 3050 Spruce Street, St. Louis, MO, 63103, USA; www.sigmaaldrich.com.
2. ThermoFisher Scientific. 25 Nimble Hill Rd., Newington, NH, USA. Contact: Greg Vinson, Ph: (800)258-0830, Office: (281)334-0164, Mobile: (281)851-0640.
3. Purolite Corporation, 150 Monument Road, Bala Cynwyd, PA 19004, USA; Phone: 1-610-668-9090; Fax: 1-610-668-8139; www.purolite.com.
4. VWR International, Radnor Corporate Center Building One, Suite 200 100 Matsonford Road Radnor, PA19087-8660, USA; Phone:1-610-386-1700; www.vwr.com.
5. Varian Inc., 3120 Hansen Way, Palo Alto, CA 94304-1030, USA.
6. McMaster Carr, P.O. Box 94930, Cleveland, OH 44101-4930, USA; Phone: 330-995-5500; Fax: 330-995-9600.
7. Microdyn-Nadir US Inc. (formerly TriSep Corporation), 93 South La Patera Lane, Goleta, CA 93117, USA; Phone: 805-964-8003; Fax: 805-964-1235.
8. Arkema Inc., 900 First Avenue, King of Prussia, PA 19406, USA; Phone: 610-205-7252.
9. The Ohio State University Department of Chemistry Machine Shop, 0041 Evans Laboratory, 88 W 18th Avenue, Columbus, OH 43210, USA.
10. Branson Ultrasonics Corporation, 41 Eagle Rd., Danbury, CT 06813-1961, USA.
11. Spectrum Laboratories, Inc., 18617 S Broadwick Street, Rancho Dominguez, CA 90220, USA.

Symbols, Abbreviations and Definitions

AFM	atomic force microscopy
AS	aminosilane
BP	Budget Period
CBE	Chemical and Biomolecular Engineering
COE	cost of electricity
DLS	dynamic light scattering
DOE	U.S. Department of Energy
DSC	differential scanning calorimetry
E_r	reduced Young's modulus
EX	turbo exchanger
FTM	facilitated transport membrane
GC	gas chromatography
GEE	General Electric Energy
GPU	gas permeation unit; 1 GPU = 10^{-6} cm^3(STP) cm^{-2} s^{-1} $cmHg^{-1}$
HX	heat exchanger
IGCC	integrated gasification combined cycle
KO	water knockout
MB	membrane stage
MFC	mass flow controller
MSC	multi-stage compressor
MSE	Materials Science and Engineering
MW	molecular weight
NMR	nuclear magnetic resonance spectroscopy
OSU	The Ohio State University in Columbus, Ohio
PC	pressure control
PMP	Project Management Plan
Q	Quarter
RO	reverse osmosis
SCD	sulfur chemiluminescence detector
TC	temperature control
T_g	glass transition temperature
T&S	transportation and sequestration
UF	ultrafiltration
XPS	X-ray photoelectron spectroscopy
XRD	X-ray diffraction

Distribution List

Katharina (Katy) R. Daniels
Project Manager
Carbon Capture Team
National Energy Technology Laboratory
U.S. Department of Energy
626 Cochran Mill Road
P.O. Box 10940
Pittsburgh, PA 15236-0940

W.S. Winston Ho
Yang Han
Ting Yu Chen
Jingying Hu
Yi-Chen Huang
Ruizhi Pang
Babul Prasad
Shraavya Rao
Yutong Yang
The Ohio State University
William G. Lowrie Department of Chemical and Biomolecular Engineering
Department of Materials Science and Engineering
458 CBEC Building
151 West Woodruff Avenue
Columbus OH 43210-1350